

© 2025 James A. Helmich

DEVELOPMENT AND TESTING OF A MODULAR CUBESAT  
SYSTEM ENABLING RAPID ACCESS TO SPACE

BY

JAMES A. HELMICH

THESIS

Submitted in partial fulfillment of the requirements  
for the degree of Master of Science in Aerospace Engineering  
in the Graduate College of the  
University of Illinois Urbana-Champaign, 2025

Urbana, Illinois

Advisor:

Adjunct Clinical Associate Professor Michael F. Lembeck

# Abstract

This thesis presents the development of a modular CubeSat system, herein called CUBE, that provides configurable payload hosting capabilities and promotes rapid access to space. Small satellites are being increasingly utilized to operate civil, defense, commercial, and educational payloads in space. These satellites offer comparatively easy access to space for payload developers. However, current standard program practices are inefficient and create many opportunities for irrecoverable mission failures in the leadup to launch. Each new payload typically requires a bespoke satellite to support it. The assembly, integration, and testing process is highly serialized, leading to schedule delays and late discovery of integration issues. All of this results in large monetary and schedule burdens on any organization wishing to launch a payload.

The novel modular system developed for this thesis streamlines the assembly, integration, and testing process by dividing the structure into independent modules that separate the payload from the supporting bus hardware. The bus hardware selected for the system can be used to support a variety of different payloads. Furthermore, the modules can be configured in different orientations to meet the specific needs of a wide range of payloads. This allows the modular system design to be used for multiple missions, removing the need for bespoke satellite design work for each payload. The bus modules can also be flight qualified and prepared in advance, allowing for rapid response missions that can accommodate late payload integration.

The versatility of the system is validated with a set of conceptual design reference missions. The design of the structure is then verified by a suite of load analyses. Once verified, a prototype of the structure is manufactured. The structure undergoes a thorough testing campaign to qualify it for spaceflight.

*For my parents, who taught me nearly everything I know.*

# Acknowledgments

I am deeply indebted to my advisor, Dr. Michael Lembeck, for mentoring me. His unparalleled skill and practical knowledge of all things aerospace is truly inspirational. I am grateful to have had his guidance both as a student and as a member of his research group. The dedication and earnestness with which he prepares young engineers to make impactful contributions during their careers is invaluable.

I am lucky to have received instruction from many great professors throughout my education. Jason Merret stands out as one of the best that I have learned from. His wealth of systems engineering experience and memorable anecdotes have shaped the way that I approach engineering problems.

I would also like to thank Michael Miller for his generous support in developing the modular CubeSat presented in this thesis. His trust, and wise feedback in design reviews, made this project possible.

I am grateful for the friendship and support of all of my colleagues at the Laboratory for Advanced Space Systems at Illinois (LASSI). They have made each workday a joy with their collaboration and humor. I am particularly grateful for David Gable, Qi Lim, Michael Harrigan, Chris Young, Rick Eason, Courtney Trom, Eric Alpine, and Hongrui Zhao. Your friendship over the years has fueled my enthusiasm for our line of work. I would also like to thank the LASSI Laboratory Manager, Murphy Stratton, for making sure I always had the materials and facilities necessary for my project.

To my friends, thank you for your encouragement and perspective. I have countless fond memories of the time we have spent maintaining our sanity together. To Allison Timm, thank you for your constant support and understanding. You have made this achievement possible and contributed so much motivation and joy throughout the process. To my family, thank you for supporting me and believing in me. Without my mother's tireless devotion to my education, or my father's constant instillation of mechanical curiosity and problem solving skills, I would not be here today. You are my role models.

# Table of Contents

<b>List of Abbreviations .....</b>	<b>vi</b>
<b>Chapter 1 Introduction .....</b>	<b>1</b>
1.1 Small Satellite Background .....	1
1.2 Responsive Space Motivation .....	3
1.3 System Objective .....	5
<b>Chapter 2 Development of a Modular CubeSat System .....</b>	<b>7</b>
2.1 Problem Setup and Response .....	7
2.2 Mission Level Functional Requirements .....	9
2.3 Design Reference Missions .....	11
<b>Chapter 3 Modular Structure Design .....</b>	<b>18</b>
3.1 Module Designs and Configurations .....	18
3.2 Interface Definitions .....	22
3.3 Internal Layouts .....	26
3.4 Mass and Center of Gravity Constraints .....	29
3.5 Example Accommodation of Design Reference Mission .....	34
3.6 Prototype Structure .....	40
<b>Chapter 4 Structural Analysis .....</b>	<b>42</b>
4.1 Finite Element Model .....	42
4.2 Sustained Acceleration .....	47
4.3 Normal Modes .....	58
<b>Chapter 5 Qualification Testing .....</b>	<b>62</b>
5.1 Test Fit Assembly .....	62
5.2 Environmental Testing .....	69
5.3 Random Vibration Testing .....	75
<b>Chapter 6 Conclusion .....</b>	<b>84</b>
6.1 Summary .....	84
6.2 Future Work .....	85
<b>References .....</b>	<b>87</b>

# List of Abbreviations

ADCS	Attitude Determination and Control Subsystem
AIT	Assembly Integration and Test
CAD	Computer Aided Design
CCD	Charged-Couple Device
CDH	Command and Data Handling Subsystem
CG	Center of Gravity
CMOS	Complementary Metal-Oxide-Semiconductor
Comms	Communications Subsystem
COTS	Commercial-Off-The-Shelf
CUBE	Configurable Universal Bus Enclosure
DoD	Department of Defense
DRM	Design Reference Mission
FEA	Finite Element Analysis
FEM	Finite Element Model
GEVS	General Environmental Verification Standard
GRMS	Root Mean Square Acceleration
GSD	Ground Sample Distance
ICD	Interface Control Diagram
M1	Module 1
M2	Module 2
MC	Module Connector
MGA	Mass Growth Allowance
MMOD	micro-meteoroid orbital debris
MMS	Multi-Mission Modular Spacecraft
MOI	Moment(s) of Inertia

NASA	National Aeronautics and Space Administration
ORS	Operationally Responsive Space
PCB	Printed Circuit Board
PDU	Power Distribution Unit
PLSB	Payload Support Board
PM	Payload Module
TacRS	Tactically Responsive Space
TVAC	Thermal Vacuum
UIUC	University of Illinois Urbana-Champaign

# Chapter 1

## Introduction

### 1.1 Small Satellite Background

In recent years, CubeSats have emerged as a predominant form factor for small satellite missions, revolutionizing the way space exploration and technology demonstrations are approached. These miniature satellites, defined by their cubic shape and standardized dimensions, have expanded the boundaries of what is possible in space missions, offering a versatile and cost-effective solution for a wide array of applications. A total of 360 CubeSats were launched in 2023, over four times the number launched a decade earlier in 2013 [1].

The introduction of CubeSat standards revolutionized space exploration and technology demonstrations by establishing a uniform framework for small satellite missions. This journey began in the late 1990s when Professors Jordi Puig-Suari of California Polytechnic State University and Bob Twiggs of Stanford University sought to create a cost-effective platform for educational and research purposes. Their vision led to the creation of the CubeSat. CubeSats are defined in standard units, where a 10 cm x 10 cm x 10 cm volume represents a single unit (1U). The ability to combine multiple units into larger configurations such as 2U, 3U, 6U, and 12U allowed for greater flexibility in design and deployment, making CubeSats a popular choice across various sectors. Fig. 1.1 illustrates the form factors of the commonly used CubeSat sizes.

The availability of CubeSat standards lowers the barrier of entry to spaceflight by defining the mechanical interface and key requirements for internal components. This standardization ensures compatibility with multiple commercially available deployer services, which act as intermediaries between CubeSats and launch vehicles. Moreover, the standardized internal component requirements facilitate the integration of components from different sources, including commercial off-the-shelf (COTS) hardware, further simplifying the

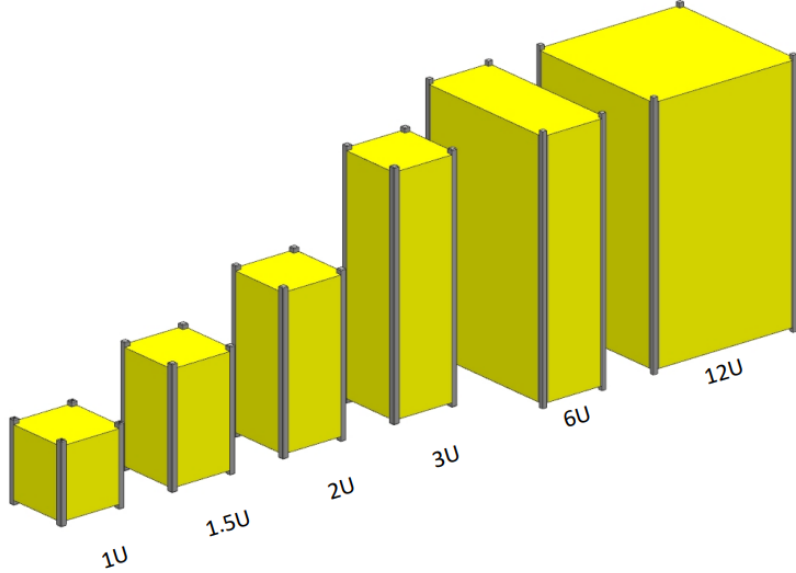


**Figure 1.1: Standard CubeSat sizes [2].**

development process. Flight hardware development benefits from the consistency provided by the CubeSat standards. Nevertheless, a significant number of engineering hours are still required to accommodate mission unique payloads. Any mission-specific work increases the cost of the mission and usually results in longer pre-flight schedules. As seen in Fig. 1.2, a state-of-the-art CubeSat mission typically takes over two years to develop from concept to launch.

Despite the use of standards, the flight hardware fabrication phase, lasting over 11 months in this timeline, remains highly serialized. It includes manufacturing and Assembly Integration and Test (AIT) activities, with many opportunities for schedule delays. Coordinating flight hardware integration when multiple organizations provide components also extends the schedule. Once fabrication is complete, System-level testing of the assembled CubeSat validates performance in launch and space environments and can reveal component weaknesses and cause hardware failures. Due to the integrated nature of CubeSats, any failure can lead to disassembly, repair, and reassembly of the entire system, often causing schedule slips [3]. AIT is crucial for mission success, and shortening this process would further enhance the utility of CubeSats.

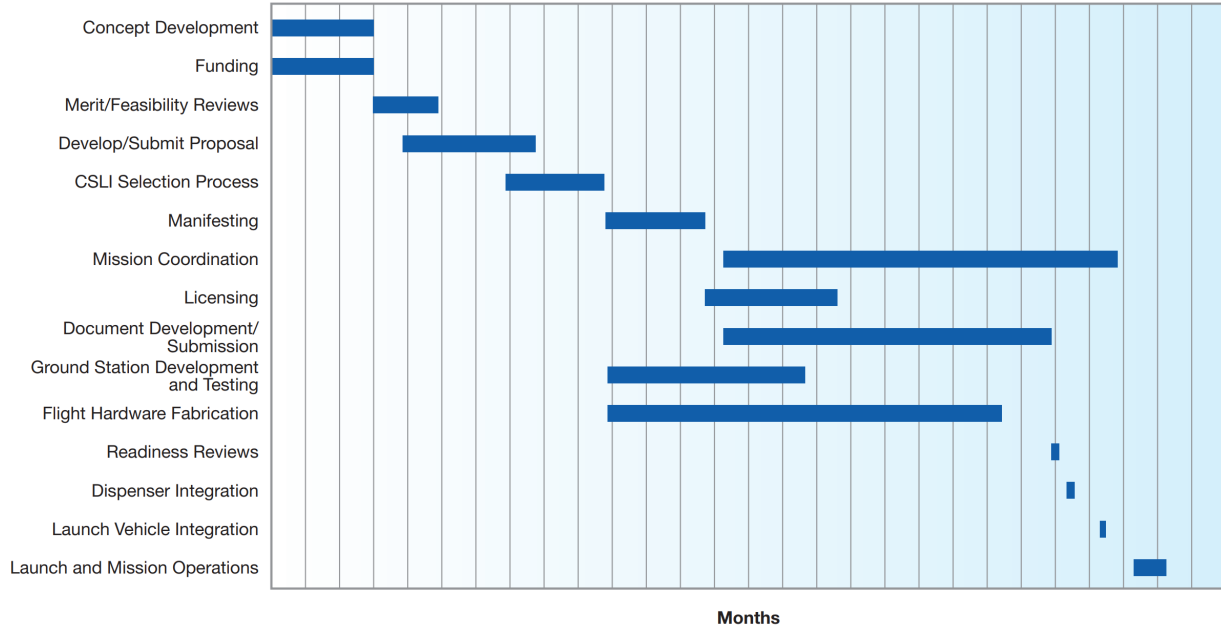


Figure 1.2: NASA suggested CubeSat development timeline [4].

## 1.2 Responsive Space Motivation

The ability to quickly integrate and launch a payload into space is very desirable for a wide range of stakeholders. The United States Air Force has exhibited a strong interest in developing Operationally Responsive Space (ORS) for over two decades [5]. ORS encompasses the capability to rapidly deploy space-based assets on an as needed basis. The U.S. Space Force calls a similar active area of development Tactically Responsive Space (TacRS) [6]. ORS and TacRS have focused on streamlining this process through a variety of approaches. Reducing pre-flight operation times from the order of months to the order of days would allow the Air Force and Space force to respond in real time to an ever-changing global environment. The principles of responsive space have been a topic of research for many decades. NASA performed relevant research in the 1970s with the development of a common spacecraft bus design that could be used for a range of missions. This system was called the Multi-Mission Modular Spacecraft (MMS) [7]. The goal of the MMS research was to lower mission costs for NASA. This cost reduction was accomplished by reducing the amount of mission specific development work required for each launch. The design of MMS split the bus into modules at the subsystem level and placed the burden of performance testing on the subsystem contractors. This approach successfully reduced the bus integration and test time from approximately eleven months to four months. The use of a consistent bus design across multiple missions also allowed the satellites to be serviceable by the Space Shuttle [8].



**Figure 1.3: ORS-1 satellite [10].**

Ultimately, the MMS was used for six missions, including Landsat 4 and 5 [8]. These MMS missions ranged from approximately 5,000 lbs. to 15,000 lbs. in launch mass. Since the development of the MMS, mission profiles for both tactical and civil stakeholders have shifted toward smaller, lower cost missions in the CubeSat class of satellites.

Responsive space efforts increased significantly in 2007 with the formation of the DoD's Operationally Responsive Space Office [9]. The office was tasked with developing payloads, busses, and launch capabilities within the low cost, rapid response constraints of ORS. The office coordinates efforts across relevant groups in the DoD and executes orders from joint military commanders. Five missions were successfully launched in the decade following its formation. Each of these missions featured unique capabilities and requirements.

The first operational mission, ORS-1 (Fig. 1.3), is noteworthy for its use as a testbed in the implementation of many new programmatic ORS approaches [9]. ORS-1 was developed as a space surveillance small satellite for the U.S. Central Command. The program utilized a rapid acquisition contract and adapted pre-existing hardware, such as the camera developed for the U2 plane [9]. Program schedules, approaches, and objectives were reassessed throughout the development. In a dramatic shift from traditional mission development, the program adhered to a "good enough" mindset to reduce unnecessary engineering efforts. The combined effect of these approaches resulted in a three-year development time from program initiation to full operation, representing a reduction of four years relative to comparable previous missions [9].

As the ORS Office looked to areas for future development in 2014, it focused on the need for assured access to space and how this need could be accomplished through disaggregated systems. The ORS Office determined that splitting the roles filled by legacy, multi-million-dollar satellites into multiple small satellite and CubeSat missions would result in a more resilient system.

The advantages of responsive space approaches are not limited to defense applications. CubeSats are also becoming more commonly used for constellation class missions. Constellation missions are often governed by coverage and revisit time requirements. Losing one spacecraft in a constellation can lead to a failure to meet the required coverage or revisit time. For this reason, critical missions, such as GPS, have historically deployed extra satellites to serve as a standby that can be commissioned as soon as an active satellite fails [11]. The alternative, building and launching a replacement when needed, is time consuming and can result in a gap in mission performance. Expediting the build and launch of a replacement satellite can also be very cost inefficient. The principles of responsive space offer a new and effective way of addressing this issue. Rapid launch capabilities can be paired with a standardized, pre-tested satellite bus. This reduces the AIT effort to an amount that can be completed quickly and efficiently.

### 1.3 System Objective

Traditional CubeSat AIT processes encumber the development and deployment of rapid response capabilities. This is the motivation for the innovative CubeSat structure system developed in the following chapters. The Configurable Universal Bus Enclosure (CUBE) system is a CubeSat system purposefully designed to significantly reduce mission unique design effort and streamline the AIT process. The objective is captured in the following system objective statement: *CUBE is a CubeSat standards compatible structure system that provides configurable payload hosting capability promoting rapid access to space.* There are several important requirements implied in the system objective statement. First, the system must comply with existing CubeSat standards. By operating within the standards, CUBE is able to leverage existing support infrastructure, such as currently available CubeSat deployers. This increases the versatility of the system by reducing mission planning workload and launch costs. Second, the description of a structure system defines the scope. The structure's design has been influenced by the bus hardware that it will ultimately support, but final bus hardware selection and AIT falls outside of the scope of this thesis. Third, the payload hosting capability provided by the system must be flexible. The structure can be adapted for a variety of payloads and is not designed for a single payload or a single mission. Payloads are supported by a set of standard interfaces compliant with the offered set of configurations. All design decisions and trades are constrained such that the structure, when combined with bus components, can be quickly integrated with any payload that meets these

interface requirements. Elements of CUBE may be environmentally tested individually and placed on the shelf for later use. After the elements are integrated, the CubeSat can be launched with minimal functional testing. Ultimately, the system is designed to accommodate missions with requirements for rapid access to space.

The objective of the system is derived from the needs and shortfalls discussed in Sections 1.1 and 1.2. The introduction of a CubeSat bus system that alleviates the schedule and integration challenges of current small satellites has the potential to make space more accessible for payload developers. CUBE accomplishes this by offering a modular structure that can be tested and flight qualified ahead of payload development. When a payload is ready, the satellite can be rapidly integrated and launched.

This thesis documents the initial development and testing of CUBE. The system's functional requirements are described, and a set of design reference missions are presented in Chapter 2. The design process and philosophy used for development is expanded upon in Chapter 3. This chapter includes definition of all system interfaces, and the application of CUBE to the design reference missions. The chapter concludes with a reduction of the subsystem components to simplified mass simulators and secondary structure. This reduced configuration is analyzed in Chapter 4. The analysis is organized into two major segments: sustained acceleration loads, and modal analysis. Chapter 5 contains details of the testing campaign performed to verify the analysis and qualify the design. This includes a test fit assembly, environmental testing, and vibration testing. The document concludes in Chapter 6 with a summary of the CUBE system and a discussion of areas for future work.

## Chapter 2

# Development of a Modular CubeSat System

### 2.1 Problem Setup and Response

Design reference missions serve as a cornerstone for defining the system and structural requirements of a modular CubeSat system. By analyzing commonalities across diverse missions, essential functionalities and recurring challenges can be identified that transcend individual payloads. This approach ensures that the CubeSat's structure and subsystems can support a variety of payloads while maintaining flexibility and reliability. Moreover, it aids in pinpointing critical design parameters, such as aperture placements, thermal management methods, and communication protocols, which are essential for ensuring payload compatibility and mission success. Ultimately, leveraging insights from reference missions streamlines the modular design process, creating a system that is both adaptable and robust for rapid deployment and efficient operation across multiple space missions.

As discussed in Chapter 1, a few external interface standards have been defined for CubeSats. However, there is no standard for integrating components into systems. This results in a lack of uniformity between CubeSat missions. Significant recurring costs are levied on stakeholders for every new CubeSat that is developed. Such costs are especially impactful to programs with limited budgets, such as those run by academic institutions. The lack of uniformity also manifests in risks associated with new development and unique operations that must be addressed for each new mission.

This thesis addresses these issues by developing a modular, reconfigurable structural design that can be re-used for a variety of missions without significant modifications. A typical 6U CubeSat bus is split into

three modules. Bus modules, Module 1 (M1) and Module 2 (M2), along with the Payload Module (PM) house either bus components or payload(s) and can be assembled in a variety of configurations. The modules share interfaces and resources across standard physical connectors. Development resources can be focused on payload development and mission unique operations support dramatically reducing development cost and risk. Additionally, system AIT procedures can be standardized. This modular CubeSat design approach is summarized in the assembly flow diagram in Fig. 2.1.

The mission begins in Phase 1a with the assembly of bus modules. These modules contain integrated subsystem components that support payload operations. The bus modules then undergo testing in Phase 2a. Having completed testing, the bus modules are ready for integration and can be stored until this takes place. Payload assembly and testing takes place in parallel with Phases 1a and 2a. The payload assembly, outlined in Phases 1b and 2b, is performed in a separate, self-contained PM. This allows for bus-independent payload development that can proceed at pace regardless of bus readiness. In Phase 3, the bus modules and PM are integrated. The satellite then undergoes expedited functional testing in Phase 4 to ensure that the module interfaces are functioning properly. The satellite is then ready for delivery to the launch vehicle in Phase 5.

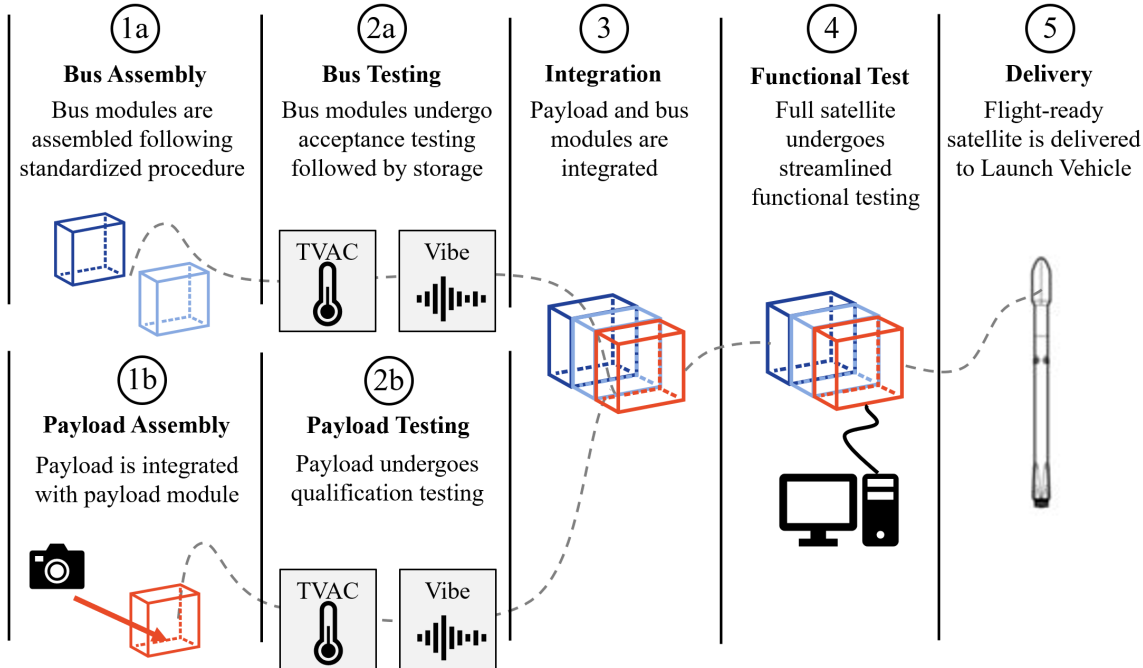


**Figure 2.1: Modular CubeSat bus and payload assembly, integration, and test flow.**

## 2.2 Mission Level Functional Requirements

The mission level functional requirements for CUBE represent the top level requirements from which all other system, component, and operations requirements will be derived. In traditional satellite development, payloads impose requirements specific to their mission. The mission level functional requirements are kept payload agnostic so as to support a wide variety of payloads without being overly prescriptive. These functions are often architecturally decomposed into subsystems and address requirements for structure, power, command and data handling, attitude determination and control, and thermal control. Performance parameters for each subsystem are more payload specific. These performance parameters for CUBE are addressed in Subsection 2.3 in the form of three independent design reference missions.

High level mission functional requirements are listed in Table 2.1. These requirements result from basic support needs that are common to many payloads. MSN-1 is a key requirement for flexibly accommodating a wide variety of anticipated CubeSat payloads. This requirement is levied to provide external apertures, dedicated for payload use, on at least four of its sides. Remote sensing, astronomical, and orbit environment sensing payloads are readily accommodated in the CUBE design.

Utility resources are also identified. MSN-2, MSN-3, and MSN-4 all relate to electrical power, which is needed for both the payload and the other bus subsystems. MSN-5, MSN-6, and MSN-10 are necessary for remote operation of a payload and extracting scientific value from a mission. MSN-7, MSN-8, and MSN-9 require that the bus be capable of two-way communications with operators on the ground for accepting commands and transmitting data and telemetry. Many payloads will require attitude control/pointing of some form. This is handled by MSN-11, which requires full three-axis pointing control for the payload. MSN-12 ensures that payload and subsystem components will have a stable thermal environment to operate within. Thermal control implementations range from simple, passive systems to complex, active systems. MSN-12 implies that the bus structure cannot insulate components from thermal control devices.

**Table 2.1: Mission level functional requirements of the modular bus**

Req. ID	Requirement	Notes
MSN-1	The bus shall structurally accommodate payloads with external apertures on four, five faces of the bus.	<i>This is configuration dependent and ensures versatile mounting options for diverse payloads, enhancing functionality.</i>
MSN-2	The bus shall generate power.	<i>This is essential to ensure continuous operation of all payloads and subsystems.</i>
MSN-3	The bus shall store power.	<i>This allows a reserve of energy to be available for critical operations during peak demand or interruptions.</i>
MSN-4	The bus shall distribute power.	<i>This ensures that all subsystems and payloads receive the necessary energy to operate efficiently.</i>
MSN-5	The bus shall collect data from the payload.	<i>This is necessary to ensure accurate and timely transmission of scientific or operational data.</i>
MSN-6	The bus shall collect telemetry.	<i>This is essential to monitor the health and status of the spacecraft systems for effective operation and diagnostics.</i>
MSN-7	The bus shall send payload data to the ground system.	<i>This ensures the transmission of vital scientific or operational information for analysis and decision-making.</i>
MSN-8	The bus shall send telemetry to the ground system.	<i>This requirement supports continuous monitoring and assessment of spacecraft health and functionality.</i>
MSN-9	The bus shall receive operational commands from the ground system.	<i>This ensures the spacecraft can be controlled and adjusted as needed for mission success.</i>
MSN-10	The bus shall execute received commands.	<i>All operational adjustments and actions required for mission success are carried out as intended.</i>
MSN-11	The bus shall point the payload in any commanded direction.	<i>This allows for precise targeting and effective data collection for mission objectives.</i>
MSN-12	The bus shall regulate the thermal environment of its elements.	<i>The thermal regulation allows components to operate efficiently within their optimal temperature range.</i>

## 2.3 Design Reference Missions

The feasibility and performance of CUBE will be measured against three design reference missions (DRMs). Each DRM identifies a pre-existing payload along with its scientific mission objective(s). The three DRMs were chosen to represent a cross section of mission profiles and payloads that are typically flown on 6U CubeSat busses. The varying performance requirements of each DRM translate into different use cases for CUBE. A brief mission description, payload description, and list of payload requirements is provided for each DRM.

### 2.3.1 Gravity Wave Detection

The objective of the Gravity Wave Detection DRM is to create maps of active gravity wave regions through the measurement of airglow brightness in the mesosphere and thermosphere of Earth’s atmosphere. The gravity waves being studied are created by weather patterns including air flow through mountainous regions and severe storm systems. The resulting gravity waves carry energy into the upper atmosphere and affect atmospheric properties including airglow [12]. The DRM is built around a photometer payload, designed by Gary Swenson in the Electrical and Computer Engineering Department at the University of Illinois Urbana-Champaign (UIUC), to measure variations in the airglow brightness induced by gravity waves [12]. This is an adaptation of the Lower Atmosphere/Ionosphere Coupling Experiment – Follow on (LAICE-F) mission developed in partnership between Virginia Polytechnic Institute and State University (VT) and UIUC [12].

A rendering of the UIUC photometer payload is shown in Fig. 2.2. The payload has seven channels, each consisting of a baffle and photomultiplier tube tuned to a unique frequency [12]. The photometers are aligned in the nadir direction during the umbra portion of the satellite’s orbit. They collect airglow brightness data to extract gravity wave parameters including amplitude, horizontal and vertical wavelengths, and wave temperature. One channel provides a background measurement, a second channel provides an ultraviolet cut-off, and the remaining five channels study various O<sub>2</sub> emission frequencies. The arrangement of the photomultiplier tubes within the satellite does not affect the data produced [12]. The mass of the UIUC photometer payload is 1563.9 g, and it occupies a volume of 2178.5 cm<sup>3</sup>. Its key accommodation requirements are listed in Table 2.2. These requirements include functional requirements, such as PL-2, which ensures that the photometers are not damaged by sunlight and performance requirements, such as PL-6, that flow down to the bus.

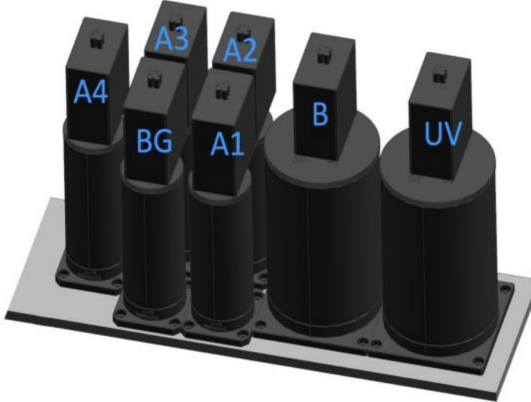


**Figure 2.2: Gravity Wave Detection Photometer Payload [12].**

**Table 2.2: Key payload requirements for the Gravity Wave Detection DRM [12].**

Req. ID	Requirement	Notes
PL-1	The Photometers shall collect measurements of nighttime airglow perturbations in the upper mesosphere.	<i>This is the primary science objective of the mission.</i>
PL-2	The Photometers shall operate during eclipse.	<i>This enables the photometers to detect faint airglow in the absence of sunlight.</i>
PL-3	The Photometers shall be aligned to nadir $\pm 10^\circ$ during operation.	<i>This requirement flows down to the ADCS subsystem and is essential for collecting usable data.</i>
PL-4	The Photometers shall be kept pointed $\geq 23^\circ$ away from the Sun.	<i>This protects the photometers from direct sunlight, even while not operating.</i>
PL-5	The Photometers shall have a 33 % average duty cycle per orbit.	<i>This is determined by the time in eclipse available for collecting data.</i>
PL-6	The Photometers shall consume $\leq 0.12$ W during standby.	<i>This contributes to the continuous power draw of the satellite.</i>
PL-7	The Photometers shall consume $\leq 2.7$ W during active operation.	<i>This flows down to the power storage requirement of the bus.</i>
PL-8	The Photometers shall pass data to the bus at a rate $\leq 21$ Bps.	<i>This data generation rate must be accommodated by the CDH subsystem.</i>

The Gravity Wave Detection mission is a useful DRM for establishing basic payload support capabilities. The derived performance requirements on the subsystems are easily met. However, the mass and volume of the payload necessitates a 6U bus. The size and number of photomultiplier tubes require a 2U area of external apertures to operate. These apertures need to be held in the nadir direction throughout payload operation.

The large aperture area and nadir pointing place significant constraints on the possible configurations of the bus. The payload-bus interface must support the 2.7 W power delivery required to operate the payload, as well as the 21 Bps data transfer rate while operating. All of these factors combine to create a DRM that establishes a key configuration capability of CUBE, while placing a relatively light load on its subsystems.

### 2.3.2 Sterile Neutrino Detection

The Sterile Neutrino Detection DRM is a CubeSat mission with the objective of characterizing a 3.5 keV X-ray signal hypothesized to be generated by sterile neutrinos, a theoretical particle that may be associated with dark matter. This signal has been identified by X-ray observatories in the past, but the observatories lack the resolution and field-of-view to properly characterize the signal. The DRM features specialized, wide field-of-view X-ray detectors developed by Fermi National Accelerator Laboratory (Fermilab) as the primary payload. The payload is used to correlate the 3.5 keV signal with regions of likely high dark matter concentration. Sagittarius A\*, the black hole at the center of our galaxy, is one such region and serves as the primary target of the DRM. The existence of a correlation with predicted dark matter concentrations would support the theorized sterile neutrino as an indicator of dark matter presence in a region. This DRM is an adaptation of the Dark matter as a sterile NEutrino Search Satellite (DarkNESS) mission, which is being developed in collaboration between Fermilab and UIUC [13].

The Fermilab payload consists of two charged-couple devices (CCDs), a beryllium window assembly, a coldplate, and an instrument computer. The CCDs each have a resolution of 80 megapixels and are shielded from lower energy signals by the beryllium window assembly. The back of the CCDs is bonded to a coldplate that interfaces with a thermal control system. The instrument computer includes a stack of three printed circuit boards (PCBs) housed in an instrument board box that is isolated from the Detector housing by standoffs [13]. The configuration of the payload is shown in a rendering in Fig. 2.3. The payload is used to take 15-minute exposures of the target to build up a sufficient signal to noise ratio. A key constraint of the payload is its sensitivity to thermal noise. In order to produce usable data, the CCDs must be kept below a maximum operational temperature of 170 K. This is accomplished through the use of active thermal control. A Ricor K508N Cryocooler, shown in Fig. 2.3, pumps a working fluid through a coldfinger to remove heat from a very small area. The coldfinger is attached to the coldplate of the Fermilab payload [13]. The heat output of the cryocooler can then be conducted to the passive thermal control system of the bus. However, the use of a cryocooler comes with a 9 W average requirement during payload operations [13]. The payload mass is 2061.2 g and it occupies a volume of approximately 2000 cm<sup>3</sup>. The key requirements for the payload are listed in Table 2.3.

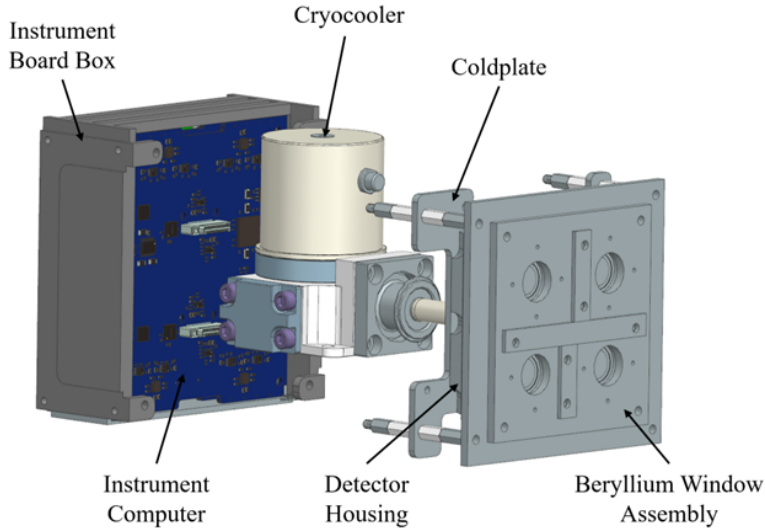


**Figure 2.3:** Sterile Neutrino Detection X-ray Imager Payload [13].

**Table 2.3:** Key payload requirements for the Sterile Neutrino Detection DRM [13].

Req. ID	Requirement	Notes
PL-1	The Instrument shall collect images of the galactic center.	<i>This is the primary science objective of the mission.</i>
PL-2	The Instrument shall use an external aperture on the ram face of the Bus.	<i>This was determined to be the optimal payload configuration by preliminary design analysis.</i>
PL-3	The Instrument shall be aligned to the galactic center $\pm 5^\circ$ during observation periods	<i>This is essential for collecting useful images that contain the target.</i>
PL-4	The Instrument shall have a 27 % duty cycle per orbit during science periods.	<i>This is determined by the 15-minute integration time of each image.</i>
PL-5	The Instrument shall consume $\leq 2.4$ W during standby.	<i>This power is drawn from the bus throughout mission operations.</i>
PL-6	The Instrument shall consume $\leq 12$ W during active operation.	<i>This takes place during eclipse and flows down to the power storage capability of the bus.</i>
PL-7	The Cryocooler shall consume $\leq 9.6$ W during active operation.	<i>This is essential for regulating instrument temperature.</i>
PL-8	The Instrument shall pass data to the bus at a rate $\leq 32$ MB per orbit during science periods.	<i>This data is processed and stored by the bus until a communication session occurs.</i>
PL-9	The Instrument Sensor temperature shall be $\leq 170$ K during active operation.	This temperature limit is crucial for achieving an acceptable signal to noise ratio.

The Sterile Neutrino Detection mission represents a moderate 6U tier CubeSat mission. The payload needs a 1U aperture on the ram face of the satellite. It also has strict thermal requirements that favor a different bus layout than the Gravity Wave Detection mission. Heat must be removed from the detector assembly efficiently to maintain its operating temperature below 170 K. Simultaneously, the structure must house the instrument computer, which produces additional heat. The payload-bus interface must be capable of supplying the detector and cryocooler with a combined 21.6 W when both are operating. This is a relatively large amount of power for a 6U CubeSat. The 32 MB raw images generated by the payload must also be transferable across the interface for timely downlink of collected data. This is a mission that demands significant bus capabilities and presents interesting interface and structure layout challenges. As a DRM, the Sterile Neutrino Detection mission provides a mission profile that is representative of an important class of CubeSat observatory payloads

### 2.3.3 Water Quality Monitoring

The objective of the Water Quality Monitoring DRM is to collect hyperspectral images of lakes and coastal water as tasked by ground operators. The hyperspectral data can be used to measure a variety of water quality metrics including, chlorophyll concentration, turbidity, suspended sediment load, and dissolved organic material. Each of these metrics are physical properties that can be correlated with the spectral content of images of water. The metrics provide direct characterization of conditions, such as phytoplankton presence, that determine water quality [14]. Collecting this hyperspectral data from an orbiting CubeSat platform enables characterization of important trends and temporal patterns over the lifespan of the mission. It further enables the monitoring of remote inland water bodies that are not easily accessible by land. The CubeSat also serves as an asset in disaster response, as it can be tasked to prioritize imaging regions with rapidly developing water quality threats.

The Simera Sense HyperScape100 is the primary payload for this DRM. The HyperScape100, shown in Fig. 2.4, is a commercially available hyperspectral imager that fits in a 1.5U volume. It consists of a CMOS sensor, optical front end, and on-board electronics. The CMOS sensor operates in a push broom configuration and is capable of imaging in 32 spectral bands within the visible and near-infrared range. The optical front end uses a modified Cassegrain design to achieve a 580 mm focal length and 2.22° field-of view. The on-board electronics sit behind the sensor and offer data storage and image reduction functions [15], [16]. The total mass is 1260.0 g and is accommodated by a volume of 1706 cm<sup>3</sup>. The mission will operate at an altitude of 500 km in order to achieve the smallest possible ground sample distance (GSD) of 4.75 m [15]. This results in a need for bus pointing accuracy on the order of arcseconds. The pointing requirement detailed in PL-3

equates to an uncertainty of 0.01 % of the payload's field-of-view. Table 2.4 lists the key requirements for the Water Quality Monitoring DRM.

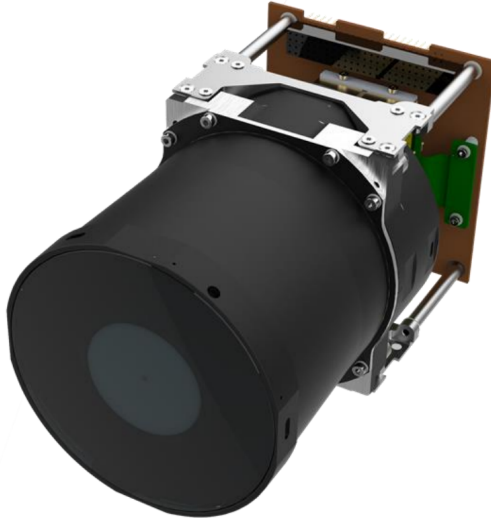


**Figure 2.4: Water Quality Monitoring Hyperspectral Imager Payload [16].**

**Table 2.4: Key payload requirements for the Water Quality Monitoring DRM [15].**

Req. ID	Requirement	Notes
PL-1	The Payload shall collect hyperspectral images of coastal waters and lakes.	<i>This is the primary science objective of the mission.</i>
PL-2	The Payload shall operate during the antumbra portion of its orbit.	<i>The hyperspectral imager relies on external energy, in the form of sunlight, to collect data.</i>
PL-3	The Instrument shall be aligned to nadir $\pm 79.92''$ during observation periods.	<i>This pointing precision is essential for collecting clear images at the high magnification of the optical system.</i>
PL-4	The Payload shall have a 30 % duty cycle per orbit.	<i>This allows the payload to be available for tasking while conserving bus resources over regions without water.</i>
PL-5	The Payload shall consume $\leq 4.0$ W during standby.	<i>This power is needed throughout all mission operations.</i>
PL-6	The Instrument shall consume $\leq 7.75$ W during active operation.	<i>This power is consumed during the 30 % duty cycle of the payload.</i>
PL-7	The Payload shall pass data to the bus at a rate $\leq 9.22$ MBs.	<i>This data generation rate is the combined output of all of the spectral bands of the imager.</i>

The Water Quality Monitoring mission has a variety of factors that make it a demanding mission for a 6U bus. The high magnification of the payload's optical front end results in the need for a large, nadir facing aperture with almost 2U of volume behind the aperture. This requires careful consideration of the component layout to create a balanced system, as the payload must be very precisely pointed to collect clear data. The payload is required to operate during the sunlit portion of the orbit, meaning that the bus must be able to generate power without entering a dedicated sun tracking mode. The payload-bus interface must supply the hyperspectral imager with 7.75 W during payload operation. The interface must also accommodate the large data generation rate of the payload. At 9.22 MBps with all spectral bands enabled, the data rate of the payload exceeds what many simple data protocols are capable of handling. The Water Quality Monitoring mission serves as a DRM that stretches the limits of payload accommodation in a 6U form factor.

# Chapter 3

## Modular Structure Design

This chapter describes the modular design of CUBE in detail. Module configurations, interfaces, and the layout of internal components are discussed. Analysis of the center of gravity in various configurations is presented, leading to a definition of the allowable payload center of gravity envelope. The design is then applied to each of the three DRMs introduced in Chapter 2, and the system’s ability to accommodate a variety of payloads is established. The chapter concludes with an introduction to the prototype of CUBE that was manufactured for testing.

### 3.1 Module Designs and Configurations

CUBE, shown in Fig. 3.1, is designed to prioritize payload accommodation flexibility. Each module is shaded with a different color for clarity. It has the overall dimensions of a standard 6U CubeSat structure and is divided into three pieces. Each module is made from 6061-T6 aluminum. M1 and M2 both contain bus hardware.

The third module is the PM, which hosts all payload components. It features large external facing apertures on all six faces for remote sensing payloads. The PM also has a grid of uniformly spaced screw clearance holes for mounting payload hardware. The exterior faces of each module sit flush with four rails, that run along the corners of the structure, except for the end faces. The rail ends extend past the structure providing a standoff height as required by the CubeSat Design Standard [2]. The standoff height creates 7.5 mm of space for deployables on the end faces. Volume available for deployables on the remaining sides of the structure is determined by the deployer selected for each mission.

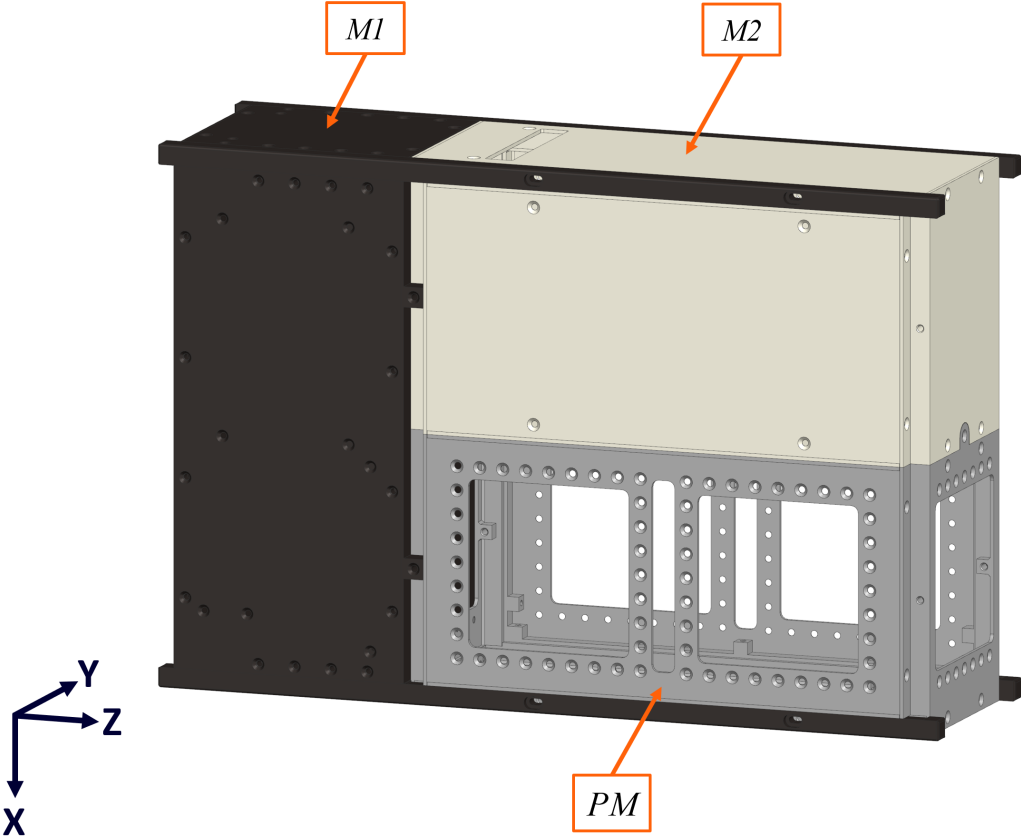


**Figure 3.1: CUBE with M1, M2, and PM assembled together into one of the available configurations.**

The three modules can be rapidly integrated to streamline AIT of the spacecraft. Fig. 3.2 shows the process for assembling the three modules to form a 6U CubeSat structure. M1 serves as the backbone of CUBE with four rails that span its full length. These rails serve a dual purpose. They provide a CubeSat Design Standard compliant deployer interface while also supporting the PM and M2 [2]. In Step 1 of the module assembly procedure, the PM is attached to M2 using two fasteners. These two modules are dimensioned such that they form a square box of approximately 1U x 2U x 2U size. There is an 8.5 mm square channel along each outside edge that fits a rail. These channels allow the assembled PM and M2 to slide between the rails of M1. The insertion of the two modules is shown in Step 2 of the assembly procedure. In Step 3, the prepositioned modules are attached using two fasteners through each rail and four additional fasteners through support blocks on M1. The small number of fasteners and simple interface between modules dramatically reduces integration complexity and allows the process to take place in a matter of minutes.

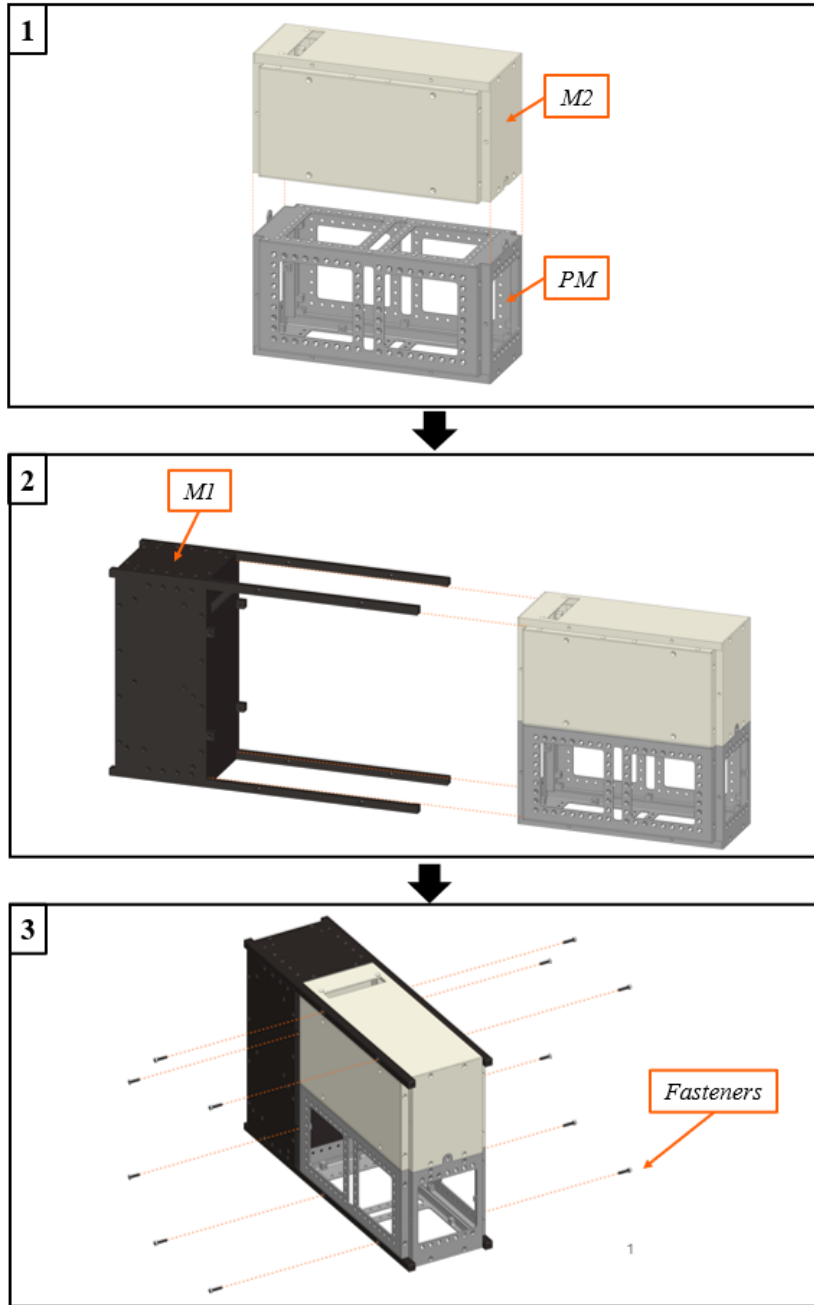
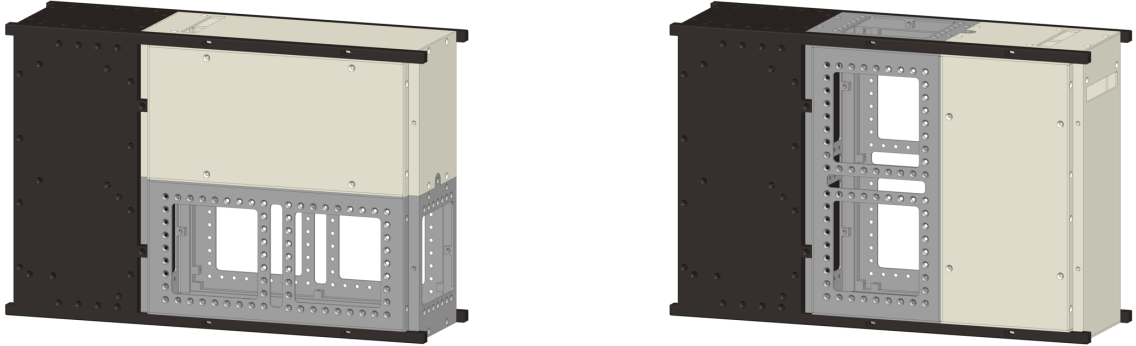


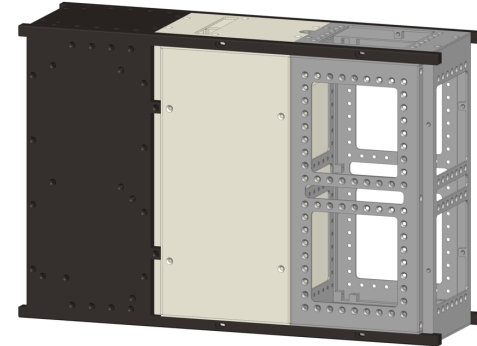
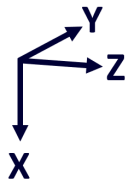
**Figure 3.2: Three-step module assembly procedure.**

Reconfigurability is one of the primary innovations provided by CUBE. Each module is self-contained and can interface with other modules through a single power and data connector. Because of this, the PM and M2 can be slid between the rails of M1 in any of three configurations without any modification to the modules themselves. These configurations are shown in Fig. 3.3. Each configuration offers different payload hosting capabilities. The external apertures available to payloads total at least 2U on five of the six faces of the structure.



**Config. A –** Tall payloads have view of zenith direction or large view of ram direction.

**Config. B –** Heavy payloads can reside close to the geometric center.



**Config. C –** Payloads can have views of ram, anti-ram, and nadir directions

**Figure 3.3:** Available configurations of CUBE illustrate the flexible accommodations provided by the design.

Providing aperture flexibility without custom subsystem modifications is not possible in traditional CubeSat structures. The three configurations also offer payload providers the opportunity to balance the center of gravity and moments of inertia to achieve their mission objectives. Thermal control of the payload can also benefit from the selection of a configuration that provides a field of view to sunlight or dark space as needed.

The design of the bus modules employs a monocoque construction that combines the open frame and flat panel elements typically present in CubeSat structures. In a traditional CubeSat structure, an open frame provides a rigid load path between all internal components and the rails. This results in a small structure mass on the order of 750 g [17]–[19]. It is then often necessary to cover the frame with solid metal panels for protection from micro-meteoroid orbital debris (MMOD) and for the mounting of external components. This, in turn, increases the overall mass of the traditional structure. The monocoque design of CUBE provides a rigid load path for internal components while also enclosing each module. This is accomplished with geometrically stiffened panels, as shown for M2 in Fig. 3.4.

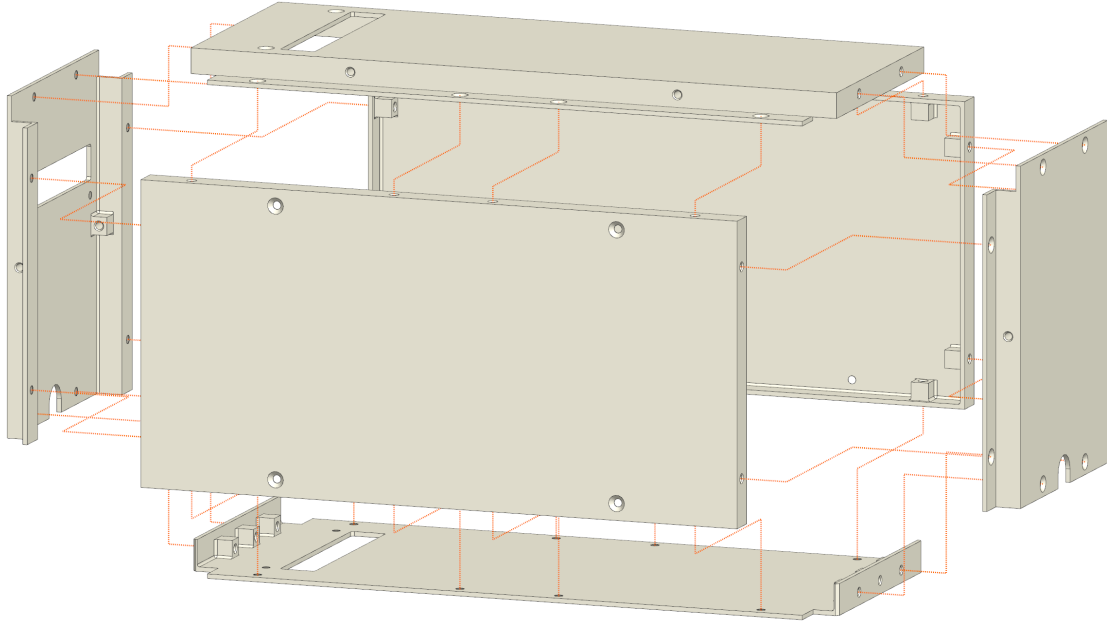


**Figure 3.4: Exploded view of bus M2 showing its monocoque construction.**

The panels are milled out of aluminum stock to maximize internal volume and create channels for the rails that also stiffen the part. The panels are assembled using countersunk machine screws that fasten into threaded inserts in the panels. One drawback of dividing a 6U CubeSat into three modules is that it results in extra structure that can restrict internal volume. Because of this, the structure is designed to provide efficient load paths to maximize internal volume and be able to accommodate COTS subsystem components. The monocoque design of the modules provides this necessary efficiency along with the added benefits of fewer parts and simplified assembly procedures.

## 3.2 Interface Definitions

CUBE is a system of systems comprised of many constituent elements. The interactions between these elements are governed by their interfaces. This thesis focuses on the interfaces within CUBE as they relate to the design of the structure. Fig. 3.5 provides an Interface Control Diagram (ICD). In this diagram, M1, M2, and the PM are shown with boundaries depicted by gray shaded rectangles. Launch Systems and Ground Operations, the two other high-level systems that the CubeSat interfaces with, are illustrated in a similar manner. The ICD legend explains the color-coding for subsystem components in the modules.

There are three types of interfaces defined by the ICD: data connections, power connections, and structure connections. Data interfaces, denoted by green arrows, exist between all of the active subsystem components and the Command and Data Handling (CDH) Main Board. Data interfaces between CUBE and the ground

operations are accommodated via the Communications Subsystem (Comms). Power from the batteries and solar arrays is sent through the Power Distribution Unit (PDU) to all other subsystem components and is denoted with yellow arrows. The structure interfaces with every element of the system to physically constrain all components throughout the mission. The structure also interfaces with the Deployer in the Launch System. This external interface constrains the physical dimensions and geometry of CUBE.

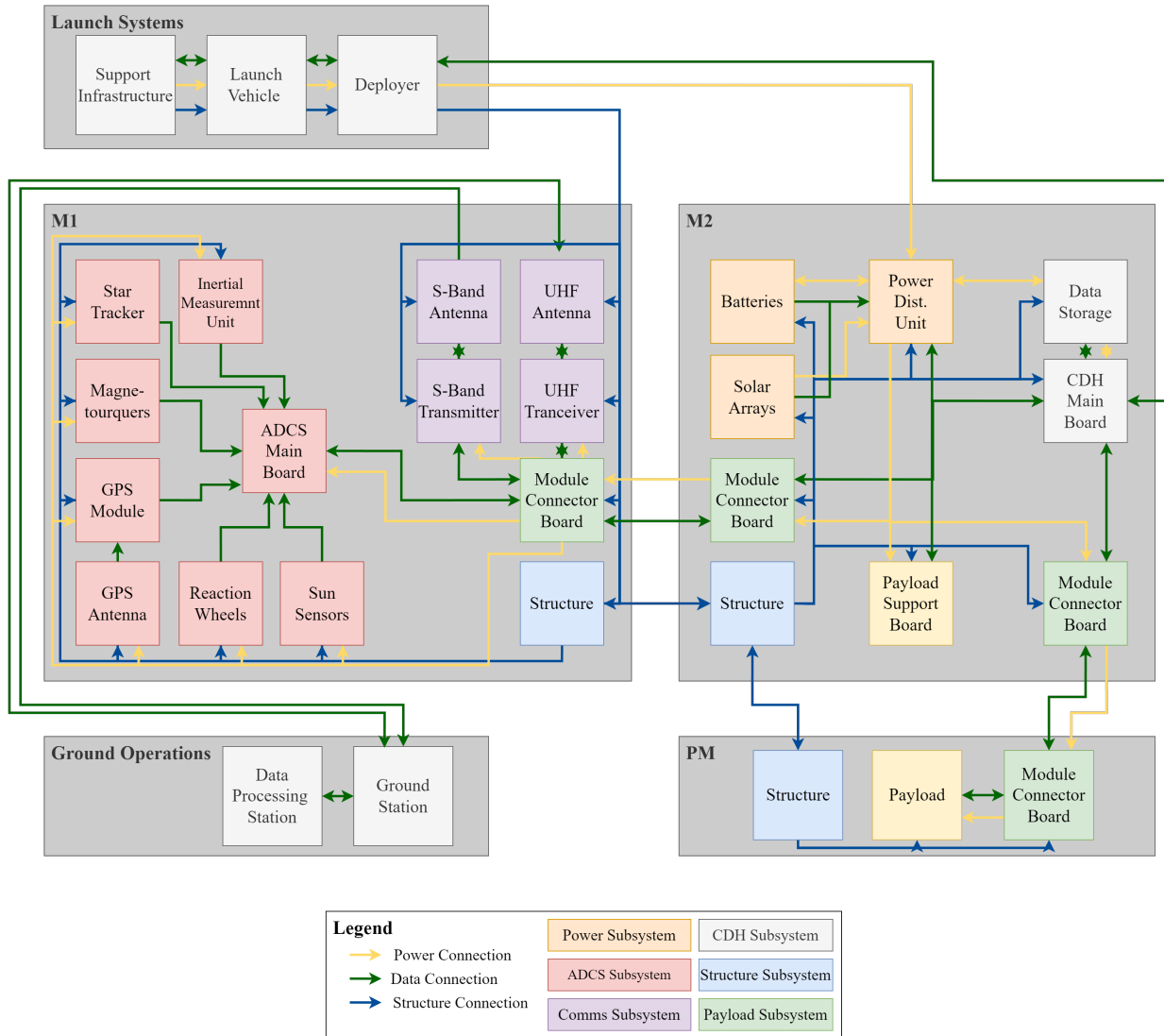


**Figure 3.5: The CubeSat System of Systems incorporating CUBE.**

The design of CUBE introduces more partitions than are typically present in a CubeSat system. The interfaces at each of these partitions are of particular interest for the structural design and are supported by the system of rail and support block fasteners previously described. A common electrical ground throughout the structure is created by uncoated metal contact at this interface. The large contact area also provides good thermal conduction between modules.

Data and power must be passed between the three modules. As shown in Fig. 3.5, This is accomplished by a single Module Connector (MC) on either side of the module interface. The design of the MC is complicated by the multiple structure configurations that must be supported. The interface must pass all necessary data and power throughout the bus regardless of structure configuration. A MC is also used to connect the payload to the rest of the satellite. Payloads will use a CSK 104-pin mating connector that meets all of the interface specifications, as defined by Pumpkin Space Systems [20]. The pins are rated for 5.7 A and arranged in four rows with a pin pitch of 0.1 inches. However, the communication protocols used by the component boards varies between vendors. The MCs are passive components that provide a reliable path for power and data between the modules. Because they are passive, their pinout and data protocol are determined by the subsystem hardware on either side of the connector. The maximum data rate is set by the data protocol implementation.

In order to support all module configurations, M1 is fitted with a female MC that extends past the side panel that it is mounted on. M2 is fitted with three male MCs that sit flush with the side panels they are mounted on. One connector is dedicated to the PM interface, one is dedicated to the Config. A bus module interface, and one is dedicated to the Config. C bus module interface. For the special case of Config. B, where the PM sits between the two bus modules, an additional MC and adapter board is fitted inside the PM. A key feature of the MCs on M2 is that the unpopulated connectors do not protrude past the surface of the structure. This means that they do not interfere with the deployer or any externally attached components and can be capped. The mating MCs for Config. C are shown in Fig. 3.6.

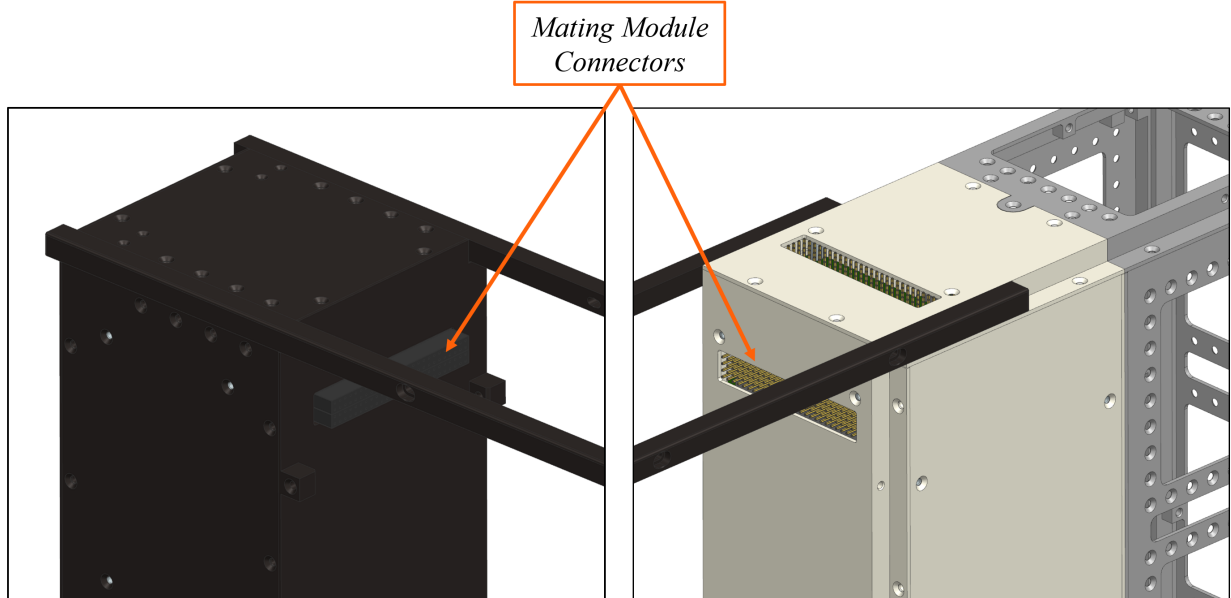


**Figure 3.6:** Mating MC placement of M1 (left) and M2 (right).

M2 requires custom hardware to correctly route the 104 conductors of the interface to three different MCs. The Stack Splitter, shown in Fig. 3.7, accomplishes this task with a set of PCBs connected by card edge connectors. The base of the Stack Splitter stacks on top of the internal subsystem components of M2. The remaining PCBs are each fastened to a side panel with standoffs to withstand the mating force of the MCs and provide a flat exterior. The traces on the PCBs mirror the pinout of the internal component stack vertically and/or horizontally to route each pin to the corresponding pin in a neighboring module. The card edge connectors provide the  $90^\circ$  rotation needed to reach each side of M2. They form a rigid connection that is reliable and does not suffer from the induced signal noise issues caused by other solutions such as ribbon cables.

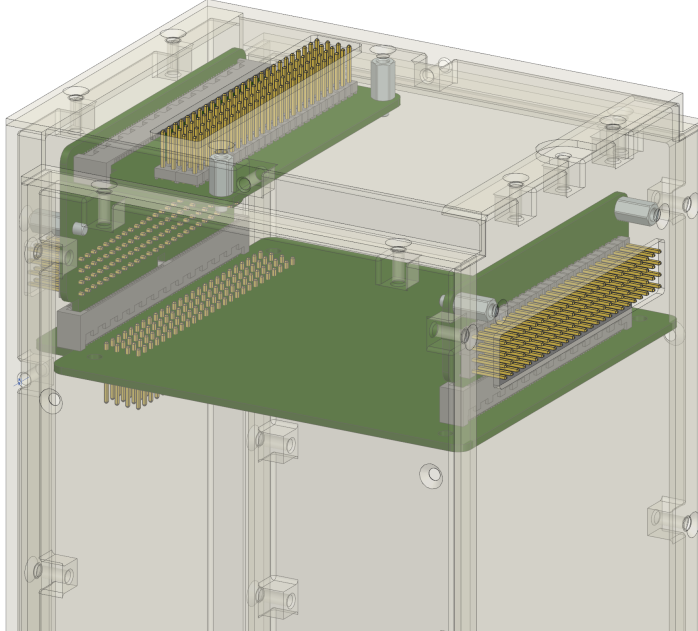


**Figure 3.7: Stack Splitter inside M2 adapts board stack (not pictured) to three MCs.**

The MC is used to interface with the PM and subsequently the payload itself. However, a more sophisticated CDH interface is needed between the payload and the rest of the bus subsystems in order to promote payload flexibility. This interface is implemented in CUBE as a Payload Support Board (PLSB). Fig. 3.8 shows a schematic of a prototype of the PLSB. It was originally designed as a kit for STEM outreach, where students could select sensors utilizing the MikroBus™ standard and program the PLSB to create a payload for a 1U CubeSat [21]. A flight version of the PLSB was produced and flown as a secondary payload on the Space Entanglement and Annealing Quantum Experiment (SEAQUE) mission on the ISS.

The physical dimensions and hole pattern of the PLSB are modified to be PC-104 bus compliant for use in the CUBE system. The PLSB uses an STM32L552 to coordinate its operations as an intermediary between

the payload and the CDH subsystem. It supports onboard storage of up to 32 GB using a commercial-grade MicroSD card. A set of pins in the MC are allocated to the PLSB for communicating with the payload and controlling power to the payload. I<sup>2</sup>C, SPI, and UART protocols are supported for transfer of data and issuing payload commands.

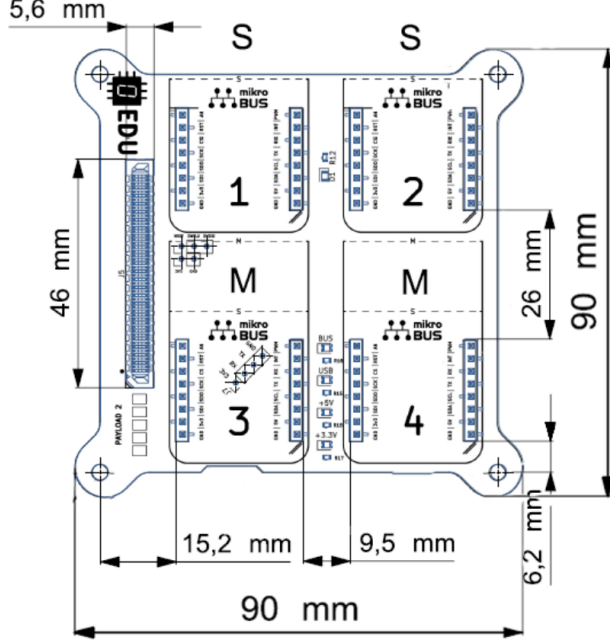


**Figure 3.8:** Prototype PLSB supporting MikroBUSTM interface [21].

### 3.3 Internal Layouts

CUBE makes 4U of volume available for bus hardware split between M1 and M2. Able to support a wide range of payloads, the set of subsystem components, selected to provide highly capable performance, fit within the 6U form factor of the structure. To avoid costly custom designs, a set of baseline flight-proven COTS subsystem components have been identified that provide the CubeSat with the functions and performance to satisfy the previously defined DRMs. These components were selected by surveying vendors listed in the NASA State-of-the-Art Small Spacecraft Technology Report [22]. Trade studies were then performed to down select from competing solutions.

Where possible, the components were sourced from a single vendor to reduce the risk of compatibility issues. Capable CDH and Comms subsystems are available from AAC Clyde Space. The Power subsystem is also produced by AAC Clyde Space, except for the solar arrays that are sourced from Blue Canyon. The AAC Clyde Space PCBs feature the same 104 pin connector utilized throughout the bus as an interface and

are designed to be stacked on one another. They also have PC-104 bus compatible mounting holes that simplify the design of supporting brackets. The Attitude Determination and Control System (ADCS) features components from CubeSpace. Their modular approach to sensors and actuators allows for a more efficient internal layout than what would be possible with an all-in-one ADCS unit. The selected hardware is listed in Table 3.1 along with the subsystem, vendor, and model.

**Table 3.1: CUBE subsystem component list.**

Subsystem	Component	Vendor	Model
CDH	Main Board	AAC Clyde Space	Kryten-M3 PLUS
CDH	GPS Antenna	AAC Clyde Space	ANT-GPS
Payload Support	Payload Support Board	N/A	PLSB
Comms.	UHF Transceiver	AAC Clyde Space	Pulsar-UTRX
Comms.	UHF Antenna	AAC Clyde Space	ANT-100
Comms.	S-Band Transmitter	AAC Clyde Space	Pulsar-HSTX
Comms.	S-Band Antenna	AAC Clyde Space	Pulsar-SANT
Power	Power Distribution Unit	AAC Clyde Space	Starbuck-Nano-Plus
Power	Battery Pack	AAC Clyde Space	Optimus-80
Power	Solar Arrays	Blue Canyon	6U-V Double Panel
ADCS	Main Board	CubeSpace	Core Module
ADCS	Reaction Wheels	CubeSpace	CW0057
ADCS	Magnetorquers	CubeSpace	CR0008
ADCS	Star Tracker	CubeSpace	CubeStar
ADCS	Sun Sensor	CubeSpace	Coarse Sun Sensor

The layout of the selected subsystem components must account for the orientation of the satellite in the space environment, as well as the module orientations possible with the three supported structure configurations. Because the rails are attached to M1, that module stays in a fixed position regardless of the selected configuration. Fig. 3.9 shows the layout of subsystem components within a see-through rendering of M1.

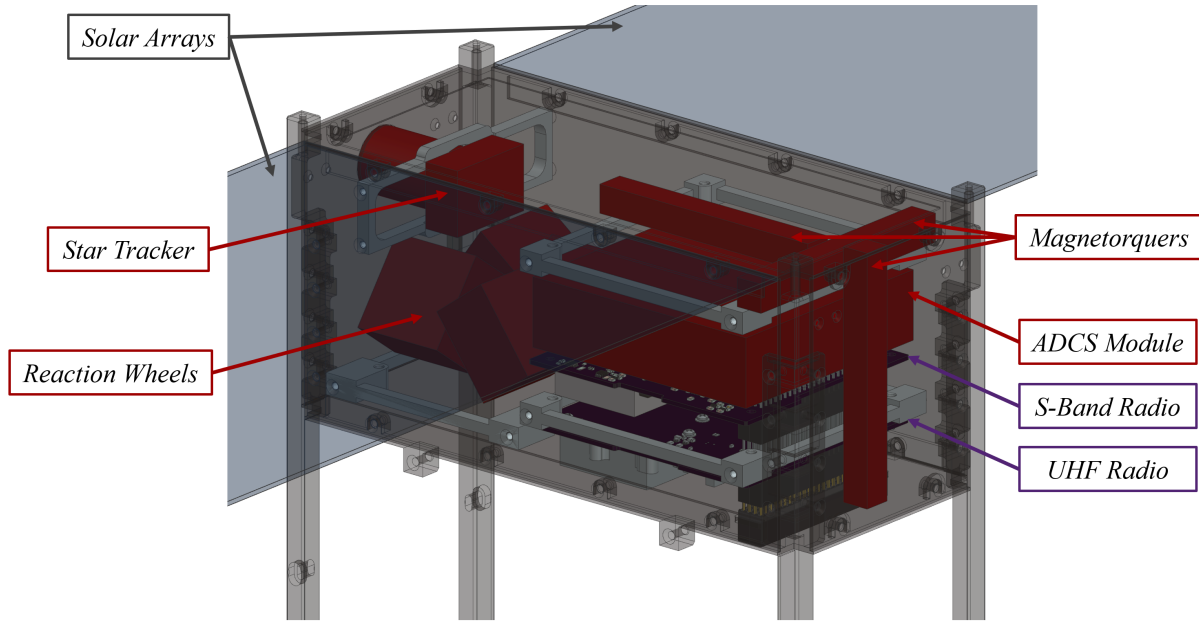


**Figure 3.9: Internal layout of M1.**

The solar arrays are attached to the 2U edges of M1, making it the “top” of the satellite for many mission profiles. The 2U x 1U face points toward the sun in sun-tracking phases, or in the zenith direction during nadir-tracking phases. ADCS and Comms subsystems are contained within this module. The right side of the figure shows three components in a stack. There is a UHF radio for transmitting and receiving commands, and an S-Band radio for high-speed data downlink.

The third component is the main board of the ADCS subsystem, which interfaces with the sensors and actuators distributed throughout the module. Four reaction wheels are mounted in a pyramid configuration for redundant control authority over the three axes. The reaction wheel assembly is one of the heaviest subsystem components and is mounted as close to the center of the structure as possible. The star tracker sits above the reaction wheels with an aperture in the 1U end face of the module. This allows the star tracker to point toward deep space for a large portion of the orbit with little or no attitude change. Three magnetorquers are mounted at the other end of the module in a “T” configuration to desaturate the reaction wheels when necessary. Sun sensors (not pictured) provide coarse attitude knowledge for detumbling after deployment and during other mission phases as needed. An S-Band patch antenna, UHF whip antenna, and GPS patch antenna are mounted on the exterior faces of the module.

The layout of the remaining subsystem hardware in M2 is shown in Fig. 3.10. The hardware consists entirely of PC-104 bus compatible hardware. It is arranged in a single board stack that plugs into the bottom of the Stack Splitter.

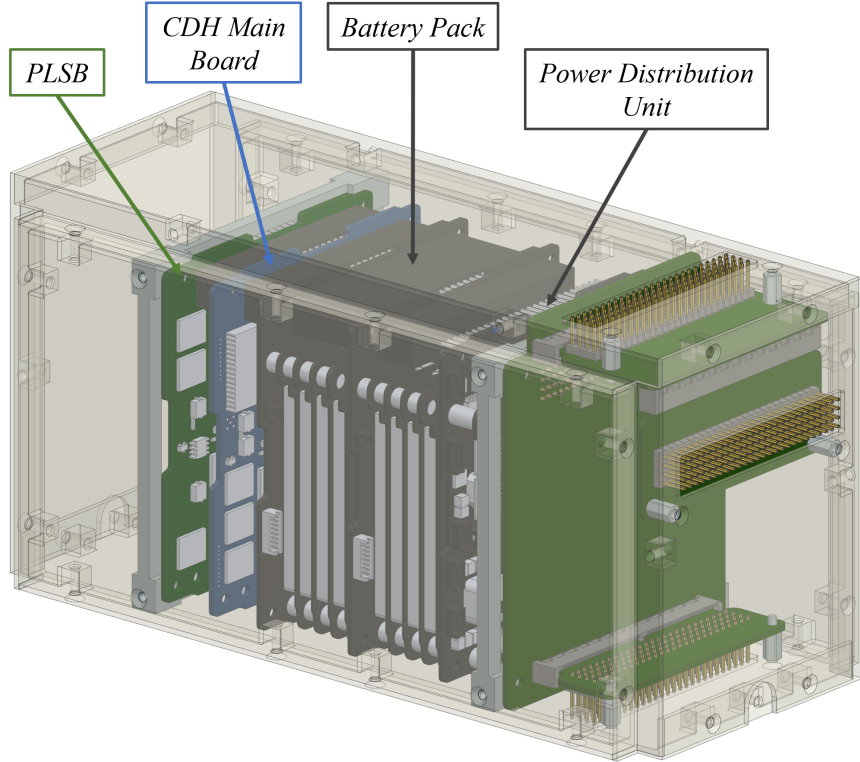


**Figure 3.10: Internal layout of M2.**

Starting from the left, the PLSB provides payload interface functions through the Stack Splitter. The CDH main board is next in the stack with an ARM Cortex-M3 processor that runs a real time operating system to reliably monitor and manage all of the subsystems. The battery pack sits at the center of the module because of its high mass. It provides 80 Whr of capacity using flat lithium-ion cells. The power distribution unit is mounted between the battery pack and the Stack Splitter. It provides 3.3 V, 5 V, and 12 V power rails to the bus interface.

### 3.4 Mass and Center of Gravity Constraints

For a 6U with a maximum mass of 12 kg dictated by the CubeSat Design Standard, payload mass is calculated by subtracting off the mass of the rest of the satellite. A mass budget is a necessary tool for tracking the mass of the system as it progresses through the systems engineering design cycle. Each item in a mass budget is assigned a mass growth allowance (MGA) based on its current development maturity. A prototype component is assigned a large MGA, while an already-manufactured flight unit is assigned no MGA. Estimated mass is then calculated using each basic mass and its MGA.

The estimated masses are summed to get a subtotal mass, and an additional mass reserve is applied to reach the total system mass. Table 3.2 enumerates a condensed mass budget for CUBE.

**Table 3.2: Condensed mass budget for CUBE.**

Item	Mass	MGA	Estimated Mass
Structure	1.5814	1%	1.597
Fasteners	0.0385	1%	0.039
Secondary Structure	0.3055	3%	0.315
Subsystem Components	3.4299	5%	3.601
Stack Splitter	0.08	5%	0.084
Connectors	0.011	5%	0.012
Harness	0.06	10%	0.066
Solar Arrays	1.5	10%	1.650
Body Solar Cells	0.0052	10%	0.006
UHF Antenna	0.04	5%	0.042
S-Band Antenna	< 0.05	0%	0.050
GPS Antenna	0.018	5%	0.019
<b>Subtotal:</b>			7.480
<b>Reserve (3.6%):</b>			0.270
<b>Total:</b>			7.750

The structure and fastener masses are assigned a very small MGA, as they are measured from physical hardware. The COTS subsystem components have been compiled into a single item with a moderate MGA. The remaining components have more uncertainty and are given higher associated MGAs. A 3.6 % reserve is applied to the subtotal, leading to a total mass of 7.75 kg. This leaves 4.25 kg of the maximum 12 kg available as allowable payload mass.

Managing the Center of Gravity (CG) of a CubeSat is critical for achieving a safe deployment on orbit and a controllable system when maneuvering. Deployer companies provide requirements for allowable CG locations to avoid binding of the CubeSat rails in the deployer as the CubeSat is released. The allowable envelope varies between deployer companies. Since CUBE is designed to be used for a variety of missions, launch vehicles, and deployers, its CG must comply with as many deployers as possible. The CubeSat Design Standard lists requirements for CG location relative to the geometric center. The CubeSat Design Standard requirements are intended to encompass the majority of deployers currently available. The allowable envelope

is defined in each axis. The CG can be  $\pm 45$  mm in the 2U X axis,  $\pm 20$  mm in the 1U Y axis, and  $\pm 70$  mm in the 3U Z axis [2].

The CG of CUBE must also fall within the allowable envelope with a variety of payloads. This is determined by first calculating the CG of the structure and its subsystem components without a payload present. A placeholder payload is then positioned at different locations within the PM to find the boundaries of the allowable CG envelope. For this analysis, the payload placeholder was modeled as a 1 cm cube of sufficient density to make its mass be the maximum 4.25 kg allowable. Since the CG location is different for each configuration, the analysis was performed for all three structural configurations. The results for Config. A are shown in Fig. 3.11.

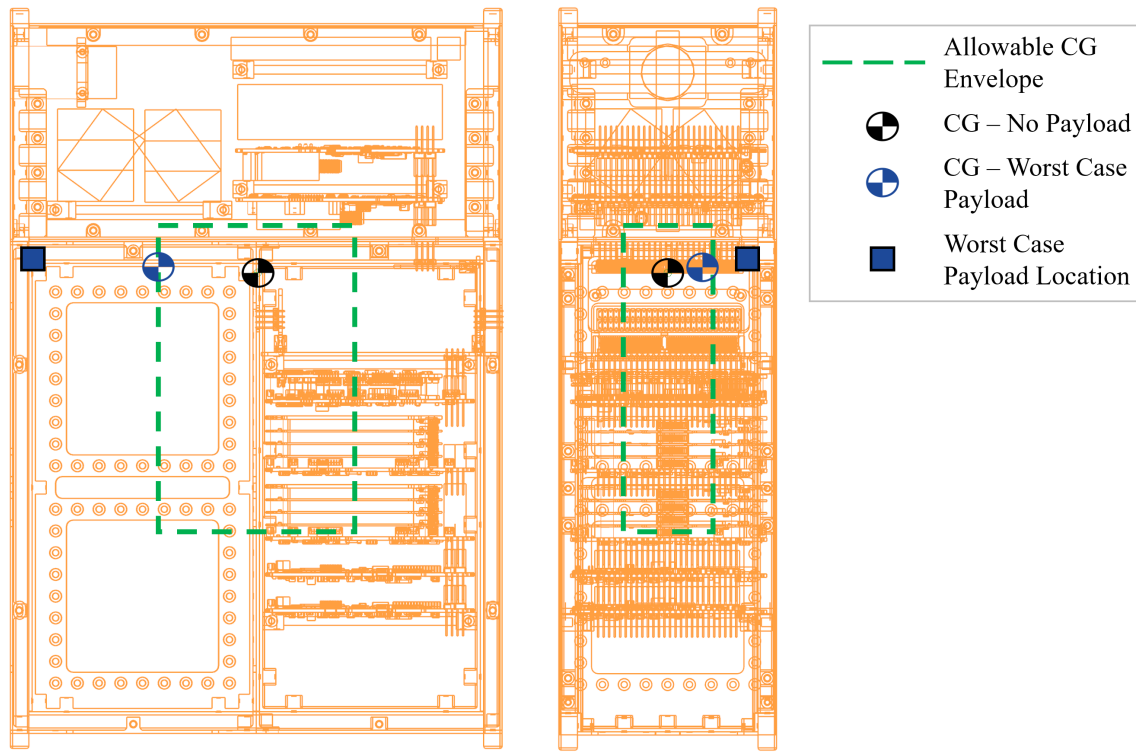


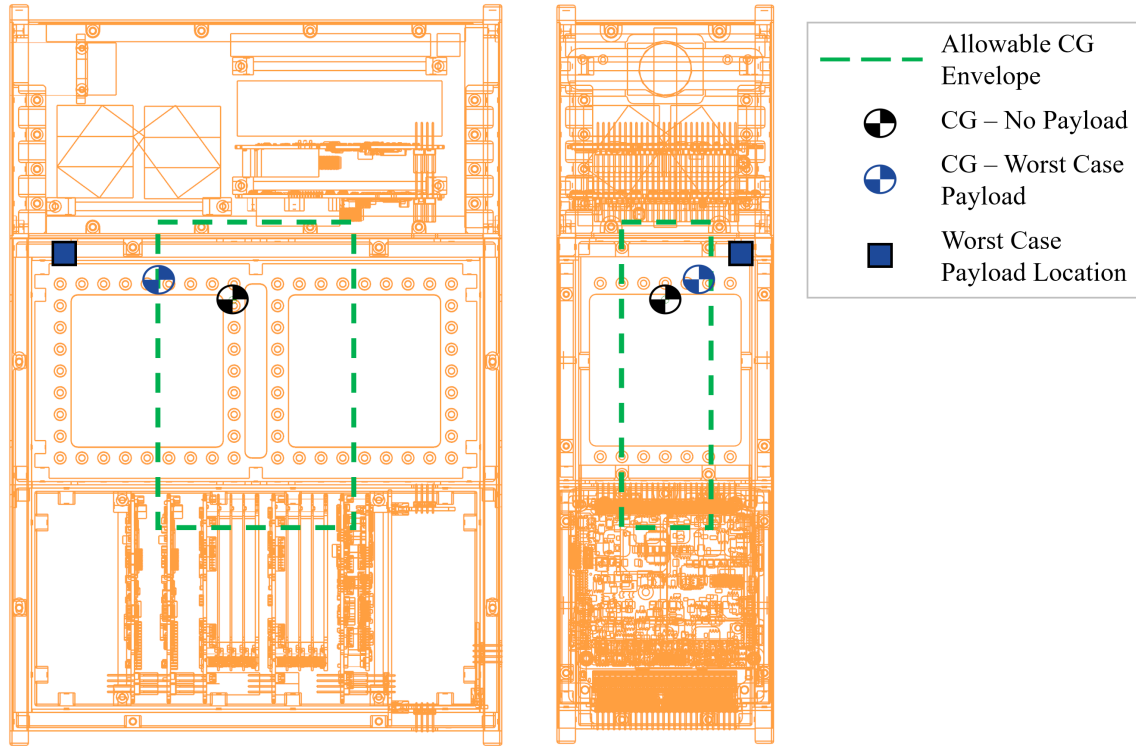
**Figure 3.11: Center of gravity characteristics of Config. A.**

The allowable envelope, as defined by the CubeSat Design Standard, is represented by a green dashed rectangle. The CG of CUBE without any payload is marked with a black icon. The worst-case location of the payload placeholder is highlighted with a blue square and the corresponding CG location is marked with a blue icon. The CG without payload is already within the allowable envelope, although it is pulled to the top end by the heavier ADCS hardware in M1.

The worst-case location found for the payload placeholder positions its center 9 mm from the outer X face, 13.5 mm from the outer Y face, and 6.5 mm from the outer Z face. This results in a full system CG

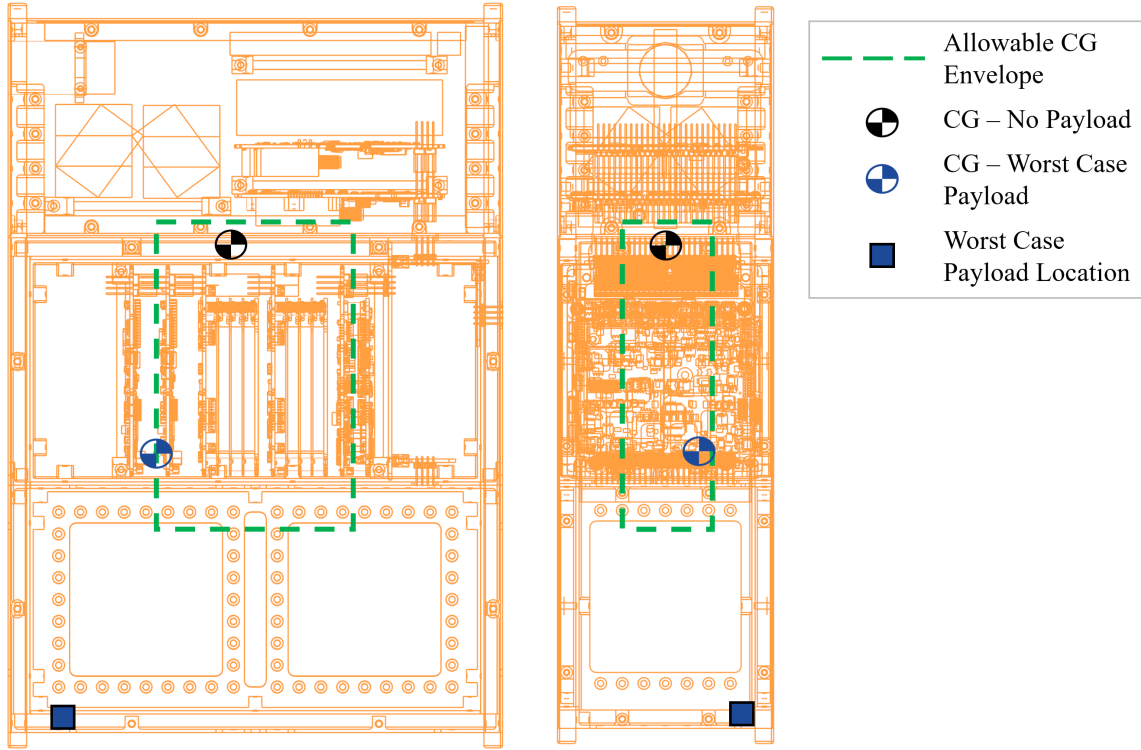
that is on the edge of the allowable X axis envelope with significant margin left in the Y and Z axes. For this configuration, the Y and Z axis locations are limited by the volume occupied by the rail. It is also worth noting that the density of the payload placeholder is likely higher than that of any real payload. This reinforces the analysis results as being a worst-case limit that actual payloads would be geometrically challenged to reach.

Fig. 3.12 shows a comparable analysis of Config. B. In this layout, the CG without payload is closer to the geometric center due to the more balanced location of M2. There is no payload placeholder location within the PM that can pull the system CG out of the allowable envelope in the Z axis. Similarly, the payload placeholder can be positioned against the inside of the rail in the Y axis leaving 4.5 mm of allowable envelope available. However, the X axis location of the payload placeholder is constrained by the allowable envelope. The worst-case location of the payload placeholder center is 23.5 mm from the outer X face, 13.5 mm from the outer Y face, and 5 mm from the outer Z face. Again, this does not practically limit the placement of physical payloads within the PM, although the X axis constraint is potentially influential.



**Figure 3.12:** Center of gravity characteristics of Config. B.

The final configuration, Config. C, is shown in Fig. 3.13. The CG without payload is shifted to the upper Z end of the allowable envelope. This is to be expected with the empty PM sitting at the bottom of the structure. The CG without payload is high enough that the payload placeholder can be positioned against



**Figure 3.13: Center of gravity characteristics of Config. C.**

the lower panel of the PM without pulling the system CG outside of the allowable envelope in the Z axis. The Y axis constraint of the payload is the same as the other two structure configurations, limited only by the rails. The X axis placement is once again constrained by the allowable envelope. Ultimately, the worst-case payload placeholder location was found to be 23.5 mm from the outer X face, 13.5 mm from the outer Y face, and 5 mm from the outer Z face. These constraints are identical to those found for Config. B.

It is possible to achieve a system CG located at the geometric center in both Config B. and Config C. This is easily accomplished in Config B. with the central location of the PM. Config C. would require a high-mass payload positioned in the upper portion of the module. It is not possible to align the CG with the geometric center in Config. A. The Y and Z axes can be centered. However, any payload mass will pull the CG off of the X axis center. This is not a concern for the majority of payloads but may be a consideration for certain physics or biological payloads requiring special maneuvering capability.

The CG analysis presented leads to payload placement constraints that can be defined with a single allowable payload CG envelope. This envelope is identical for all three structure configurations to simplify interface compliance for payload providers. Fig. 3.14 shows the allowable envelope as a green volume in cross section. The envelope is symmetrical about all three center planes. The payload CG can be up to 23.5 mm from either 1U end, 13.5 mm from the 2U sides, and 9 mm from the top and bottom.

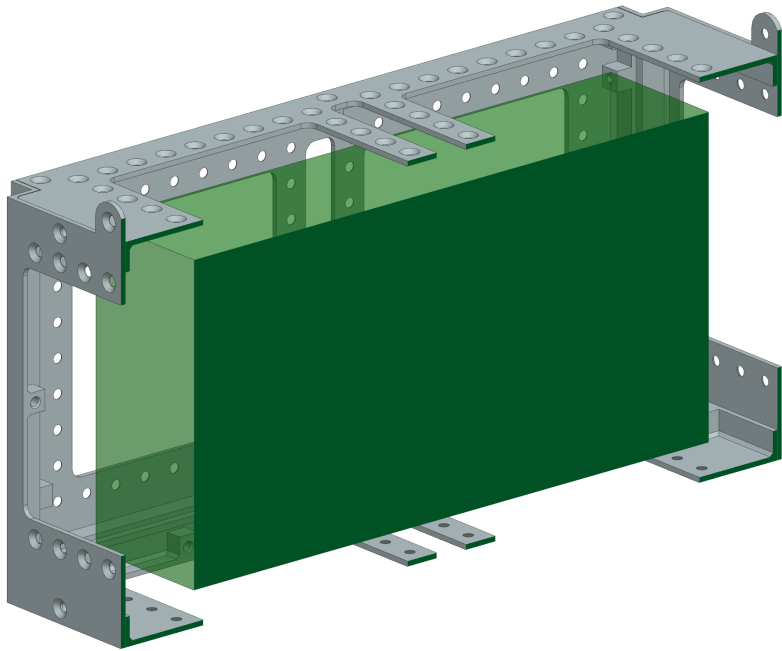


**Figure 3.14:** Cross section of allowable payload CG envelope.

## 3.5 Example Accommodation of Design Reference Mission

In this section, the DRMs from Chapter 2 are revisited to discuss their accommodation by the CUBE system. A system layout is presented, followed by details of mass, volume, CG, and Moments of Inertia (MOI) characteristics. Payload interface accommodations are also discussed. The successful accommodation of the three DRMs validates the design of CUBE and its ability to provide versatile payload support capabilities.

### 3.5.1 Gravity Wave Detection

The Gravity Wave Detection DRM has a payload made up of seven photometers. These photometers all need to be pointed in the nadir direction during the eclipse portion of the low Earth orbit to collect data. The 2U aperture area required by the payload is most easily accommodated by Config. C of CUBE. This layout is shown in Fig. 3.15. In this configuration, nadir would be down, and ram would be to the left. The solar arrays would be mounted to the top edge of M1 and would generate power with the payload held in the nadir direction throughout the orbit.

The mass of the payload is 1563.9 g, which is easily accommodated by the 4.25 kg payload limit of the CUBE. Its volume of  $2178.5 \text{ cm}^3$  fits within the 2U volume of the PM. The resulting CG and MOI are listed in Table 3.3. The CG is offset from the geometric center by 7.8 mm in the X axis, 2.2 mm in the Y axis, and

-9.5 mm in the Z axis. This is well within the allowable CG envelope and places the CubeSat CG very close to its geometric center. The MOI values are within the expected range and represent a resistance to rotation that is easily overcome by the ADCS actuators.

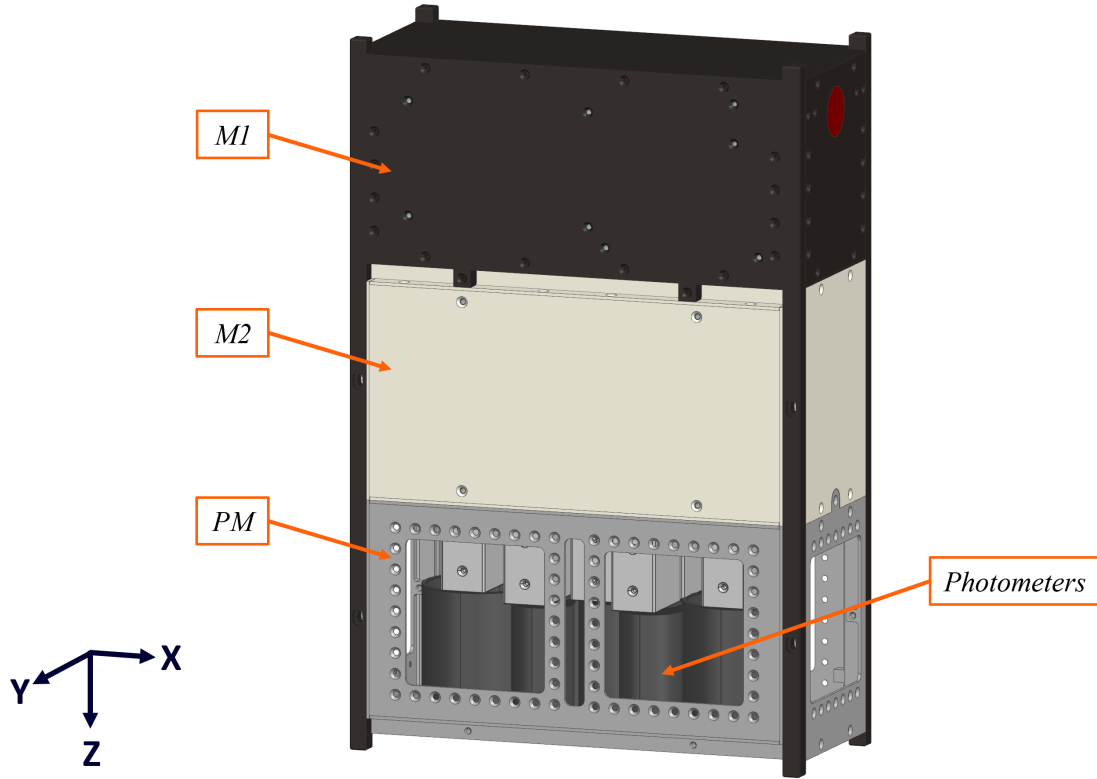


**Figure 3.15:** Photometer payload mounted in CUBE Config. C.

**Table 3.3: Gravity Wave Detection DRM mass properties.**

Center of Gravity (Absolute)		
X	120.95	mm
Y	52.23	mm
Z	153.72	mm
Moments of Inertia		
$I = \begin{bmatrix} 76537.53 & -138.66 & -5595.65 \\ \vdots & 97397.39 & 1088.718 \\ \dots & \dots & 31021.15 \end{bmatrix} \text{ kg mm}^2$		

The photometer payload and mission profile of the Gravity Wave Detection mission can be accommodated by CUBE without any mission specific modifications. At a peak power draw of 2.7 W, the payload is readily powered through the PLSB and MC. The 5.7 A current limit per connector pin allows the payload to be powered at any voltage level with only one pair of power pins. The data output of the payload does not exceed 21 Bps. This rate is easily accommodated by the I<sup>2</sup>C protocol, which can transfer up to 3.4 MBps in its high-speed mode [23]. The heat generated by the payload is relatively small due to its low power draw. As such, passive thermal control can be used to regulate payload temperature.

### 3.5.2 Sterile Neutrino Detection

The Sterile Neutrino Detection DRM payload consists of three main elements: the detector assembly, the instrument board box, and the cryocooler. Analysis performed in the preliminary design of the payload determined that it should be positioned with a 1U aperture in the ram direction (i.e., X axis forward) [13]. This could be accomplished with any of the three modular structure configurations. However, Config. B provides the best accommodation for this DRM. This layout creates a balanced system with the detector near the center of the structure. Most importantly, it provides an efficient geometry for active thermal control of the payload. The payload requirement of operating below 170 K is demanding in the small volume of a 6U CubeSat. The cryocooler is capable of extracting the necessary heat from the detector assembly. However, the heat must then be conducted away from the cryocooler and radiated to space in an efficient manner. Placing the cryocooler at the center of the structure allows for rapid heat dissipation with the addition of good thermal paths between the cryocooler and the structure. The instrument board box, which also produces a significant amount of heat when operating, is positioned behind the cryocooler to keep heat away from the detector assembly. In this structure configuration, the ram face is on the right side, allowing the star tracker to perform attitude determination while the payload is pointed at the galactic center. The layout of the payload within CUBE is shown in Fig. 3.16.

The combined mass of the detector assembly, instrument board box, and cryocooler is 2061.2 g. This is well within the payload mass limit. The payload volume of approximately 2000 cm<sup>3</sup> is less than the 2U volume available. The CG and MOI of the payload and bus are listed in Table 3.4. The CG is offset from the geometric center by 9.76 mm in the X axis, -0.29 mm in the Y axis, and -30.27 mm in the Z axis. This is within the allowable CG envelope. Only the Z offset is significant due to the high mass of the components in M1. The MOI values are similar to those calculated for the Gravity Wave Detection DRM. The product of inertia values are closer to zero indicating better alignment with the principal axes.

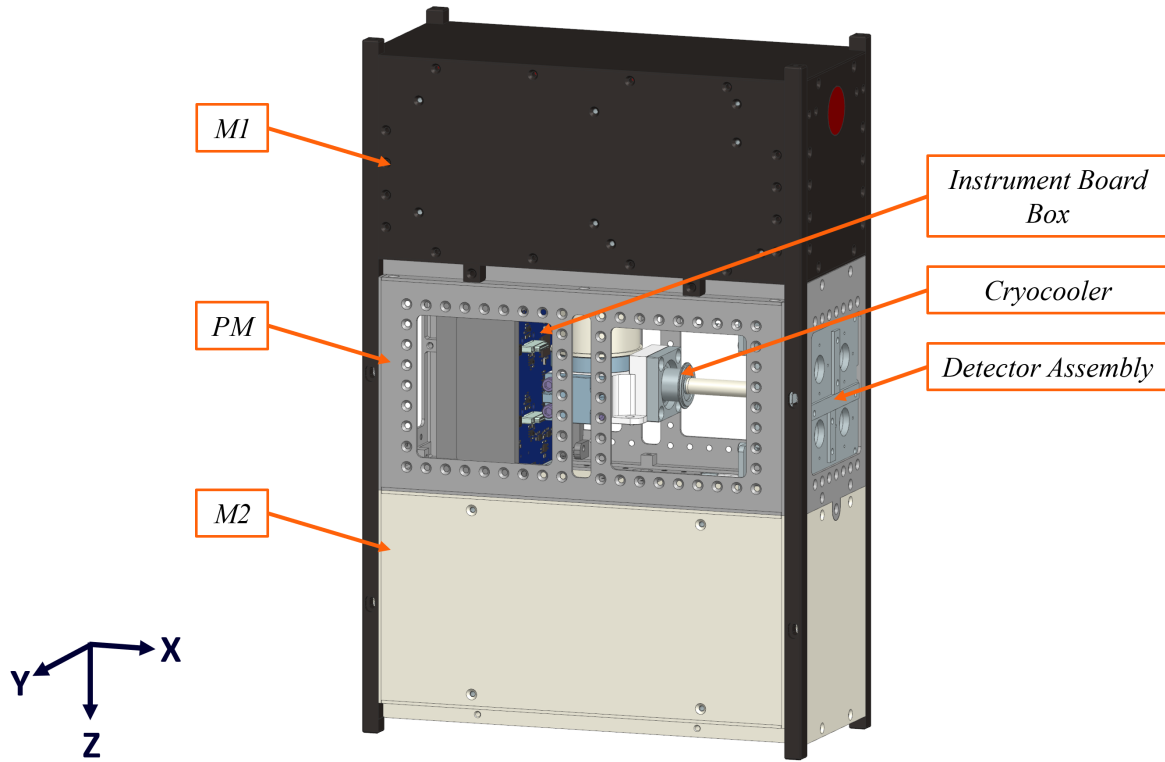


Figure 3.16: Sterile Neutrino Detector payload mounted in CUBE Config. B

Table 3.4: Sterile Neutrino Detection DRM mass properties.

Center of Gravity (Absolute)		
X	122.91	mm
Y	49.71	mm
Z	132.99	mm
Moments of Inertia		
$I = \begin{bmatrix} 61832.96 & -27.77 & -4719.47 \\ \vdots & 82258.93 & -16.04 \\ \dots & & 30436.02 \end{bmatrix} \text{ kg mm}^2$		

The MC and PLSB are capable of meeting the payload's requirements. When operating, the detector and cryocooler draw a combined 21.6 W. This power is needed at different voltages for the cryocooler, instrument computer, and sensors. As such, the 21.6 W is split between the 3.3 V, 5 V, and 12 V rails allowing for delivery under the 5.7 A limit of each pin in the MC.

The payload produces 32 MB of data once per orbit when collecting images. This amount of data can be accommodated by the PLSB through its I<sup>2</sup>C protocol, given the long downtime between image collection. The active thermal control and heat paths between the cryocooler and the structure are outside of the scope of this thesis. However, the design provides low thermal resistance interfaces between each module, enabling efficient passive thermal control and dissipation of heat to dark space. CUBE is well suited to accommodating the Sterile Neutrino Detection DRM. The payload's constraints on configuration and thermal control can be met without modifying CUBE.

### 3.5.3 Water Quality Monitoring

The Water Quality Monitoring DRM payload is a single large assembly including a hyperspectral sensor, optics, and an integrated processing board. The total length of the assembly is 176 mm, which limits the payload to being mounted along the 2U length of the PM. Since the hyperspectral imager is intended to collect water quality data frequently during its orbit, it is most efficient to have the imager pointing in the nadir direction by default. This can be accomplished by CUBE in Config. A. The payload is pointed in the opposite direction from the solar arrays, allowing for power generation throughout the sunlit portion of the orbit. Aperture covers could be added to the PM to protect the imager from debris during ground handling. This layout is shown in Fig. 3.17.

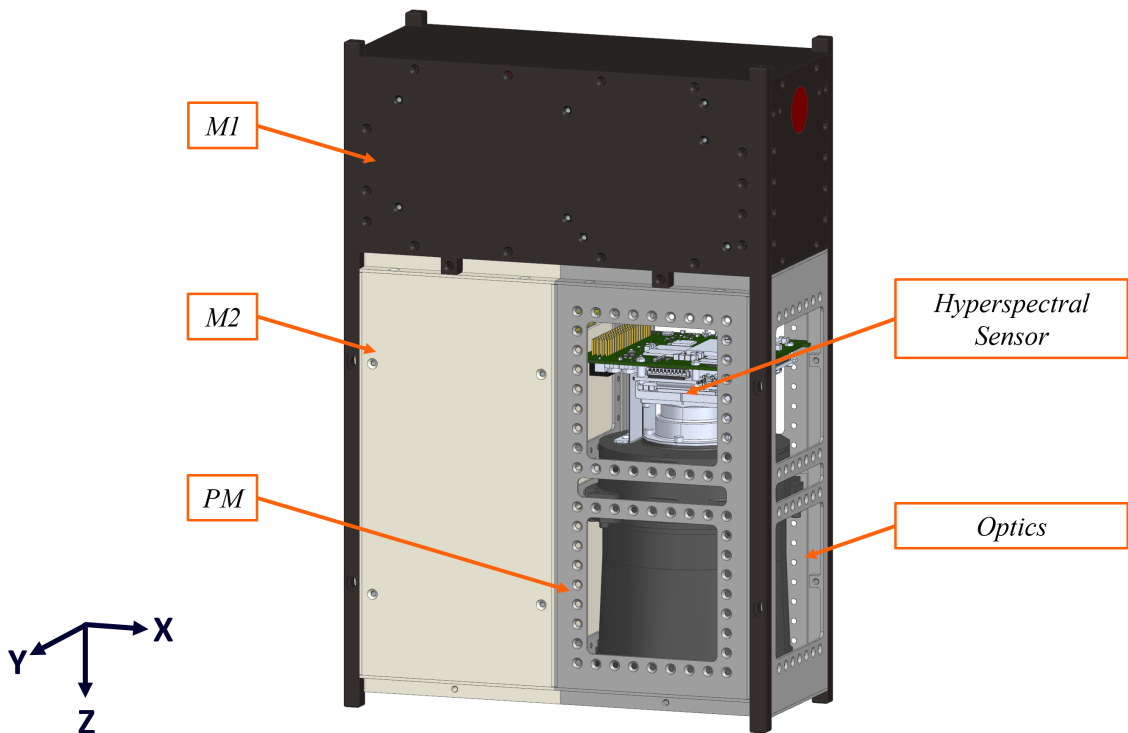


**Figure 3.17:** Hyperspectral Imager payload mounted in CUBE Config. A.

The mass of the hyperspectral imager is 1260 g. This is readily accommodated by the PM. Its volume, 1706 cm<sup>3</sup>, is also within the limits of the PM. The CG and MOI are listed in Table 3.5. The CG of the payload and bus is offset from the geometric center by 10.14 mm in the X axis, -0.05 mm in the Y axis, and -24.38 mm in the Z axis. This is both close to the geometric center, and well within the allowable CG envelope. The MOI are comparable to that of the other DRMs and within the control capabilities of the ADCS subsystem.

**Table 3.5: Water Quality Monitoring DRM mass properties.**

<b>Center of Gravity (Absolute)</b>		
X	123.29	mm
Y	49.95	mm
Z	138.87	mm
<b>Moments of Inertia</b>		
$I = \begin{bmatrix} 65409.75 & -29.14 & -1342.04 \\ \vdots & 87840.81 & -12.46 \\ \dots & & 32651.17 \end{bmatrix}$ kg mm <sup>2</sup>		

The MC and PLSB are capable of accommodating the hyperspectral imager payload requirements. The imager consumes 7.75 W while operating. This is supported by a single pair of conductors connected to the 5 V rail through the PLSB. With a connector limit of 5.7 A per pin, there is still a significant margin.

The data generation rate of the payload is more of a challenge. At 9.22 MBps, a single I<sup>2</sup>C interface would not be able to keep up. However, there are other options. The integrated processing board of the payload is capable of performing lossy or lossless compression following the CCSDS 122.0-B-2 standard [15]. Utilizing on-board compression would reduce the data rate that the MC needs to accommodate. It would also be possible to program the PLSB to accept data from the payload over two or more I<sup>2</sup>C interfaces using the pins already allocated to the PLSB in the MC. CUBE accommodates the hyperspectral imager payload and the mission profile of the Water Quality Monitoring DRM, even with the payload's demanding data and pointing requirements.

### 3.6 Prototype Structure

A prototype of CUBE was manufactured to verify the design. It is necessary to fill the structure with simulated subsystem hardware in order to accurately assess its performance. This was accomplished by grouping components that are mounted close together and emulating them with a metal block of identical mass and similar moments of inertia. The result is shown in Fig. 3.18. Secondary structures were then designed to position the CG of each block in the correct location. The internal layout on the left has each component color coded by subsystem. The internal layout on the right shows subsystem mass simulators in orange, payload mass simulators in blue, and secondary structure in gray.

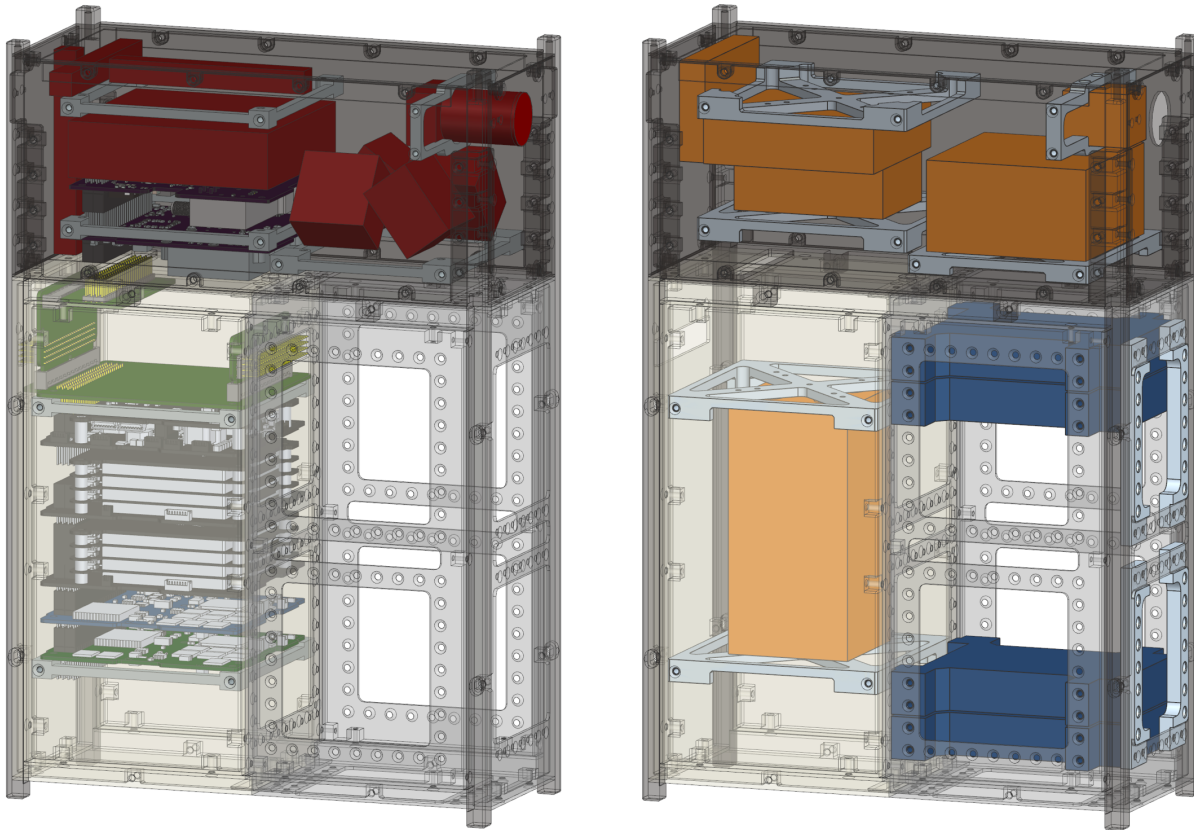


**Figure 3.18: Reduction of subsystem components (left) to mass simulators (right).**

In M2, the board stack of CDH and power hardware was easily reduced to a single aluminum block. The brackets supporting this block are slightly offset to achieve the same CG as the original board stack. In M1, the heavy reaction wheel pyramid was reduced to a block of steel. The board stack of the ADCS main board and radios was combined with the magnetorquers and replaced with three blocks of aluminum. The three-block design was chosen for its simplicity to machine and assemble. The star tracker is represented by a separate aluminum block due to its distance from the other components.

A single bracket design was used to mount the mass simulators in M1 and M2, except for the reaction wheel and star tracker simulators which required unique brackets. The PM contains a set of four identical payload plates that have a combined mass equal to the maximum payload mass. The payload plates can be mounted anywhere along the 2U axis of the module in increments of 10 mm using the mounting hole arrays in the structure. This allows the CG of the system to be adjusted for testing different configuration scenarios.

The module panels were milled from aluminum 6061-T6 stock. M1 and M2 were brushed to finish. The PM was polished. This is a cosmetic difference and was done to visually distinguish the three modules. The rails were Type III hard coat anodized to create a CubeSat Design Standard compliant interface for test fixtures and deployers. The prototype is shown in Fig. 3.19. Further details of the assembly and geometric dimensioning and tolerancing are covered in Chapter 5.

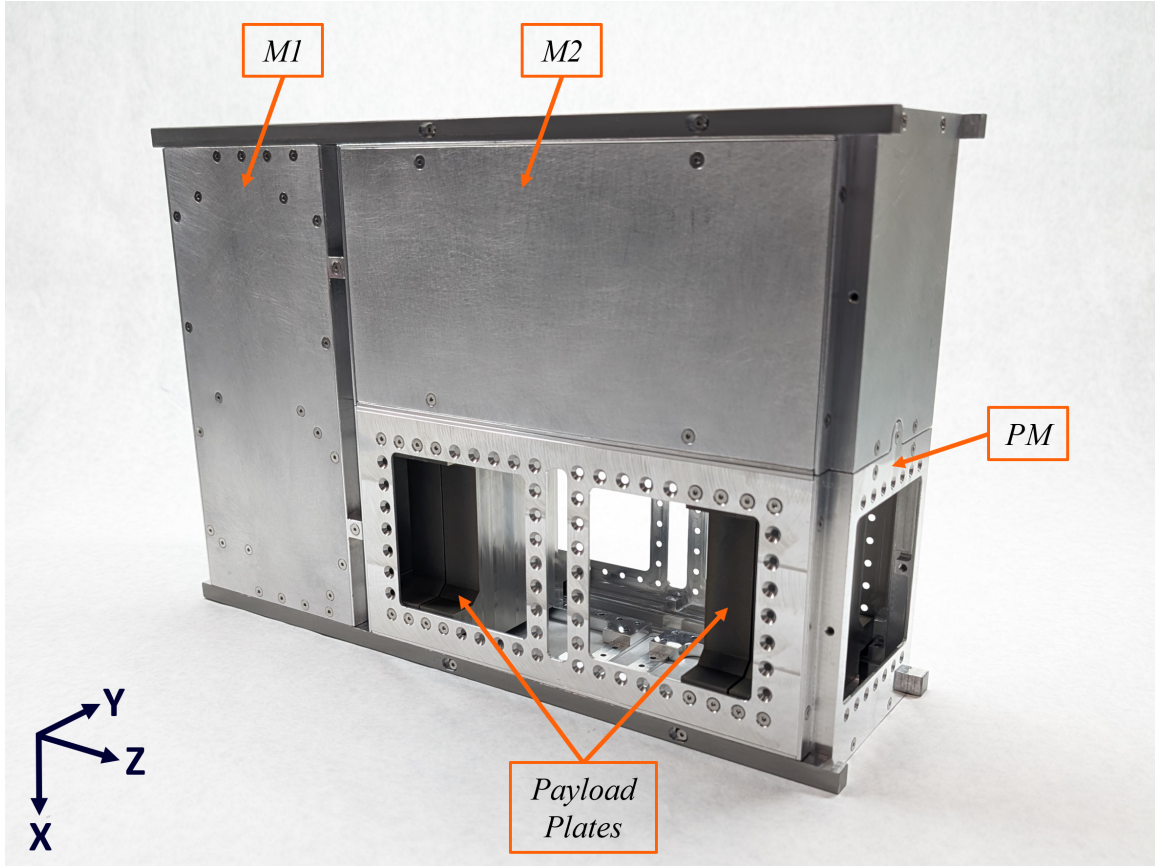


**Figure 3.19: Prototype of CUBE assembled in Config. A.**

Before the assembled prototype was verified by environmental tests, analysis was performed to predict the response of the structure. Results are presented in the following chapter.

# Chapter 4

## Structural Analysis

This chapter describes analysis that was performed on the CUBE design to simulate its behavior under simulated launch conditions. The approach to modeling CUBE for finite element analysis (FEA) is presented. The model was subjected to quasistatic launch loads in all axes and configurations to characterize its response. Free vibration simulations were also performed to establish a baseline for its normal modes in each configuration. All analysis presented in this chapter was performed using NASTRAN as the FEA solver and Siemens Simcenter 3D for pre and post processing. This analysis is used to ensure that the CUBE structure meets key launch provider requirements, allowing it to fly on a variety of launch vehicles.

### 4.1 Finite Element Model

A simplified CUBE Finite Element Model (FEM) was constructed to perform the FEA. This model discretizes each component into a mesh of nodes and elements. Nodes are points that are placed semiautomatically throughout the geometry of a component. Elements connect each node to its neighbors and come in many different shapes, including 1D, 2D, and 3D geometries. By applying bulk material properties to a mesh of nodes and elements, material behavior can be accurately simulated. This is accomplished by solving a set of large matrix equations associated with the mesh. The same FEM can be used for multiple simulations by changing the applied loads and constraints. The CUBE FEM used for both sustained acceleration and free vibration simulations is shown in Fig. 4.1.

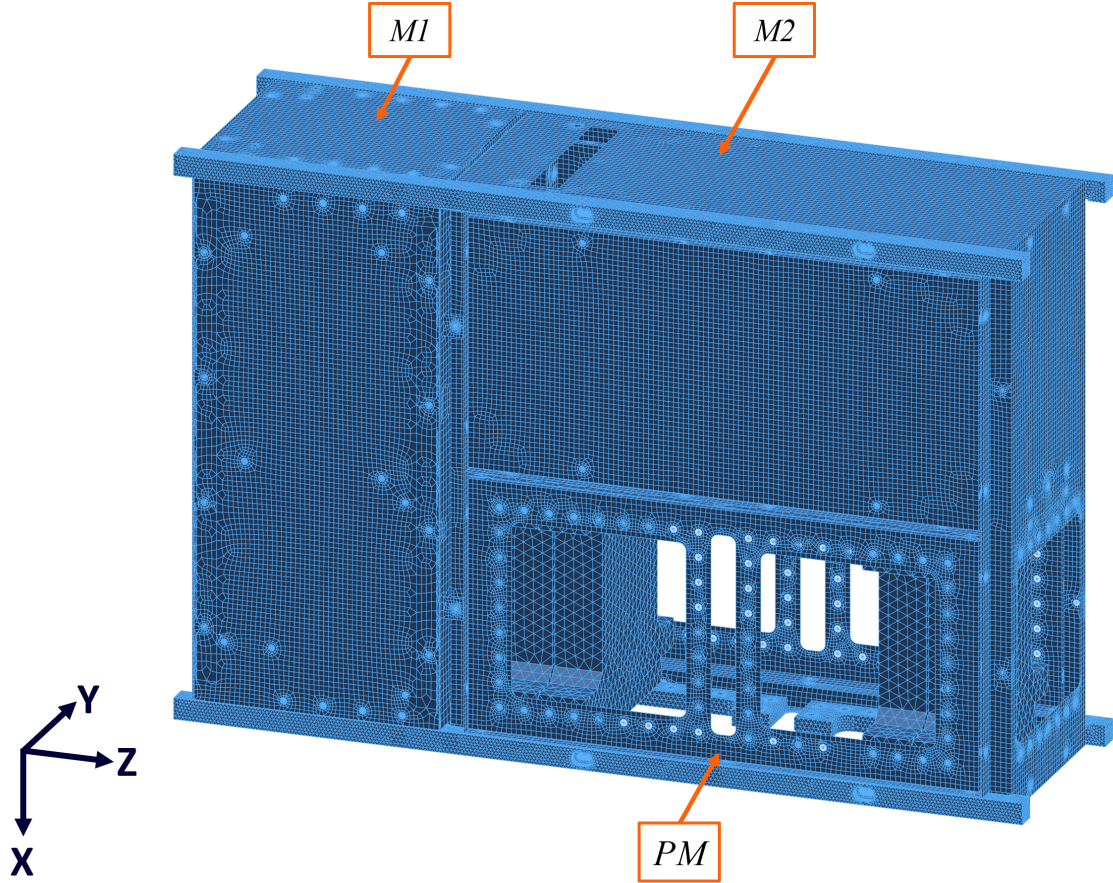


**Figure 4.1: Config. A CUBE FEM used for structural analysis.**

The complexity of a FEM directly determines the computational power required to run a simulation. FEM complexity is affected by the number of components to be modeled, the size of the elements in the mesh, and the shape of the elements. For CUBE, the number of components is fixed. The element sizes depend on the geometry of the part and whether it lies in a critical load path. Smaller element sizes are selected to provide additional resolution in areas of high stress concentration. This leaves element shape as a powerful tool for efficiently modeling CUBE.

Many of the structural components are thin flat plates with more complex geometry around the edges. Modeling such a component with 3D elements is very inefficient. A plate would have to be meshed with several 3D elements through its thickness to accurately calculate out-of-plane stresses. This requires an impractically small element size for thin plates. Instead, a thin plate can be represented by a plane of 2D elements. This dramatically reduces the mesh size, while enabling accurate results with proper definition of mesh associated data. An example of the simplifications made to the components is provided in Fig. 4.2. An unedited computer aided design (CAD) model of one of the end faces of M2 is shown on the left side of the image. This component consists of thin flat plates.

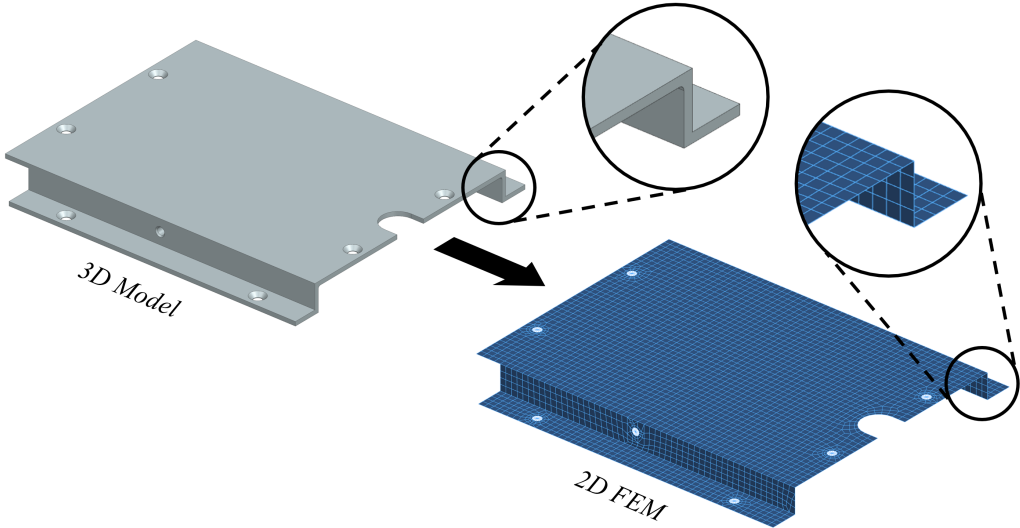


**Figure 4.2: Simplification of a 3D model of an M2 component to a 2D mesh FEM.**

However, it has right-angle corners, small fillets, and countersunk clearance holes. The FEM of the component, shown on the right, features several simplifications. The thin plates have all been meshed using 2D elements. These elements are stitched together at the right-angle corners. The small fillets and countersunk tapers have been eliminated in the simplification to 2D elements. Small features such as the fillets have no practical impact on the structural performance of the component for the purpose of simulation. The resulting FEM is relatively simple, while still capturing the important structural characteristics of the component. A similar set of simplifications was applied to all of the other thin plate components.

The rails are more complicated than the other structure components. They feature a nearly square profile for the majority of their length, with complicated geometry required to mount the panels of M1. There are also clearance holes for attaching the PM and M2, as well as a pocket at one end of the rail for mounting a power inhibit switch. These factors make the rails poorly suited to the use of 2D elements described for other components. Instead, the rails are modeled with a fine mesh of 3D tetrahedral elements. The FEM of a rail is shown in Fig. 4.3. The element size was selected to provide multiple elements through the thickness of the rail in all locations.

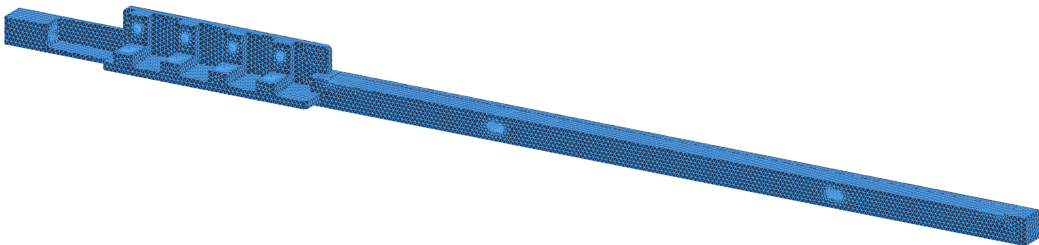


**Figure 4.3: 3D mesh FEM of a CUBE rail.**

The analysis is intended to verify CUBE's design integrity under flight conditions. As such, the FEM must include subsystem components and a payload to simulate realistic loading on the structure. Rather than use detailed CAD models for these components, mass models, introduced in Chapter 3 for the purpose of testing, were meshed into the simulation. There are two main reasons for taking this approach. First, the mass simulators and secondary structure are much easier to represent with nodes and elements, resulting in better simulation efficiency. Second, the mass simulators were designed to replicate the CG and MOI of the components that they represent, such that the load induced on the structure is very similar to the load created by the real components.

The layout of the mass simulators inside CUBE is the same as discussed in Chapter 3. The corresponding FEMs of the mass simulators and their secondary structure are shown in Fig. 4.4.

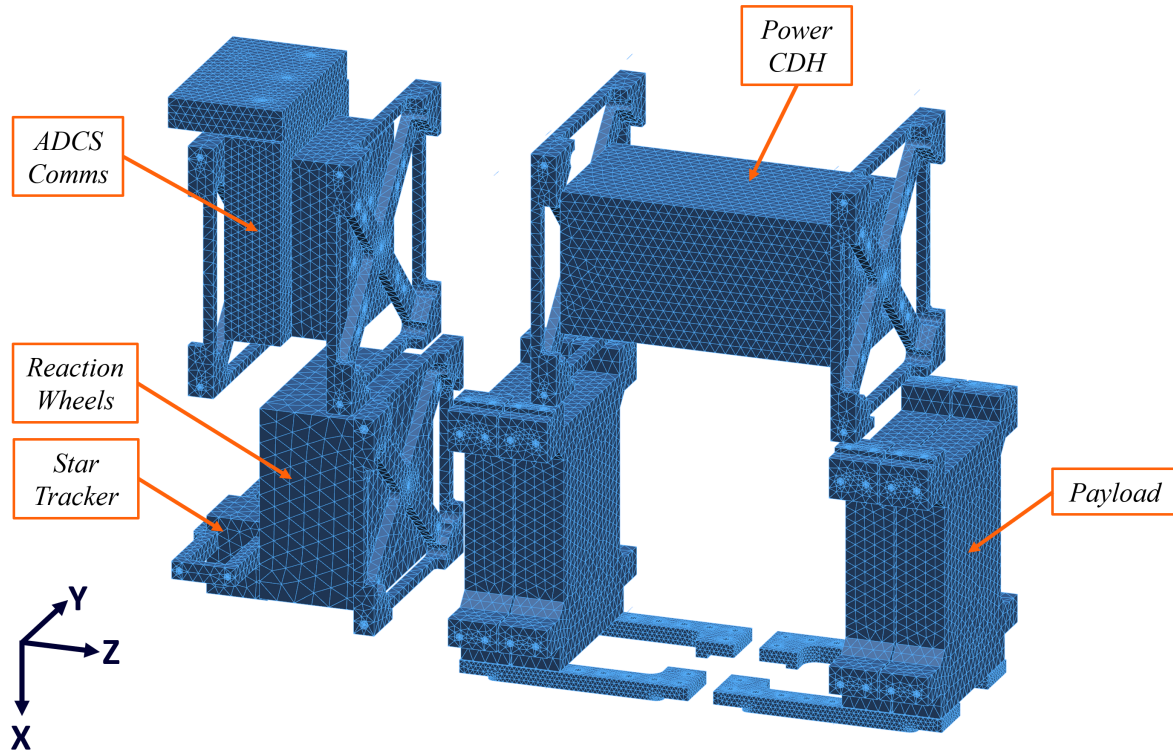


**Figure 4.4:** Mass simulator and secondary structure FEMs in their relative positions.

Each mass simulator is positioned to match the selected layout of subsystem components that balances mass distribution and MOI for the full CUBE system. The ADCS and Comms mass simulator is mounted to two brackets. These brackets are, in turn, mounted to two opposing side panels. The Power and CDH mass simulator is similarly mounted to two brackets. Having a bracket on either side of the mass simulator reduces the cantilever load applied to the panels. The reaction wheel mass simulator is only mounted to one bracket to be representative of the actual reaction wheel pyramid which only has attachment points on one face. The

small star tracker mass simulator is mounted to a single bracket that spans the distance between two side panels. The payload plates are positioned at opposite ends of the PM. This positioning was chosen to create the maximum possible MOI in Config. C, thereby maximizing the load on the structure. The mass simulators and secondary structure were all meshed with 3D tetrahedral elements due to their substantial thickness.

The structure is held together with more than a hundred fasteners. It is necessary to represent each fastened joint in the FEM to create an accurate model of CUBE. Meshing each fastener with 3D elements would be computationally expensive and inaccurate due to the small size of the fasteners. Instead, each fastener is meshed as a single, rigid 1D element. These elements are named RBE2 elements in NASTRAN. An RBE2 element creates a rigid connection between two nodes, where force is transmitted from one node to the other. This is a suitable approximation of the behavior of small fasteners when studying the overall behavior of a structure [24].

In order to model a screw head interaction with a countersunk clearance hole, a network of RBE2 elements can be created to connect a centrally located node to the 2D elements of the panel surrounding the hole. The same approach can be used to model the thread interaction. An example of a network of RBE2 elements connected between a central node and a 2D panel is shown in Fig. 4.5. Once each RBE2 network is created, the fastened joint can be formed by simply adding an RBE2 element between two corresponding central nodes.

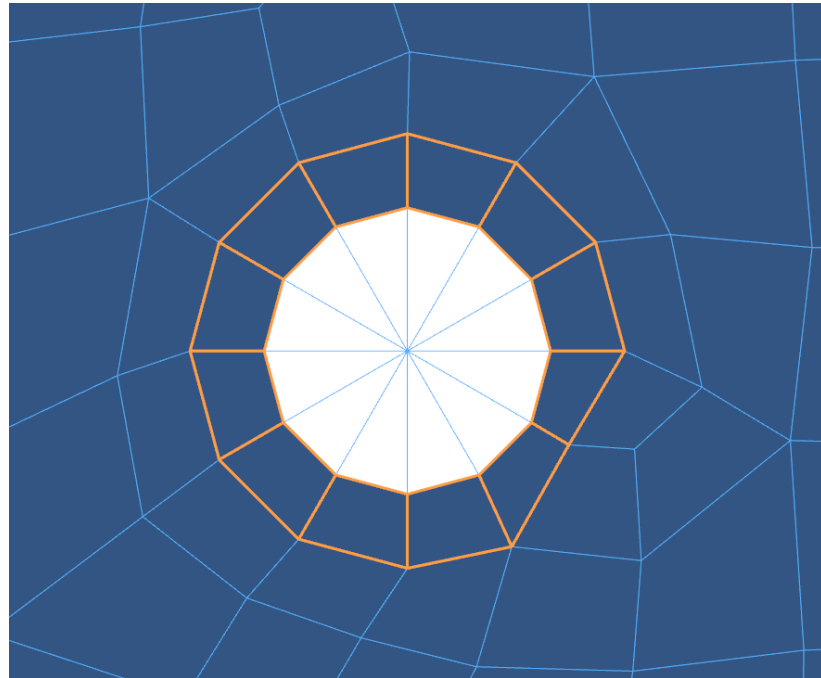


**Figure 4.5:** Network of RBE2 elements connecting a central node to the orange highlighted elements.

With all of the fastened joints modeled, the FEM is fully constrained. This means that no component is left floating and free to separate from the assembly. However, surface contact in a FEM is not modeled by default. Components are free to displace through each other in physically unrealistic ways. This results in inaccurate simulation results. To alleviate this issue, every region of surface-to-surface contact within the structure was defined in the FEM. Each region then undergoes additional force calculations to converge a resulting surface interaction for all simulations where the regions are included. The regions defined for CUBE are shown in Fig. 4.6. Each pair of regions that are in contact is illustrated by opposing gold arrows. The modeling of surface-to-surface contact significantly increases the computational expense of running a simulation. However, the increase in accuracy of results is well worth the reduction in efficiency.

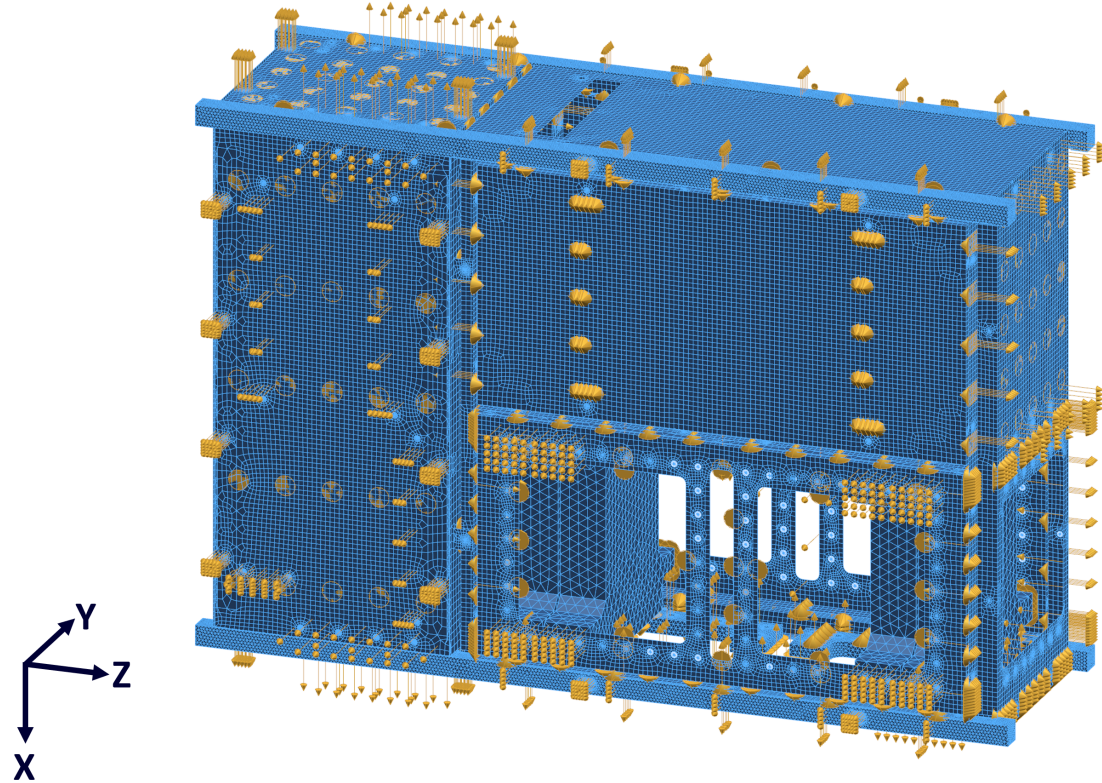


**Figure 4.6: FEM of CUBE with surface-to-surface interactions depicted by gold arrows.**

## 4.2 Sustained Acceleration

Sustained acceleration loading is used to assess the structure's performance when subjected to the quasistatic launch vehicle induced loads. Launch service providers publish payload user guides for their launch vehicles providing the nominal limit loads experienced during launch. Limit loads are then typically

translated into test or simulation requirements for prospective payloads. These requirements must be satisfied by testing before a payload is allowed to launch aboard the vehicle.

CUBE envelopes the requirements of multiple launch service providers. In the case of sustained acceleration, a set of payload user guides were reviewed, and the highest test load was selected for use in the simulations. The SpaceX Rideshare Payload User’s Guide requires testing at a sustained acceleration of 17g [25]. A qualification factor of 1.25 was then applied to reach an acceleration of 21.25g used for the sustained acceleration simulations. The qualification factor is used to build confidence in the design by proving a positive margin of performance. The acceleration was applied to the structure as a body force with separate simulations for each axis of loading. The structure was constrained in each simulation by applying fixed constraints to the rail faces opposing the direction of acceleration. This represents the interface between CUBE and a deployer that it is launched in. Models of all three configurations were tested to confirm the structural integrity of the design.

When performing analysis, it is critical to establish success criteria beforehand. In order to be considered successful, CUBE should not experience structural failure when the qualification test load is applied. Studying the simulated stress that develops in the structure is one way of determining whether failure is likely to occur. 6061-T6 is a ductile material, so as long as the maximum stress in CUBE does not meet or exceed the yield strength of 6061-T6, it is likely to survive the applied load. Accordingly, one measure of success is that the maximum stress does not exceed 75 % of the yield strength of 6061-T6.

It is also important that the structure remains sufficiently rigid under the applied load. Deformations in the structure that do not have a permanent adverse effect on mission objectives are acceptable. The ductile nature of the material used allows CUBE to undergo some deformation without failing. Any deformation that occurs in the elastic regime of the material, below the yield strength, is non-permanent. However, deformation can negatively affect the alignment of sensitive payloads. For the purpose of this analysis, a maximum displacement of less than 0.1 mm was considered acceptable. A displacement of 0.1 mm along one of the rails is within the tolerance of commercial deployers due to the need for free sliding deployment of CubeSats rather than a tight friction fit. A 0.1 mm change in ADCS component alignment would be inconsequential as it is within the mounting precision achievable with standard fasteners and tight clearance holes. Determining the possible effects on all sensitive payloads is challenging. However, a 0.1 mm displacement orthogonal to the Z axis would result in an angular misalignment of 61.2 arcseconds across the length of the entire structure. This is less than the demanding pointing accuracy requirement of the Water Quality Monitoring DRM.

The plots of displacement and Von-Mises stress for each configuration and load axis are shown on the following pages. The plots are annotated with the maximum displacement and stress observed and the respective locations where they occurred. An arrow with a dashed line pointing to a location indicates that

the maximum magnitude is not on the outer face. All plots have the constrained rail faces marked with triangles. A brief description of the results is provided with each set of plots.

Fig. 4.7 shows the first simulation case for Config. A (which has the payload adjacent to and under the bus modules) with the acceleration load applied in the positive X axis. As expected, the displacement is zero on the bottom faces of the rail where the fixed constraint is applied to the FEM. Larger displacements, in the range of 0.016 mm, are observed on the top panels of M1 and M2. The maximum displacement for this case is 0.0478 mm, occurring on the mass simulators inside M1. This meets the displacement success criteria.

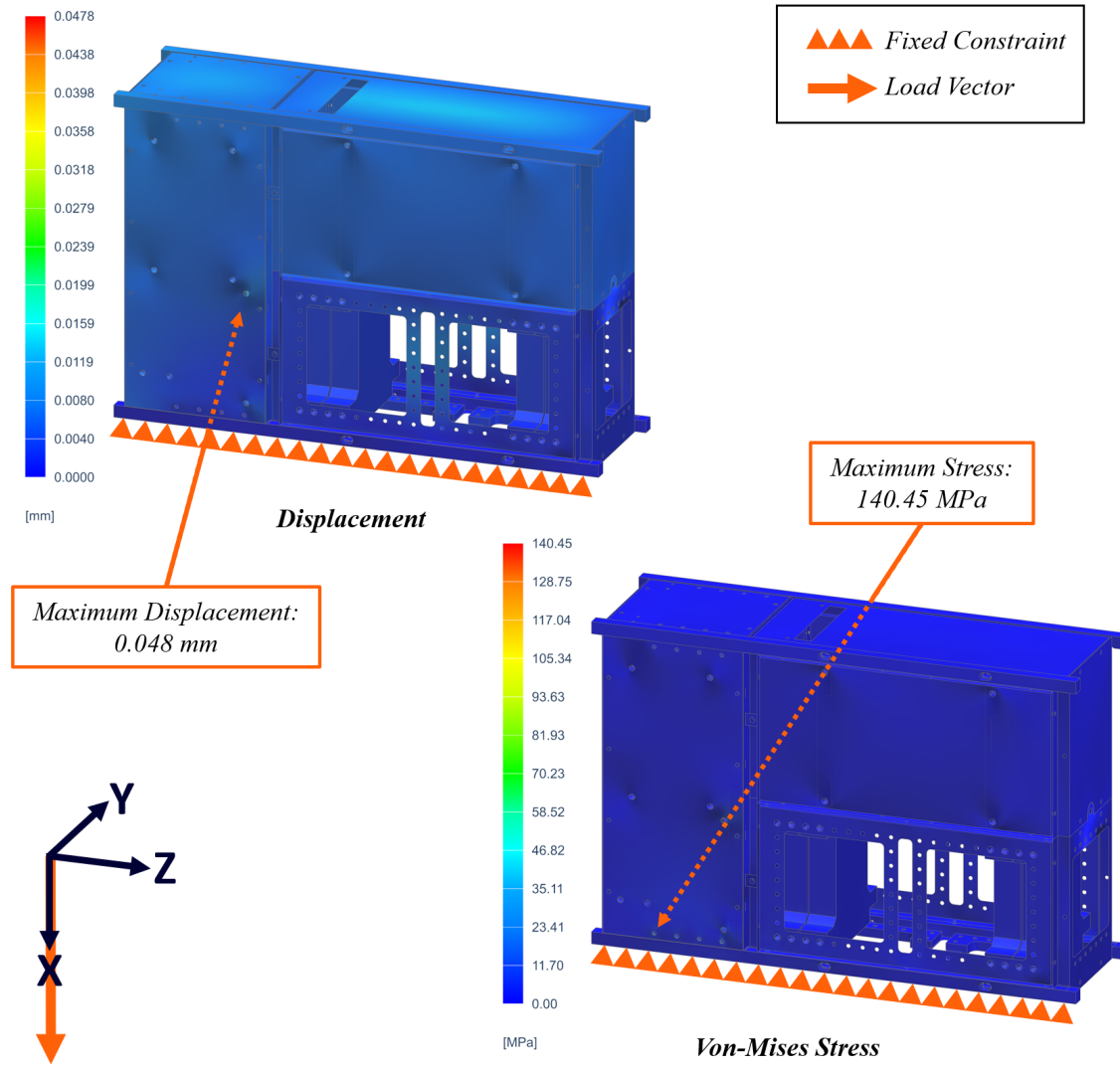


**Figure 4.7: Simulated loading of Config. A subjected to 21.25g in the X axis.**

The stress plot shows very low Von-Mises stress in the panels. This is because stress is concentrated at the fastener locations. FEMs can produce nonphysical stress concentrations at the interface of RBE2 elements transmitting a point load to a circular hole in a panel. In reality, this load is distributed over the conical

head of a countersunk screw and through multiple screw threads engaged in the hole that it is installed in. The first circle of elements around each fastener hole have been excluded from these results, allowing the simulated stress to be distributed more evenly to produce more realistic stress concentrations. In this case, the maximum stress of 140.45 MPa occurs at one of the rail fastener locations on the backside of M1. The yield strength of aluminum 6061-T6 is 276 MPa, which puts this maximum stress at only 50 % of the yield strength. CUBE therefore passes both success criteria in this simulation case.

Fig. 4.8 shows the simulation case for Config. A with the acceleration load applied in the positive Y axis. Under this loading condition, the structure is compressed towards its constrained rail faces on the backside of the plot. The displacement plot shows relative displacements in the middle of the M1 and M2 side faces. However, the magnitude of these displacements does not exceed 0.06 mm. The stress plot once again shows little stress in the large panels.

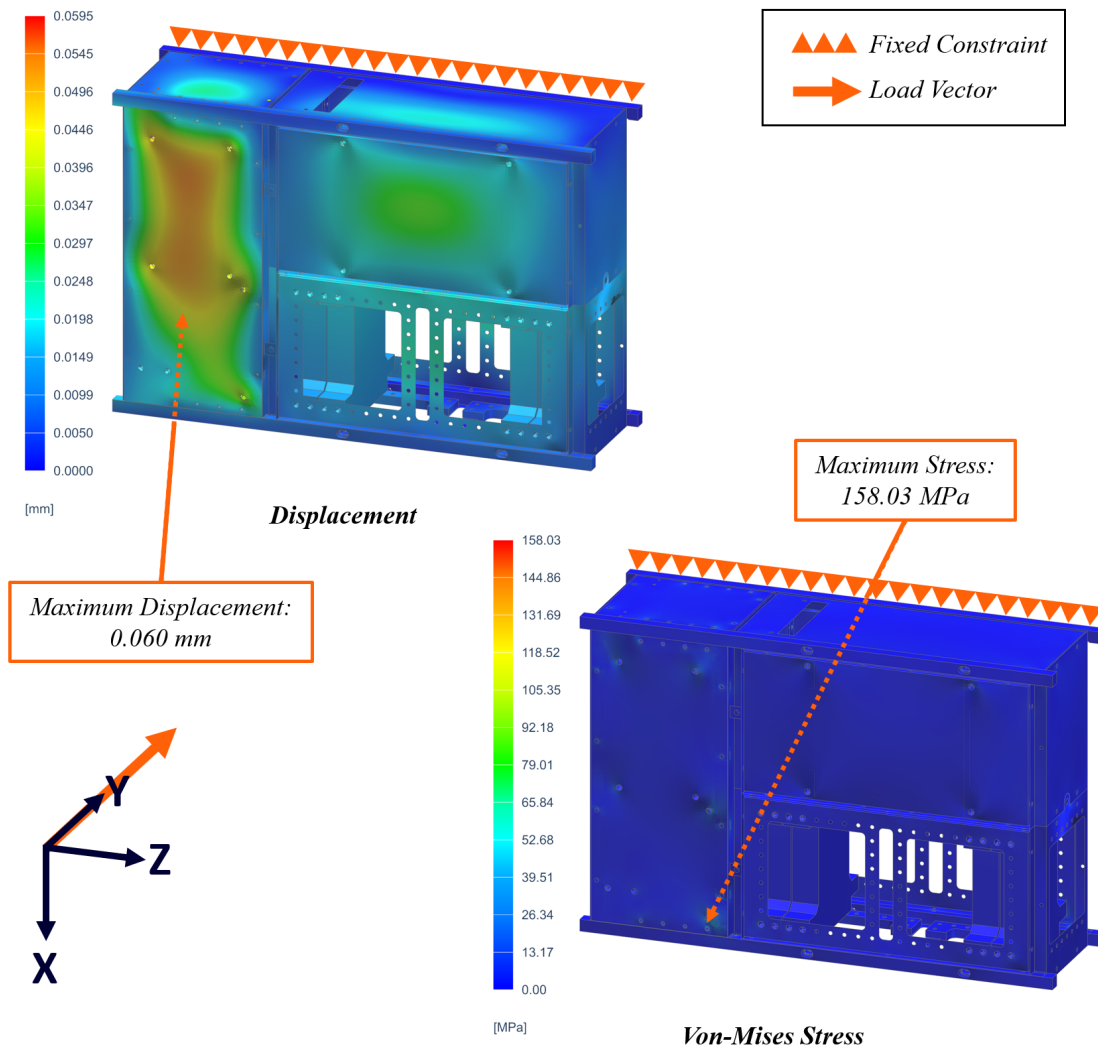


**Figure 4.8:** Simulated loading of Config. A subjected to 21.25g in the Y axis.

Stress concentrations are observed as expected near fastener locations. The cantilever load created by the reaction wheel mass simulator in this load direction results in a noticeable stress concentration around its secondary structure fastener locations. The maximum stress occurs near one of the rail fastener locations on the backside of the structure. With the specified rail constraints, these fasteners must support the weight of M1 and its internal components. The maximum stress of 158.03 MPa is still less than 58 % of the material yield strength. CUBE satisfies both success criteria in this simulation case.

Fig. 4.9 shows the simulation case for Config. A with the acceleration load applied in the Z axis. In this case, the rail ends on the right side of the structure are fixed. Moving along the rails to the left, displacement increases, and an approximately uniform displacement of 0.03 mm is observed throughout M1 and M2. The PM exhibits higher displacement than the other modules due to the high-mass payload plates mounted inside. The largest displacement occurs in the PM near the PM-M2 interface.

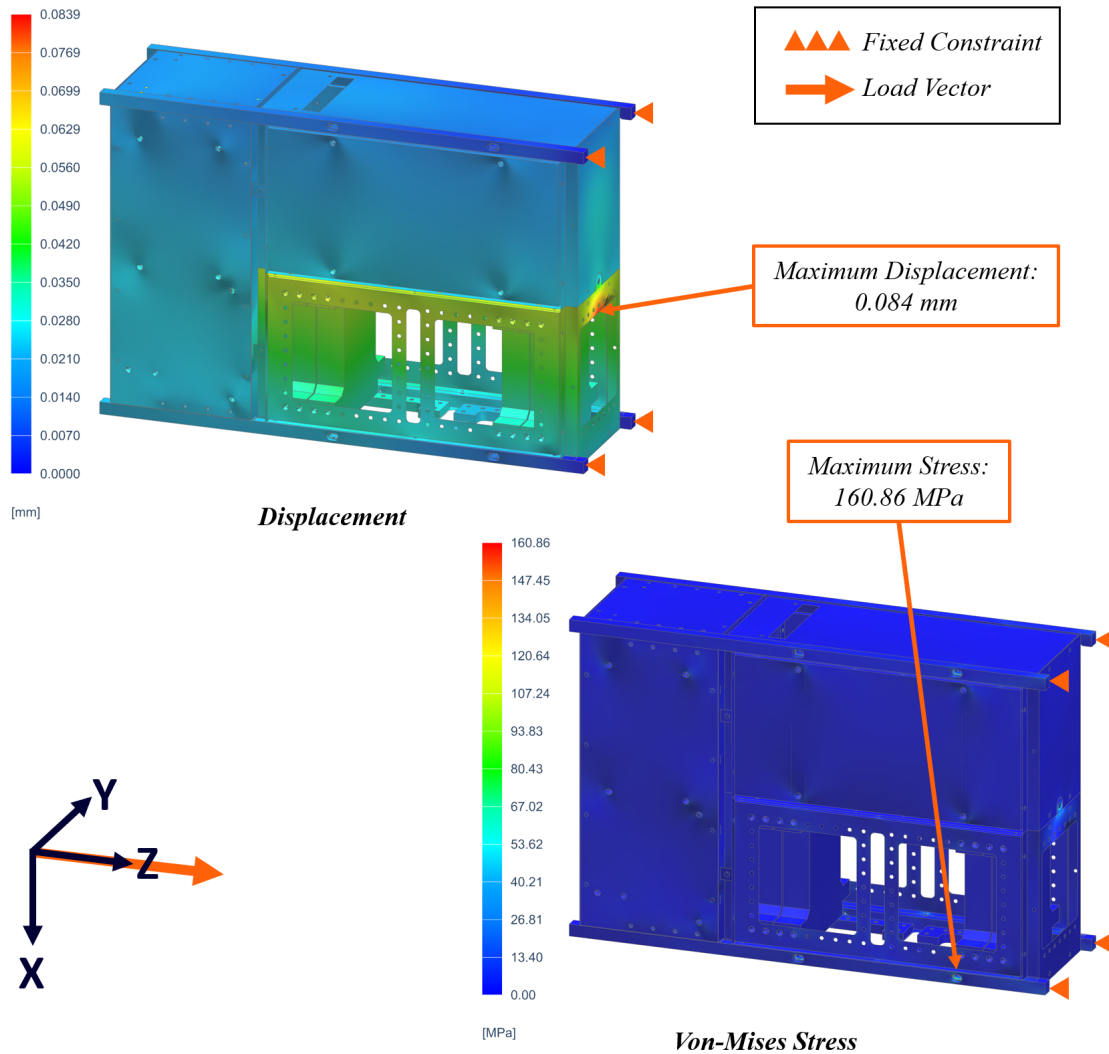


Figure 4.9: Simulated loading of Config. A subjected to 21.25g in the Z axis.

The maximum displacement magnitude of 0.084 mm is still adequately small. The stress plot reveals significant stress concentrations near the fastener holes in the rails used for mounting the PM and M2. The maximum stress of 160.86 MPa occurs around the fastener through the rail into the PM closest to the fixed end of the rails. This is likely caused by the comparatively weaker interface between the PM and M2. The larger displacements at the top of the PM indicate that the module is being primarily supported by M1 and the two rails that it is attached to. The maximum stress is only 58 % of the yield strength of the rail. This leaves a significant performance margin. CUBE satisfies both success criteria in this simulation case.

Fig. 4.10 shows the simulation case for Config. B (which stacks the payload modules vertically between the two other modules) with the acceleration load applied in the X axis. The displacement plot reveals inconsequential panel deformation, while the largest displacements occur inside CUBE.

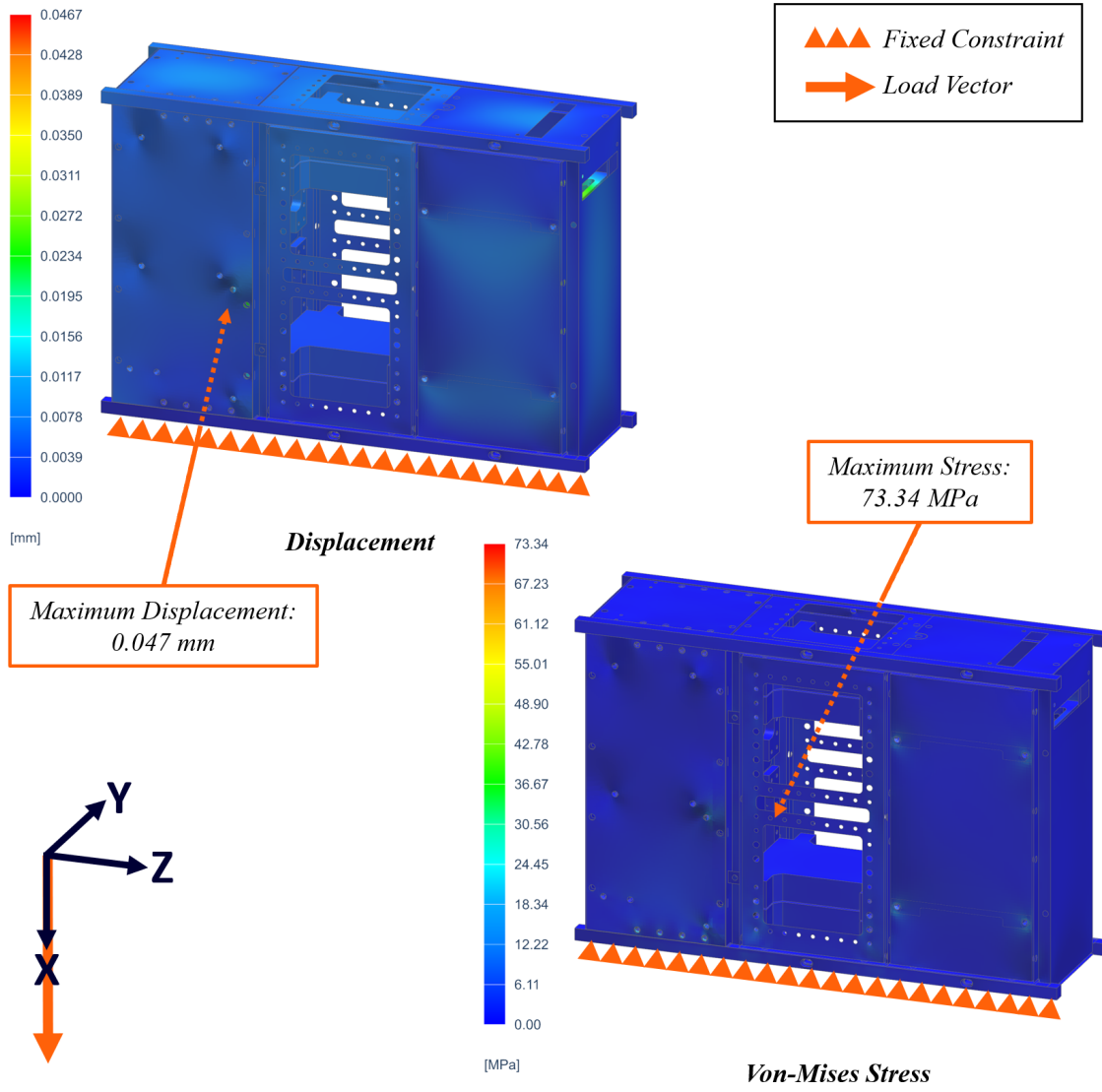


Figure 4.10: Simulated loading of Config. B subjected to 21.25g in the X axis.

The maximum displacement is only 0.047 mm, which is well within the displacement success criteria. Since payload alignment is of particular interest, it is worth noting that the change in distance between the upper and lower payload plates in the PM is less than 0.01 mm in this simulation case. The stress plot shows stress concentrations around the panel fasteners. However, the scale of stress magnitudes observed is much lower in this simulation case than the others discussed so far. The maximum stress is 73.34 MPa. It is located at a fastener hole in the secondary structure that holds the reaction wheel mass simulator. This stress is less than one third of the yield strength. CUBE satisfies both success criteria in this simulation case.

Fig. 4.11 shows the simulation case for Config. B with the acceleration load applied in the Y axis. At 0.060 mm, the maximum displacement under this load is very similar to the corresponding simulation case with the Config. A structure.

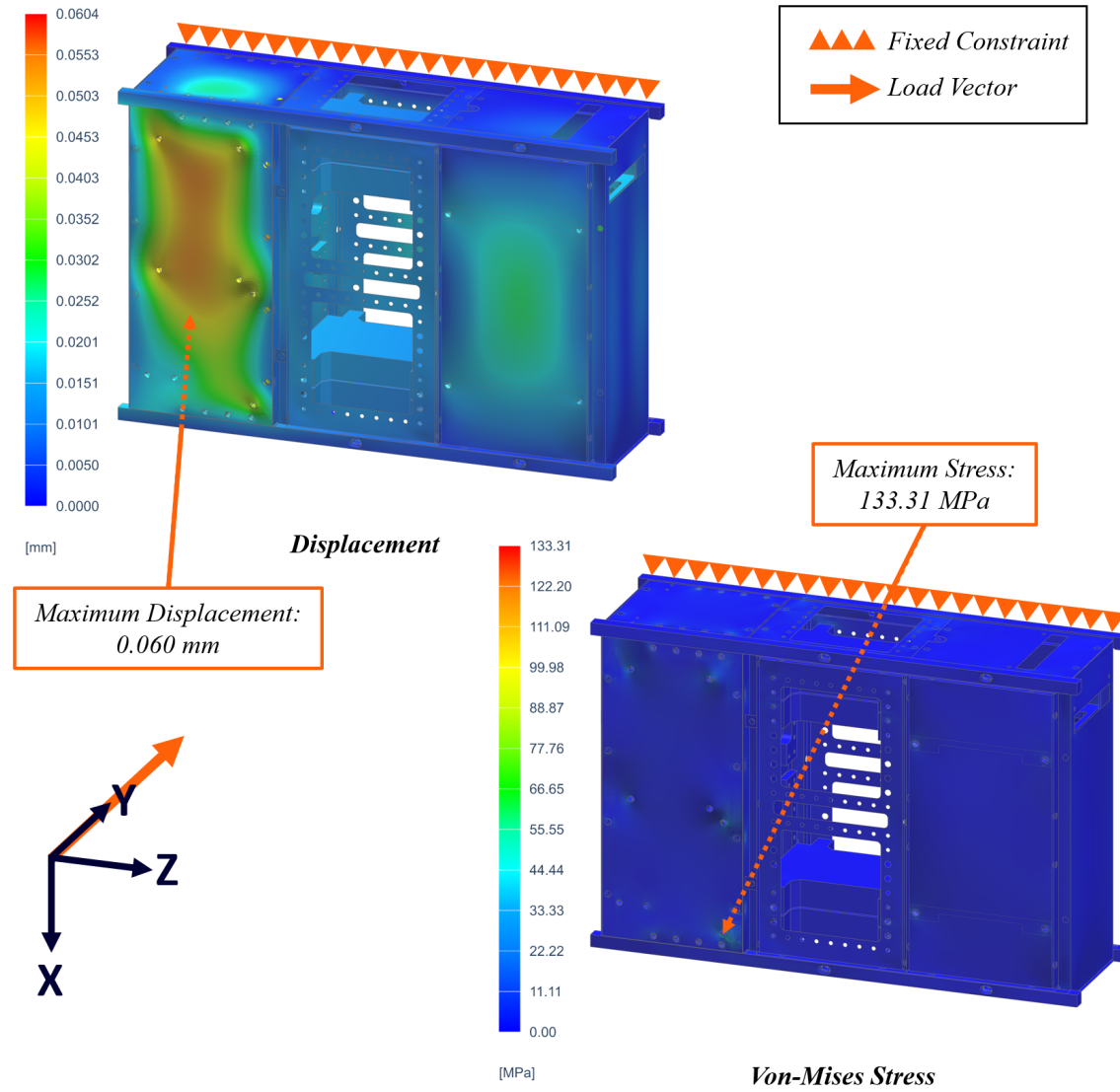


Figure 4.11: Simulated loading of Config. B subjected to 21.25g in the Y axis.

However, the displacement of the PM is lower in Config. B due to the support of M1 and M2 on either side. There is relatively low stress throughout the model. The maximum stress is 133.31 MPa. It is located near one of the rail fasteners in M1 on the backside of the structure in the stress plot. The maximum stress is less than half of the yield strength and is not of concern. CUBE satisfies both success criteria in this simulation case.

Fig. 4.12 shows the simulation case for Config. B with the acceleration load applied in the Z axis. This load direction forces the structure to be supported by the small surface area of the rail ends. This generally leads to more uniform, and slightly larger, displacements throughout the structure. The displacement plot shows that the PM is better supported in this configuration. The displacement of the payload plates is less than 0.03 mm. The maximum displacement meets the success criteria at only 0.065 mm.

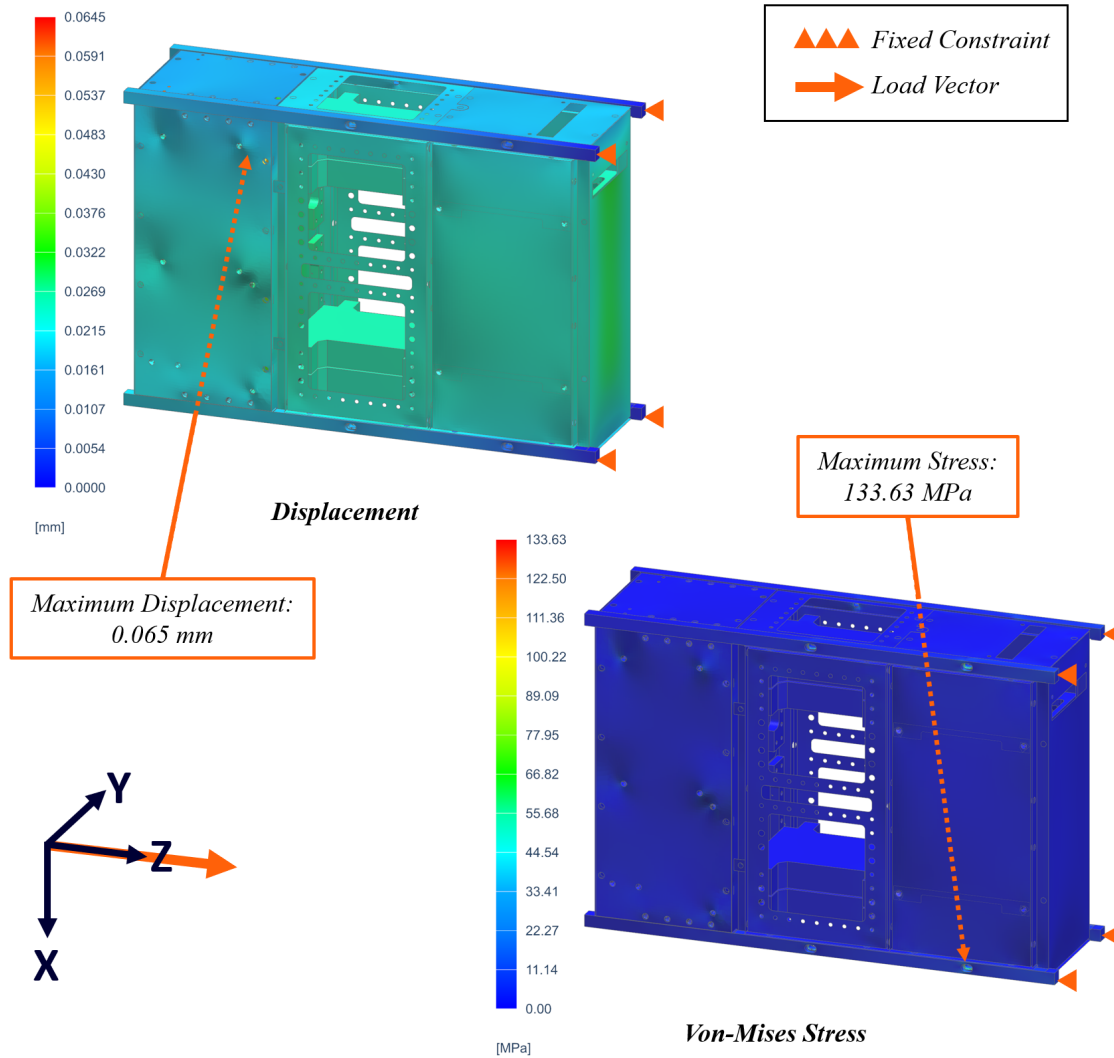


Figure 4.12: Simulated loading of Config. B subjected to 21.25g in the Z axis.

The stress plot once again shows the maximum stress located at a rail fastener closest to the constrained end, as it was in the Config. A simulation case. This is primarily the result of M2 “hanging” from the four rail fasteners closest to the constrained end, where the rails show very little displacement. The maximum stress magnitude of 133.63 MPa is less than half of the material yield strength. CUBE satisfies both success criteria in this simulation case.

Fig. 4.13 shows the simulation case for Config. C (which places the payload module at the end of the bus stack) with the acceleration load applied in the X axis. The performance of the structure in this simulation case is nearly identical to that of Config. B. The maximum displacement is 0.047 mm, and the displacement gradient is similar, with higher displacements near secondary structure fastening locations and further away from the constrained faces of the rails.

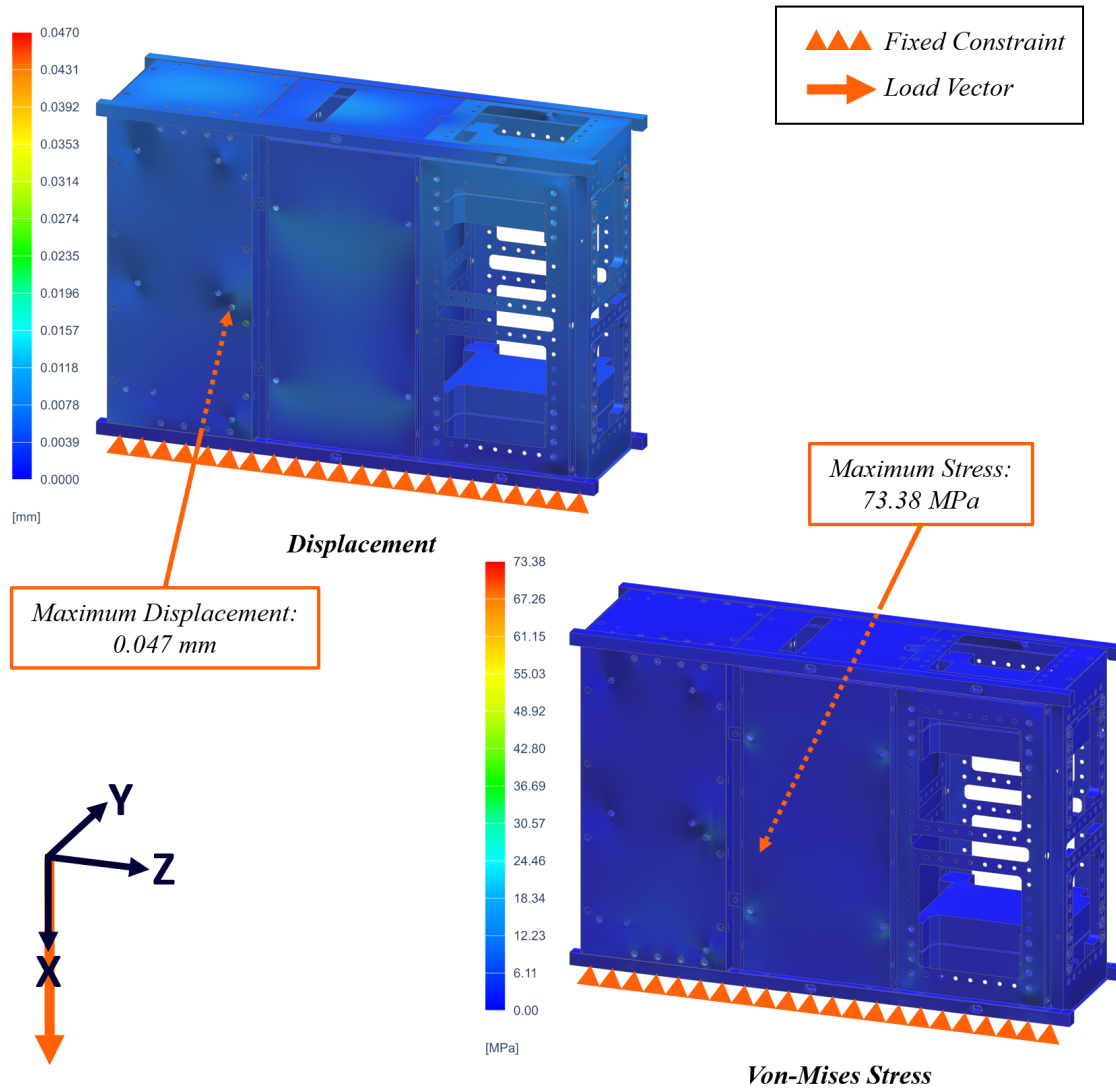


Figure 4.13: Simulated loading of Config. C subjected to 21.25g in the X axis.

The maximum stress of 73.38 MPa is once again located near a fastener that holds the reaction wheel mass simulator in place. The magnitude of the stress is not concerning at less than one third of the yield strength. CUBE satisfies both success criteria in this simulation case.

Fig. 4.14 shows the simulation case for Config. C with the acceleration load applied in the Y axis. This simulation case has nearly identical displacement results as Config. B, with the load applied in the same axis. There is significant displacement visible in the side panel of M1 caused by the mass simulators that it supports inside the module. The maximum displacement of 0.058 mm is well within the range permitted by the success criteria. The maximum stress occurs in the same region near the rail fasteners in M1 on the backside of the structure. The magnitude of 128.56 MPa is acceptable at less than half of the material yield strength. CUBE satisfies both success criteria in this simulation case.

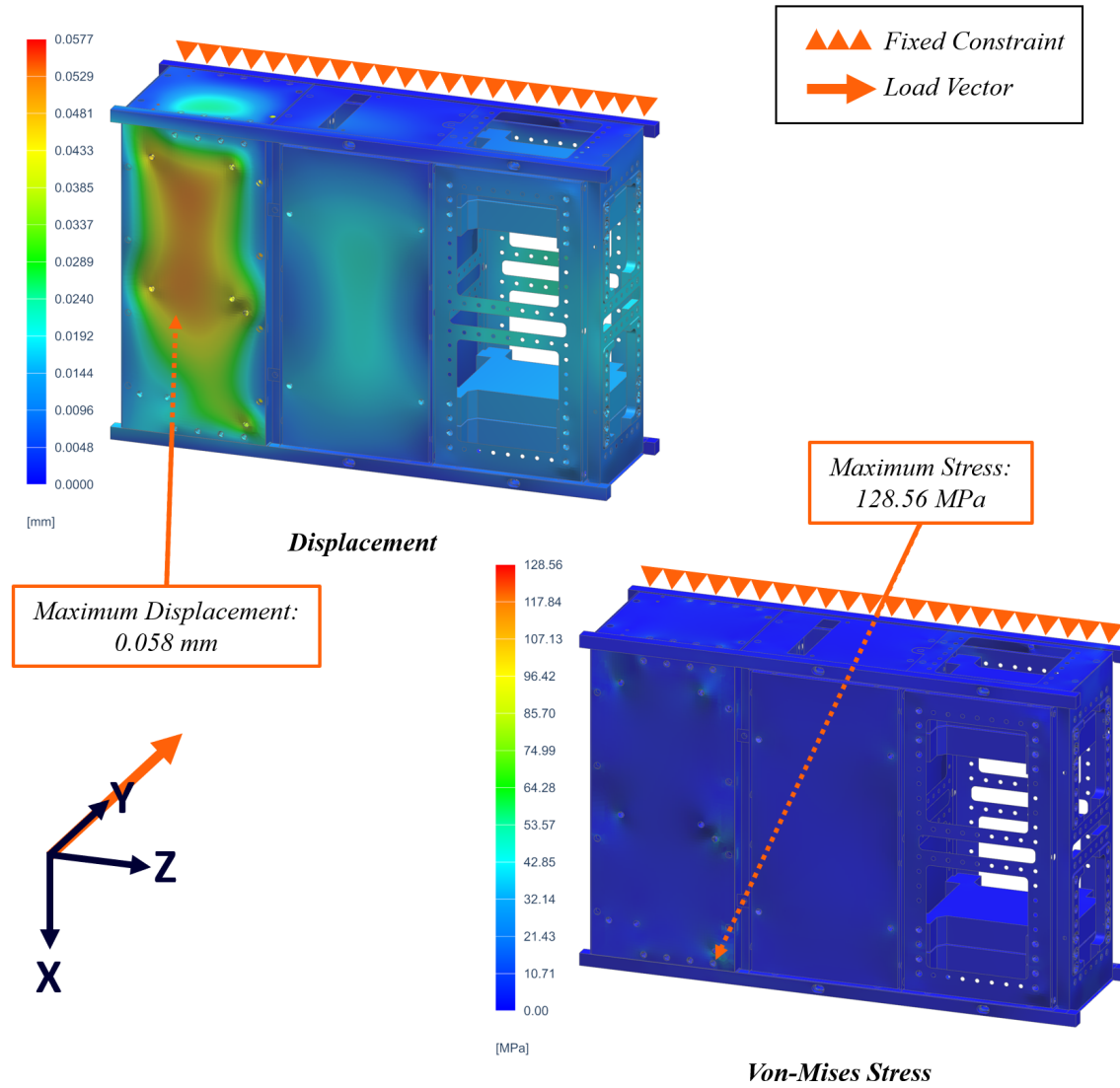


Figure 4.14: Simulated loading of Config. C subjected to 21.25g in the Y axis.

Fig. 4.15 shows the simulation case for Config. C with the acceleration load applied in the Z axis. The displacement plot reveals larger displacements in the PM in this configuration than in Config. B. Displacements on the order of 0.035 mm are seen throughout the PM with the largest displacements occurring at the interface between the PM and M2. The largest displacement in this simulation case is 0.064 mm, which is well within the bound of the displacement success criteria. The maximum stress occurs in a rail near one of the fasteners that supports the PM. This is the same location as the corresponding simulation for Config. B. However, the magnitude of the stress is higher than the Config. B case. Since the PM and M2 swap locations between Config. B and Config. C, this is likely due to the mass of the PM and payload plates being higher than the mass of M2. At 146.84 MPa, the magnitude of the maximum stress is well below the yield strength of the material. CUBE satisfies both success criteria in this simulation case.

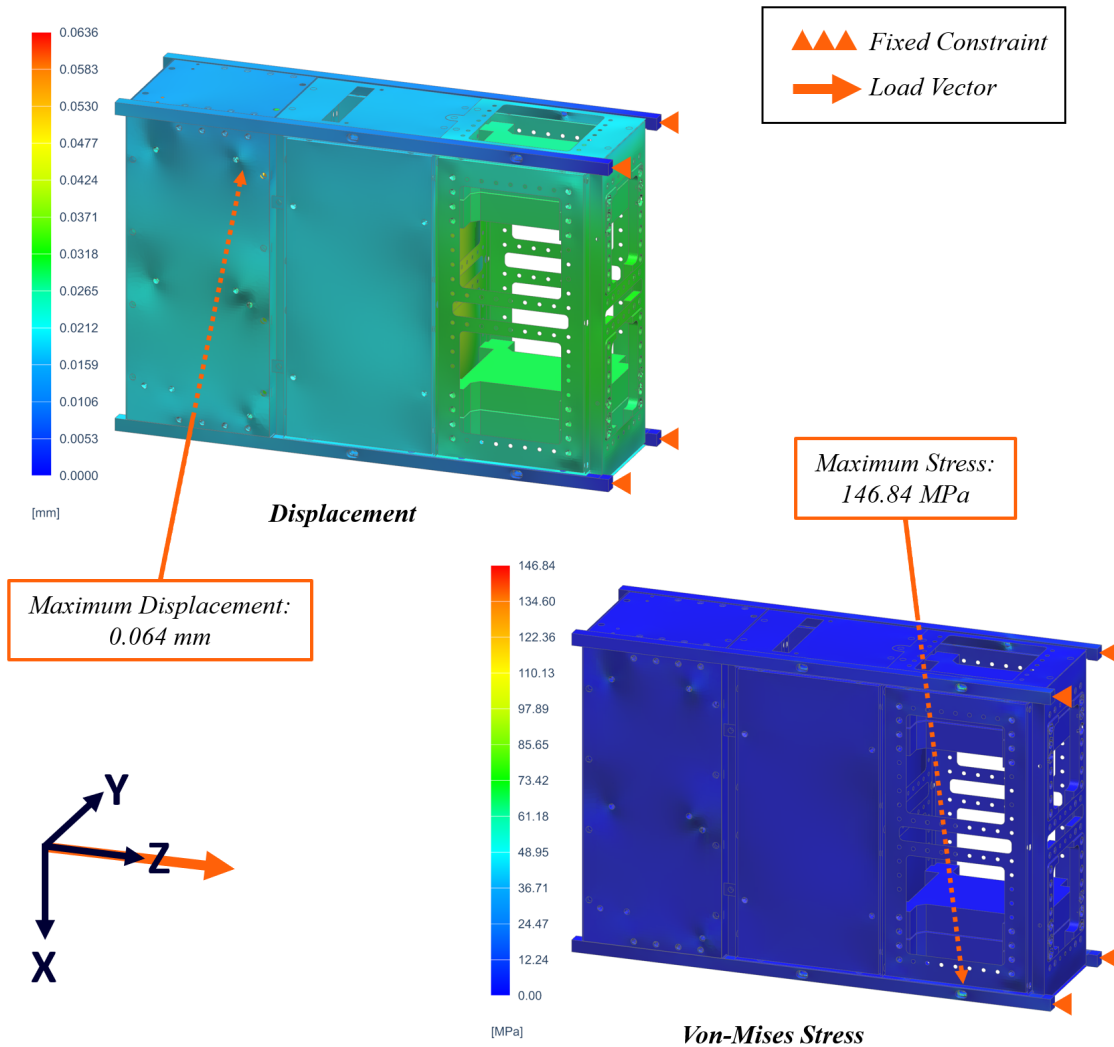


Figure 4.15: Simulated loading of Config. C subjected to 21.25g in the Z axis.

The results of the sustained acceleration simulations clearly show that the design is sufficiently strong to withstand the quasistatic launch loads that it will experience. The maximum displacement across all CUBE configurations and load axes is only 0.084 mm, when subjected to 21.25g of acceleration. Payloads mounted inside the PM are unlikely to experience detrimental changes in alignment with these limited displacements. The maximum stress across all of the simulation cases is only 58 % of the yield strength of aluminum 6061-T6. This provides substantial margin in the strength of the structure, leading to high confidence that CUBE can survive quasistatic launch loads without experiencing material failure in any structure component. It also indicates that some mass could be removed from the structure without compromising its strength in these load conditions.

Comparing the performance of CUBE in the different simulation cases yields insight into the weaker parts of the design. The simulations performed on Config. A reveal that the interface between the PM and M2 is a potential weak point. Additional fasteners could be added to strengthen this interface. The simulations where the load was applied in the Y axis show somewhat large displacements in the side panels of M1 and M2. Loading in the Y axis exposes the largest faces of each module to internal loads from the mass simulators. Geometry could be added to the inside of the panels to stiffen them in this loading direction. However, this would come at the cost of additional mass. The simulations where the acceleration load was applied in the Z axis, show that the rails are subjected to significant stress when supporting the modules that are attached to the fasteners through the rails. The CubeSat Design Standard and deployer requirements limit the amount of rail surface area that can be recessed [2]. This limits the number of fasteners that can be designed into the rails.

In conclusion, CUBE's design meets the success criteria as specified. The substantial margin in the strength of the structure suggests that there may be room for further optimization of the design. Such optimization would incur complexity and cost penalties. The resulting mass efficiency improvement would likely not be very beneficial to payload flexibility since volume is a tighter constraint than mass for all but the highest density payloads. However, improvements in mass efficiency could be used to provide more subsystem capability. It is also worth noting that the 42 % margin found between the maximum stress and the yield strength only applies to the quasistatic load case. Any further optimization would need to maintain the stiffness of the structure to withstand the vibrational loads of launch.

### 4.3 Normal Modes

The launch environment created by any launch vehicle consists primarily of vibration at a wide range of frequencies and amplitudes. It is necessary to assess CUBE's performance when subjected to vibrational

loading in order to qualify the design for flight. The objective is to ensure that serious coupling does not occur between the launch vehicle and CUBE. The majority of high energy vibrations produced by a launch vehicle occur at relatively low frequencies. For this reason, launch providers typically require the first normal mode, or fundamental frequency, of a payload to be above 50 Hz [26]. While specific launch environments vary, the 50 Hz cutoff reduces the likelihood of coupling between the launch vehicle and CUBE. Modes occurring at higher frequencies typically have less energy and mass participation, making them less of a concern for mission success. Ultimately, testing is an essential method for verifying a design's response to vibrational loading. Analysis performed prior to testing is very valuable for assessing performance and establishing baseline estimates of normal mode frequencies.

The FEM was subjected to free vibration in order to calculate its normal modes in each configuration. Free vibration refers to modal analysis that does not use any external forces or constraints. Under these conditions, the first six modes that are calculated are rigid body modes, where the entire assembly is displaced. Such rigid body modes should occur at frequencies very close to zero. If the frequency of these modes is higher, it can indicate issues with the internal constraints of the FEM under simulation. The remaining modes that are calculated are elastic modes where the assembly is deformed.

NASTRAN has a variety of different analysis types, or solution sequences, that simulate different physical effects. The modal analysis falls within NASTRAN's SOL 103 solution sequence. SOL 103 calculates the normal modes of a mesh by finding the eigenvalues and eigenvectors of a governing equation that contains the mesh properties. There are other types of vibrational analysis supported by NASTRAN that allow for modeling of more complex nonlinear dynamics. SOL 103 was selected for this analysis to provide a worst-case estimate of the first normal mode frequency. The addition of rail constraints imposed by a deployer limits the motion of the structure and thereby increases the frequency of its first normal mode. Simulating free vibration provides a baseline frequency without the effects of stiffening provided by external constraints. The success criterion for this analysis is that CUBE only have normal modes that occur above 50 Hz.

The FEA simulation was set up to calculate the six rigid body modes and the first six normal modes in each configuration. Mass simulators, secondary structure and surface-to-surface interactions were all included to improve the accuracy of the results. Table 4.1 lists the frequency associated with each mode number for the three CUBE configurations.

**Table 4.1:** First six normal modes of CUBE in each configuration.

Mode #	Config. A Modes [Hz]	Primary Participation	Config. B Modes [Hz]	Primary Participation	Config. C Modes [Hz]	Primary Participation
1-6	$< 1.2 \times 10^{-3}$	<i>N/A</i>	$< 1.1 \times 10^{-3}$	<i>N/A</i>	$< 1.1 \times 10^{-3}$	<i>N/A</i>
7	167.75	<i>Structure</i>	171.11	<i>Structure</i>	162.53	<i>Structure</i>
8	277.32	<i>Structure</i>	304.28	<i>Both</i>	307.10	<i>RW Sim</i>
9	298.47	<i>RW Sim</i>	305.94	<i>RW Sim</i>	318.48	<i>Struct + Sim</i>
10	324.48	<i>Struct + Sim</i>	333.12	<i>RW Sim</i>	329.67	<i>RW Sim</i>
11	324.98	<i>RW Sim</i>	341.90	<i>Struct + Sim</i>	347.86	<i>ADCS Sim</i>
12	331.59	<i>ADCS Sim</i>	350.42	<i>ADCS Sim</i>	376.70	<i>Structure</i>

A column to the right of each set of frequencies in the table indicates mode shape by detailing the main component(s) that participate in each mode. Each configuration has its first six modes at very low frequencies on the order of  $10^{-3}$  Hz. This is the desired result expected for rigid body modes associated with a properly prepared FEM. The first normal mode occurs at 167.75 Hz for Config. A, 171.11 Hz for Config. B, and 162.53 Hz for Config. C. This satisfies the success criterion of the modal analysis.

The first normal mode in each configuration is primarily formed by participation of the entire structure. These normal mode shapes include displacement of the rails. This indicates that the mode may not occur when CUBE is constrained inside a deployer. That would result in the first normal modes occurring at even higher frequencies.

Config. A experiences its second normal mode at 277.32 Hz. This is another normal mode that is primarily excited in the structure. It does not appear in the other two configurations, leading to the conclusion that Config. A is somewhat less rigid than the other configurations. This is likely due to the mounting orientation of the PM and M2. Config A. relies on the stiffness of the rails more than the other two configurations because the space between the rails in the X axis is not spanned by single structure components.

The next mode that occurs in all three configurations is excited near 300 Hz as a result of reaction wheel mass simulator motion. These normal modes, and the other modes involving mass simulators, could be partially damped by redesigning the secondary structure that holds the mass simulators. There are several normal modes in the range of 300 Hz to 400 Hz that involve a combination of structure and mass simulator motion. These modes are unlikely to be excited with significant energy by a launch vehicle due to their relatively high frequencies.

Performance varies only slightly between the three configurations. Config. B and Config. C exhibit very similar behavior, while Config. A exhibits a response at somewhat lower frequencies. CUBE is sufficiently stiff in all three configurations and provides excellent margin above the first normal mode cutoff of 50 Hz. The successful completion of the analysis detailed in this chapter was sufficient to proceed to the manufacturing of a physical prototype. The prototype is discussed in detail in the following chapter, and its performance under real loads is presented.

# Chapter 5

## Qualification Testing

This chapter describes the environmental test campaign that was performed on the CUBE prototype. Following manufacturing of the structure and representative component mass simulators, a test fit assembly was performed to ensure proper integration and assess the assembly procedure. Modifications and lessons learned during this test are presented. Once successfully assembled in all three configurations, a thermal vacuum (TVAC) test was conducted to verify the performance of CUBE in space-like environmental conditions. Temperature profiles for this test are presented along with the results of a post-test torque check on every fastener. Vibration tests were also performed on an electrodynamic shaker table. CUBE was configured to have the highest possible MOI to maximize internal loads, and then it was subjected to random vibration in all three axes. The random vibration tests establish the ability of CUBE to survive launch. The test campaign provided confidence in the design's structural integrity, opening the door to future flight opportunities.

### 5.1 Test Fit Assembly

The test fit assembly performed on the prototype was a critical step in qualifying the design. It provided insight into its manufacturability, highlighted the need for some minor design modifications, and ultimately verified the three different configurations. The test began with an inspection of each structural component, shown in Fig. 5.1. During this inspection, the dimensions of each component were compared against those in the engineering drawings used for manufacturing. No deviations outside the ISO 2768 Class F tolerances specified in the drawings were found. The finish of the components was also inspected for defects. The hard anodization of the rails was acceptable, and the remaining uncoated components showed no performance altering flaws. All of the threaded components were fitted with helical inserts to improve the durability of the threads. These inserts were all checked for proper installation and functionality.

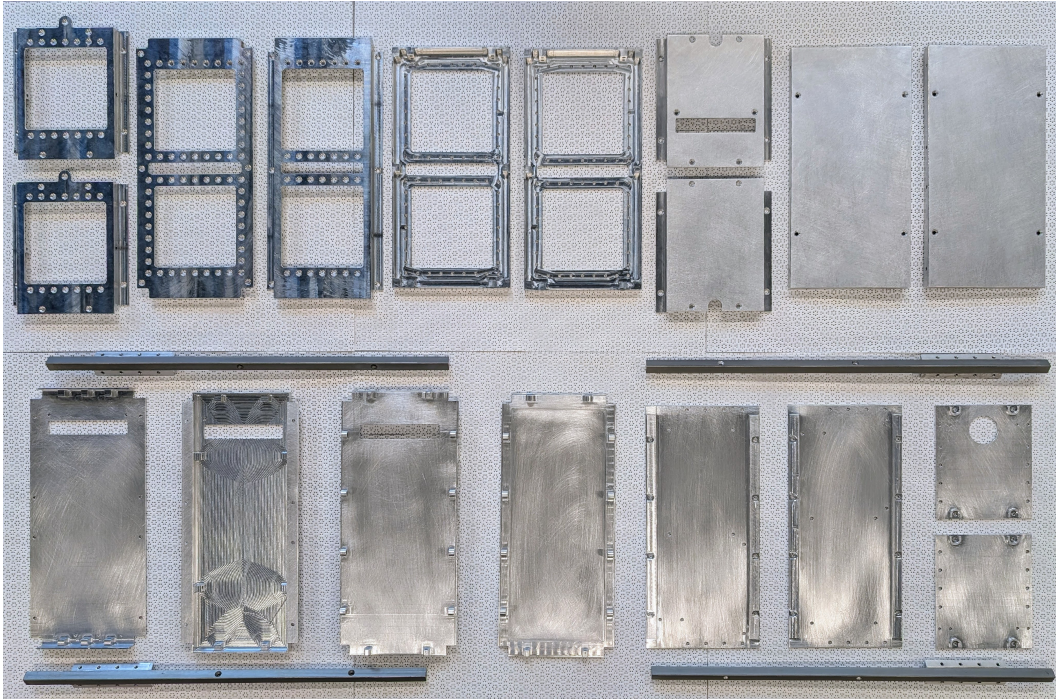


**Figure 5.1: Main structure components of the prototype prior to assembly.**

The M1, M2, and PM modules were each assembled following the inspection of their components. This assembly was performed with dry fasteners and a low torque value to check component integration without introducing unnecessary wear. The assembly of each module was successful, and no issues with dimensional compatibility were found. The completion of module assembly verified the design and assembly procedures at the subassembly level. The assembled modules are shown in Fig. 5.2.

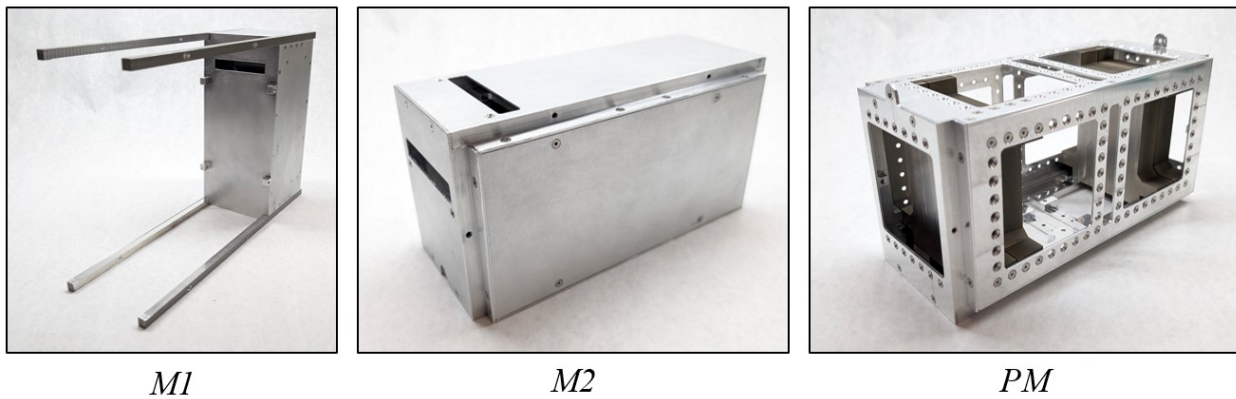
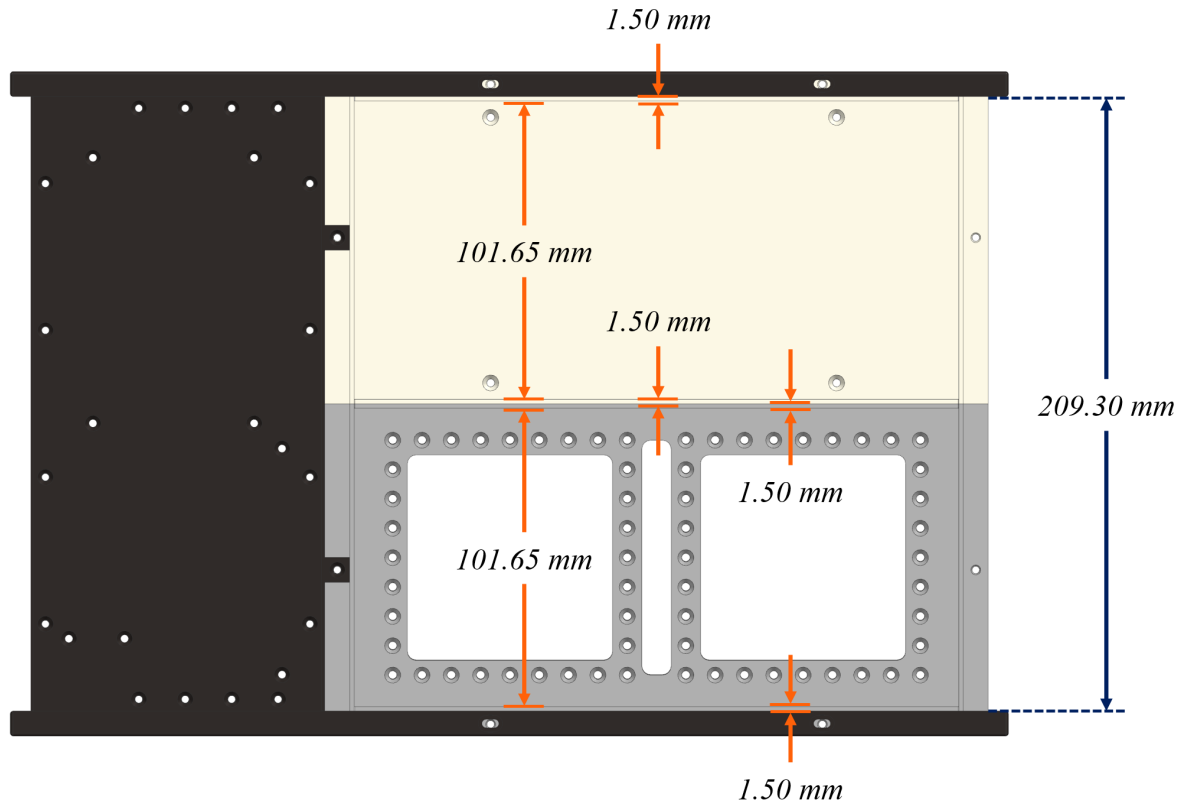


**Figure 5.2: The three modules after successful test assembly.**

Module integration was the next step in the test fit assembly. This uncovered an issue with the fit of the PM and M2 between the rails of M1. When attempting to slide the PM and M2 between the rails of M1, the modules would bind, indicating that they were oversized for the available space between the rails.

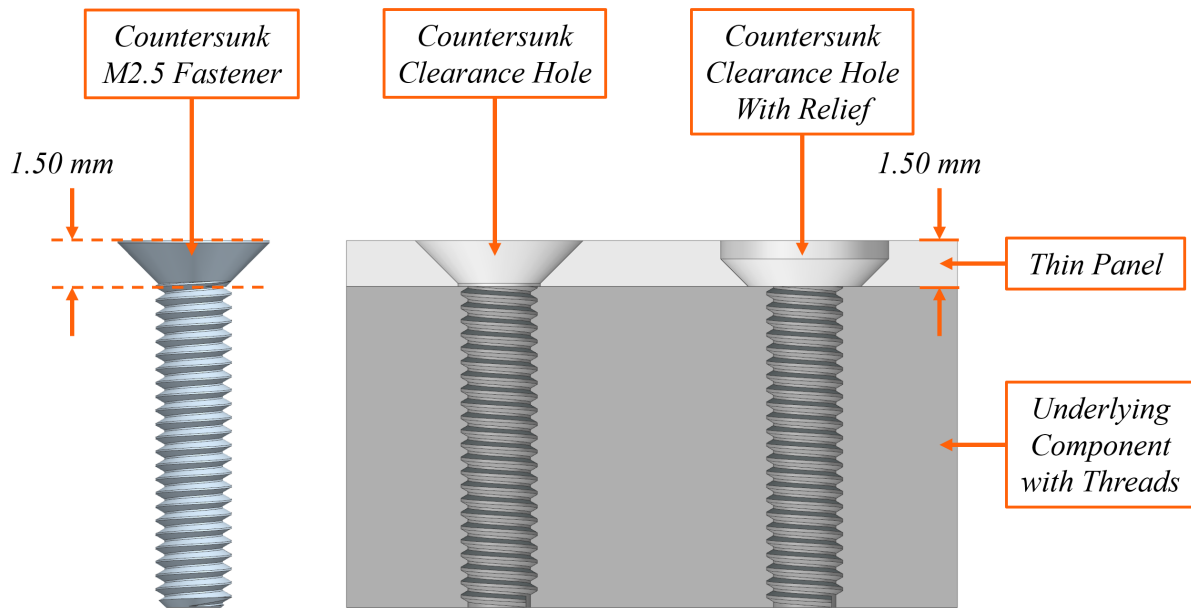
The modular design results in a larger number of components that must be mounted between the rails than found in traditional CubeSat structures. Each component has a critical, not-to-exceed dimension in the space between two rails. These critical dimensions contribute to tolerance stacking, which can negatively affect module integration if not properly managed.

Fig. 5.3 shows the critical dimensions of the PM and M2 in the X axis when they are mounted in Config. A. The total available space is shown by the blue dimension. Very little clearance is designed into the space between the rails. Since the rails provide the primary load path between the deployer and all of the internal components during launch, it is important that the PM and M2 make good contact with the interior faces of the rails. The consequence of this is that components that are oversized in their critical dimension can affect the integration of the modules. Even if each critical dimension is within tolerance, the accumulated error across multiple critical dimensions could make installation difficult. For this reason, each critical dimension was defined with a single sided tolerance in the engineering drawings created for manufacturing. The single sided tolerances define the maximum dimension and allow only slight undersizing of components due to imprecision in the manufacturing process.



**Figure 5.3: Critical dimensions (in orange) that contribute to tolerance stacking between the rails.**

The component inspection performed during the test fit assembly confirmed that all dimensions were within the specified single sided tolerances. This indicated that the module integration issue was arising from a different source. Upon further inspection of the assembled PM and M2, it was determined that the countersunk fasteners used in both modules were sitting slightly higher than the surfaces they were mounted into. Fig. 5.4 illustrates the challenges associated with countersunk fasteners that lead to the problem occurring.



**Figure 5.4: Diagram of countersunk fastener accommodation challenge with thin panels.**

M2.5 fasteners, like the one shown on the left side of the figure, are used throughout CUBE. They are installed through countersunk clearance holes in 1.5 mm thick panels into deep threaded holes in the underlying components. The nominal height of a countersunk M2.5 fastener head is 1.5 mm. A simple clearance hole can be created by cutting a corresponding taper in the panel, as shown in the middle of the diagram. In theory, this should make an installed fastener sit flush with the top face of the panel. However, inconsistency in thread engagement and fastener dimensions result in fastener heads sitting between 0.1 mm and 0.3 mm higher than the top face of the panel. This extra height accumulated at the interface between the PM and M2, as well as the faces of the two modules that slide against the interior faces of the rails.

When machining countersunk clearance holes, it is common practice to add relief to the taper as shown on the right side of the diagram. This relief ensures that the fastener head will sit below the surface of the panel. In the case of CUBE, the panels are not thick enough to enable this feature. When relief is added to the clearance hole, there is not enough thickness left for the tapered part of the hole. As a result, the fastener

head bottoms out on the threads of the underlying component before it is fully engaged in the tapered part of the clearance hole. This rules out adding relief to the clearance holes as a possible solution.

The use of low-profile fasteners was also explored. Special countersunk fasteners are manufactured with smaller head heights. This could potentially allow the fasteners to sit below the surface of the panels. However, low-profile fasteners are more common in larger sizes and are not readily available in the M2.5 size required for CUBE. Ultimately, changing fasteners and hole geometry were not viable solutions to the module integration issue.

Modifying the rails to create more clearance for the PM and M2 was identified as a more effective solution to the integration issue. The opposing interior X axis faces of the rails were milled out in the region where the modules are mounted. In total, 0.6 mm of material was removed from each rail. Fig. 5.5 shows the end of one rail with the modified region visible on the top face.

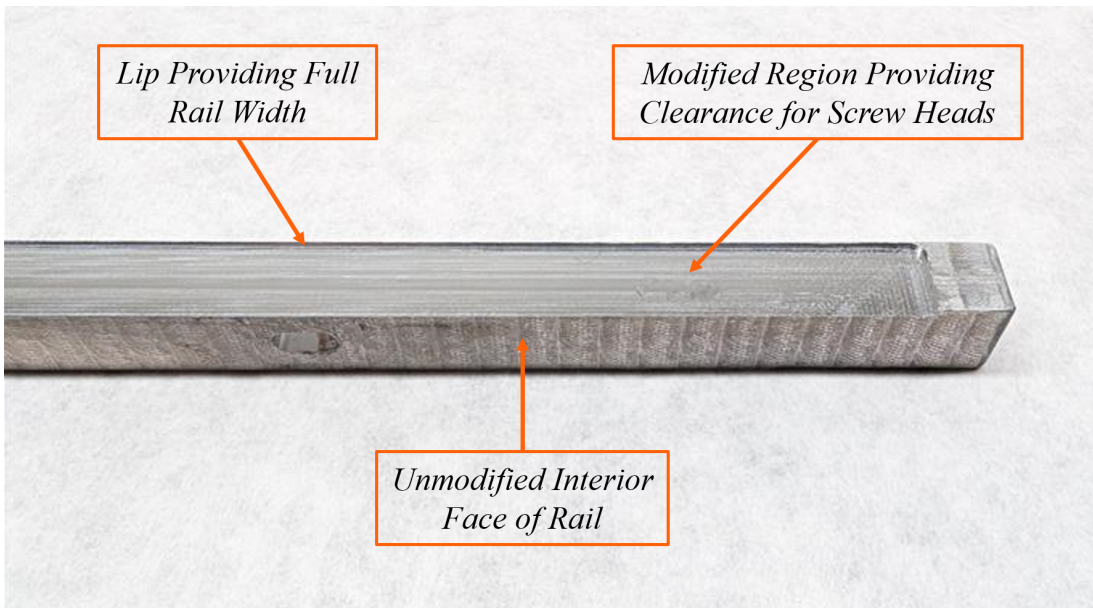


**Figure 5.5: Modification of rail face to accommodate raised screw heads.**

The modified region does not extend all the way to the edge of the rail due to CubeSat Design Standard requirements on rail thickness. A rail width of 8.5 mm must be maintained on both external faces [2]. The thin lip remaining on the rail after the interior region was milled out allows the exterior width to be 8.5 mm without affecting the module integration by occupying the space created by small chamfers on the edges of the PM and M2. The standoff segment of each rail that extends past the modules was left unmodified to preserve the rail-deployer interface. The interior faces of each rail in the Y axis were also left unmodified, because this axis is not affected by fasteners that sit above the panels they are mounted in. This minor modification to the four rails allowed the PM and M2 to slide between the rails without binding.

An alignment issue with the clearance holes in the rails was revealed when module integration was attempted after modifying the rail faces. The threaded holes in the PM and M2 did not properly align with the clearance holes in the rails in all CUBE configurations. The issue stemmed from the countersunk fastener tolerancing resulting in variability in the alignment of the threaded holes. The clearance holes originally specified in the rail design were simple countersunk clearance holes as shown in the top of Fig. 5.6.

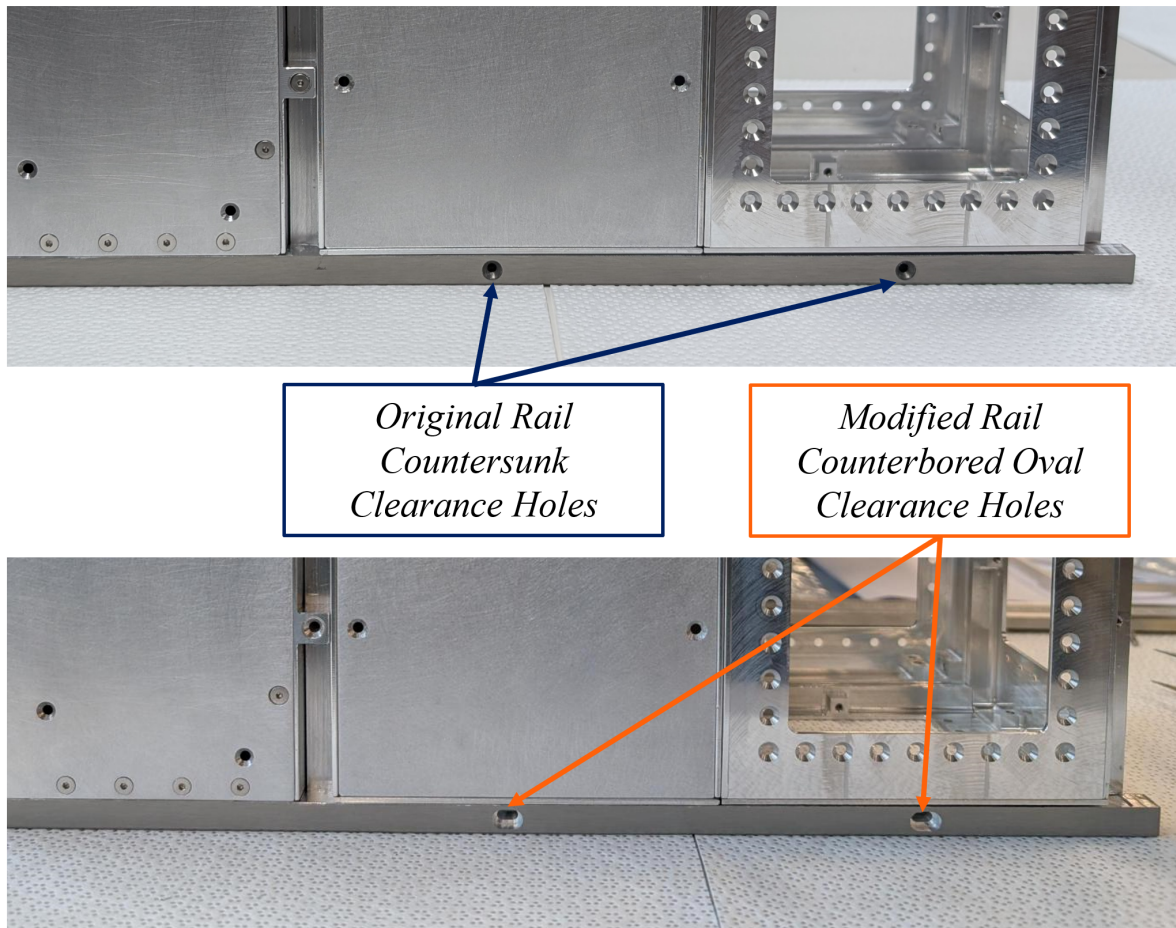


**Figure 5.6: Modification of rail holes from countersunk to counterbored oval**

This design allowed for very little variation in underlying threaded hole alignment. In order to increase the module integration tolerance, the rail clearance holes were modified from circular countersunk holes to oval counterbored holes. This modification is shown in the lower portion of the figure. The major axis of the oval clearance hole was sized to be two fastener diameters centered on the original hole. The major axis was aligned with the structure's Z axis to allow for variability in the Z location of the PM and M2. It was necessary to switch from a countersunk geometry to a counterbored geometry when making this change to create a sufficient surface area for contact between the rail and the fastener head. This modification allowed the eight rail fasteners to be installed regardless of the configuration.

The mass simulators and their secondary structures were manufactured and assembled to provide higher environmental test fidelity. Each assembly was weighed to verify that a representative component mass was being integrated into the structure. The assembled mass simulators and secondary structures are shown in Fig. 5.7. The top three assemblies represent the subsystem components of M1, and the bottom left assembly represents the subsystem components of M2. The payload plate, shown in the bottom right, is one of four payload plates that can be installed in the PM. Once the component masses had been verified, each mass simulator was integrated into the structure. The integration process went smoothly, and no issues were found.

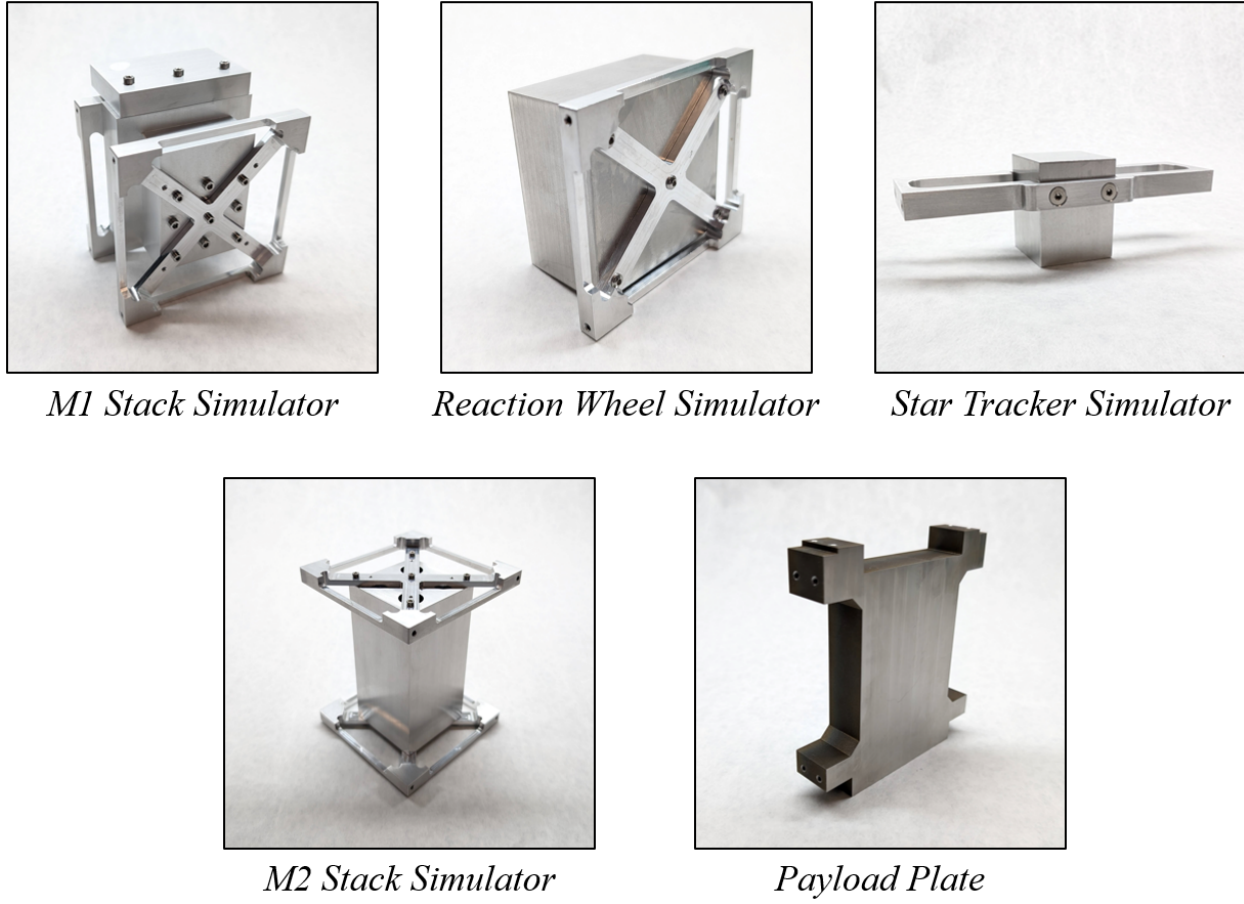


**Figure 5.7: Mass simulators and secondary structure of the CUBE prototype.**

The test fit assembly concluded with the full integration of three configurations (Fig. 5.8). The modules were assembled with all of the mass simulators and payload plates. These assemblies verified the payload accommodation flexibility of the design and marked the successful completion of the test fit assembly.

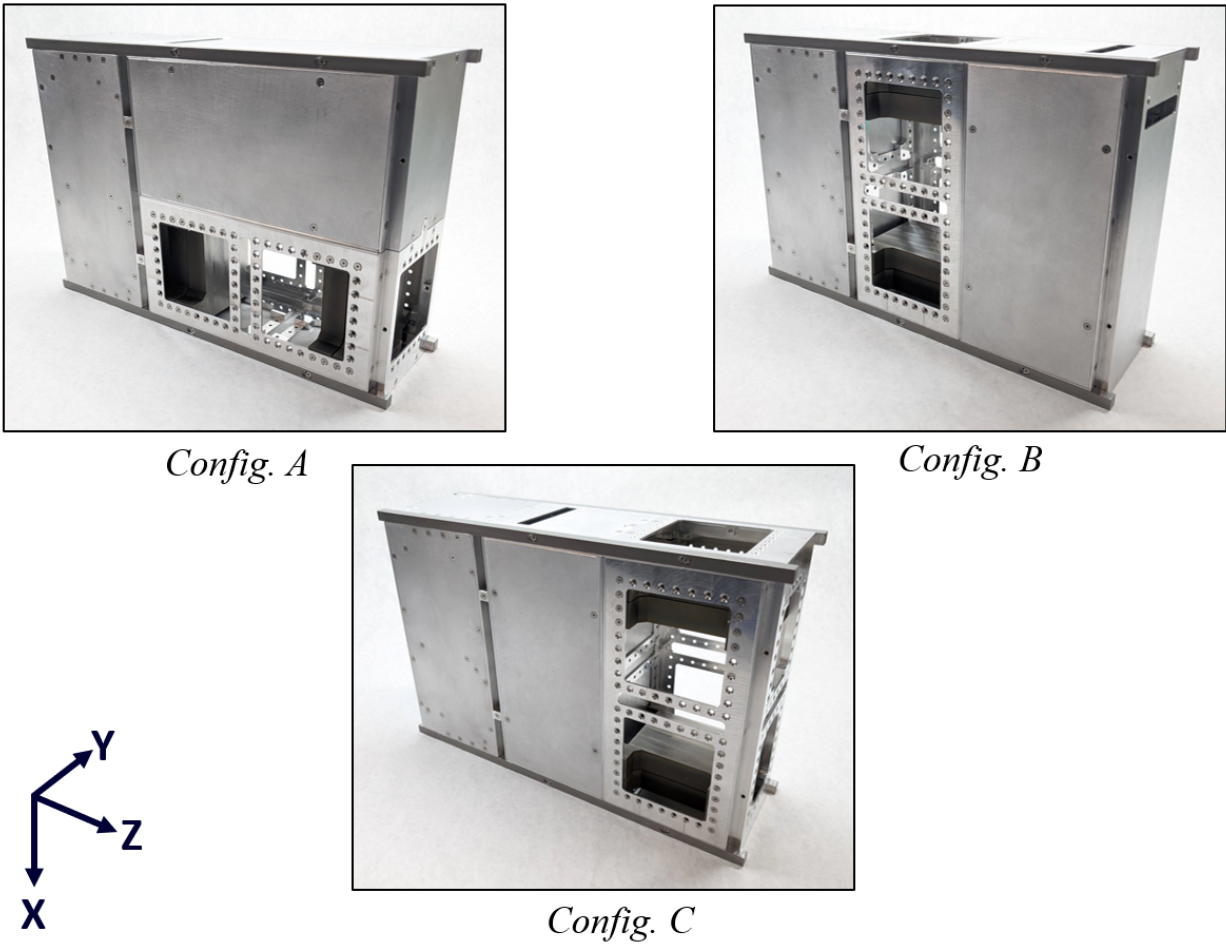


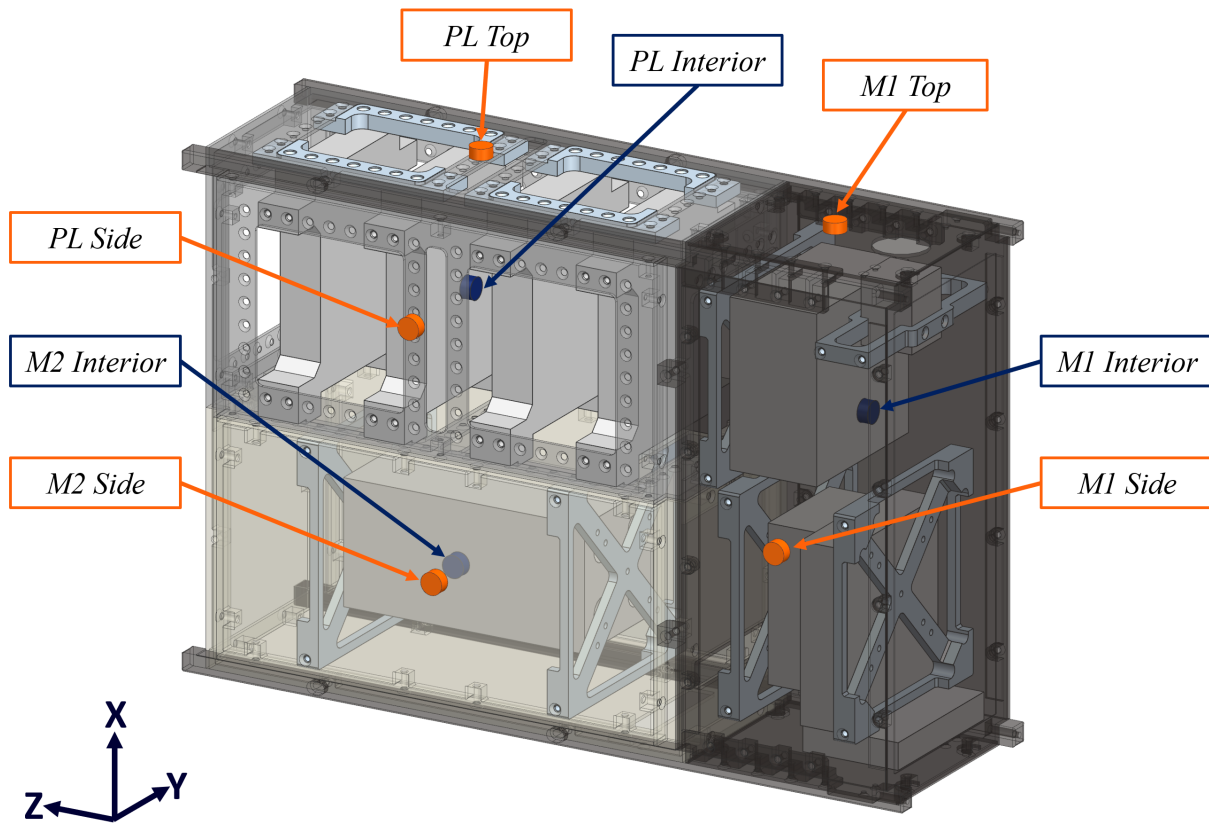
**Figure 5.8: CUBE prototype successfully assembled in all three configurations.**

## 5.2 Environmental Testing

Environmental testing was conducted to assess the performance of the system in simulated flight conditions. CUBE was subjected to high vacuum, and then its temperature was controlled through two cycles of hot and cold temperatures. Such temperature cycles under vacuum mimic a “day-in-the-life” for satellites operating in low Earth orbit. Rapid temperature changes brought about by entering and exiting orbital eclipses can “work” the structure, introducing stresses and displacements that can loosen fasteners and affect the structural integrity of a satellite.

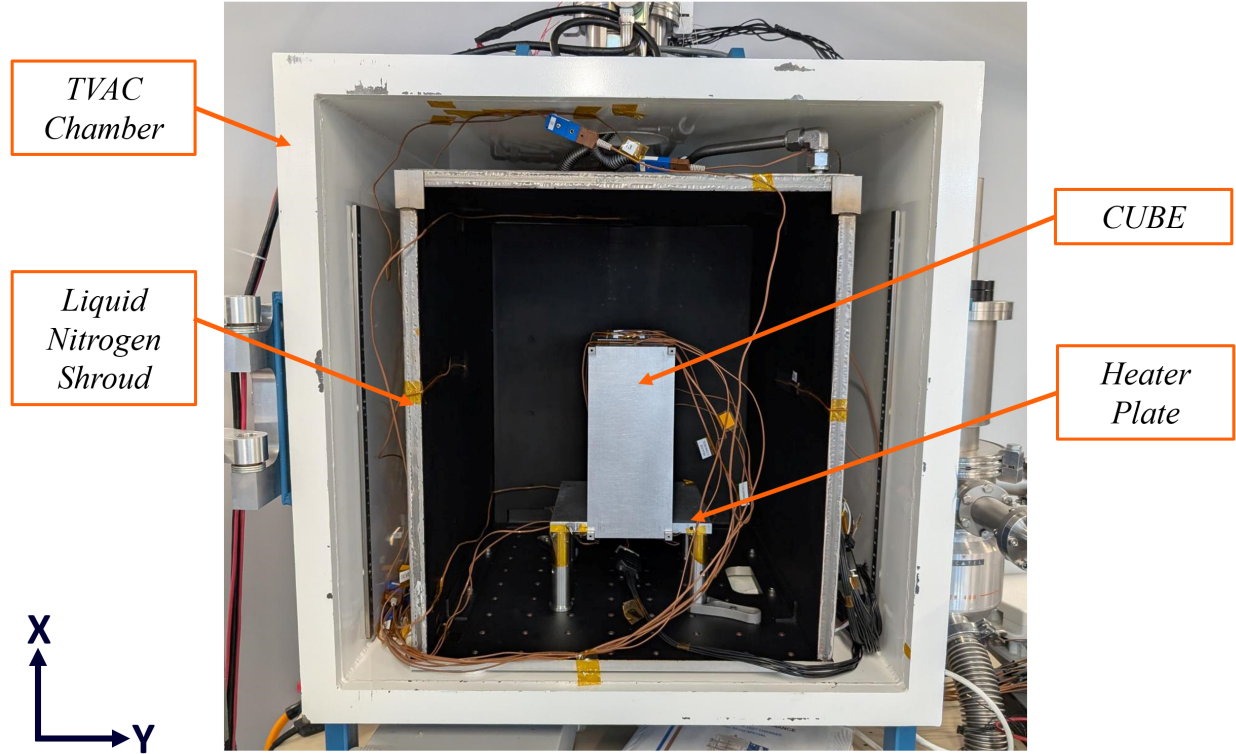
Thermocouple data was recorded throughout the thermal vacuum test to verify that the predetermined test profile was followed. A post-test torque check of each fastener in the structure was then performed to establish whether stress induced by the thermal loading created any loss of structural integrity. Survival without loss of structural integrity is the success criterion of the test.

Fig. 5.9 shows how the structure was prepared for environmental testing. Config. A was selected to test the heat transfer capability between M2 and the PM. In this orientation, heat is applied to the bottom of the structure through a heater plate. Eight thermocouples were mounted to monitor the temperature of the structure throughout the test. Thermocouples mounted in the interior are indicated by blue pucks and labels, while thermocouples mounted on the exterior are indicated by orange pucks and labels. Interior thermocouples were positioned near the center of each module on high thermal mass components to provide an accurate assessment of the heat transfer inside the module. Exterior thermocouples were placed near the center of each module panel on one Y axis face, and two thermocouples were placed on the top panels.



**Figure 5.9: CUBE thermocouple placement for TVAC testing.**

The environmental testing was performed in a TVAC chamber at UIUC. Fig. 5.10 shows CUBE placed in the TVAC chamber for testing. The -X face is resting on a heater plate. A shroud surrounds the test volume with liquid nitrogen pumped through it to achieve colder temperatures.



**Figure 5.10: Test setup of CUBE for TVAC testing.**

The test profile was developed from the requirements listed in NASA's General Environmental Verification Standard (GEVS). The standard provides guidance on thermal vacuum qualification tests at all levels of system and program development. For metallic structures, a minimum of two full thermal cycles of hot and cold temperatures are required [27]. The upper and lower temperature bounds are selected on a per-mission basis. For CUBE, an upper bound of  $+45^{\circ}\text{C}$  and a lower bound of  $-35^{\circ}\text{C}$  were chosen to be representative of the temperature extremes likely to be experienced in low Earth orbit. A two-hour dwell is required at each bound, and the transfer rate between the two bounds is required to be less than one degree per minute [27]. Pressure in the TVAC chamber was to be maintained at high vacuum throughout the test.

Fig. 5.11 shows thermocouple data from the environmental tests. The thermocouples have been averaged together to create a single trace, labeled Structure Average in the legend. Similarly, the shroud temperature presented has been averaged across two thermocouples. Because of limitation in the test equipment, some of the thermocouple data contained a relatively large amount of noise. Single point outliers in the thermocouple data, that had a deviation exceeding  $\pm 3^{\circ}\text{C}$ , were replaced with a rolling average of four surrounding points. Because the rate of temperature change is required to be less than one degree per minute, this approach smooths the data without unintentionally removing real results.

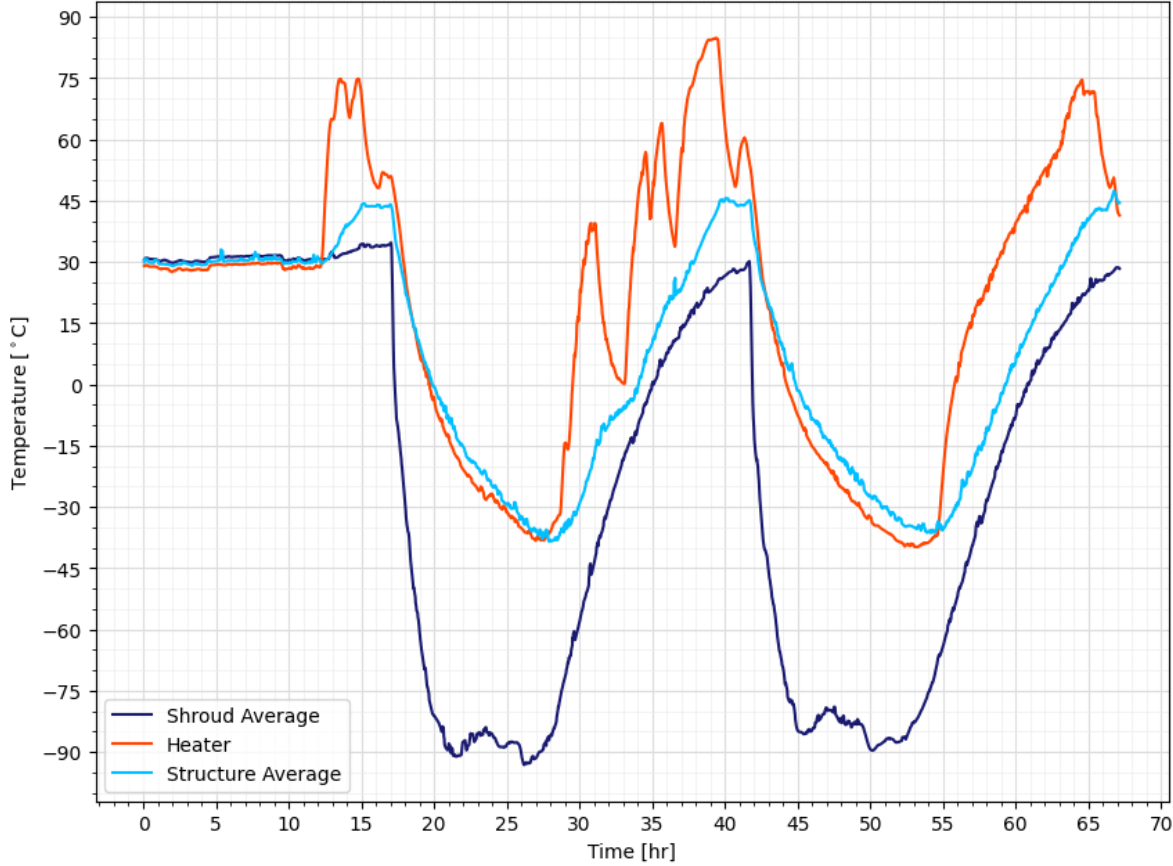


**Figure 5.11: Averaged temperature data from two-cycle TVAC test.**

The plot shows that two full cycles were completed, as specified in the test plan, starting with a climb to the upper temperature bound. Again, because of limitations in the test equipment, manual temperature control accounts for the large temperature swings in the profile. The average temperature decreased rapidly at the end of the two-hour dwell when liquid nitrogen was pumped into the shroud. The rate of the cold dive dropped off as the shroud leveled off at  $-85^{\circ}\text{C}$ . CUBE's temperature was held at  $-35^{\circ}\text{C}$  for the two-hour dwell, and then the heater plate was enabled to bring the temperature back up for a second cycle. The heating rate was more linear than the cooling rate, as the temperature climbed at approximately  $0.125^{\circ}\text{C}$  per minute. The second cycle was very similar to the first, with smoother heating following the second cold dwell. Throughout the test, the TVAC chamber pressure was maintained in the  $10^{-6}$  Torr range.

Some insight into the structure's heat conduction behavior can be gained by examining the test thermocouple profiles. Fig. 5.12 shows the temperature data from six of the thermocouples. The M1 Side thermocouple was excluded for producing unusably noisy data, and the M2 Interior thermocouple was excluded for failing partway through the test. The remaining six thermocouple datasets were smoothed using a simple 21-point rolling average.

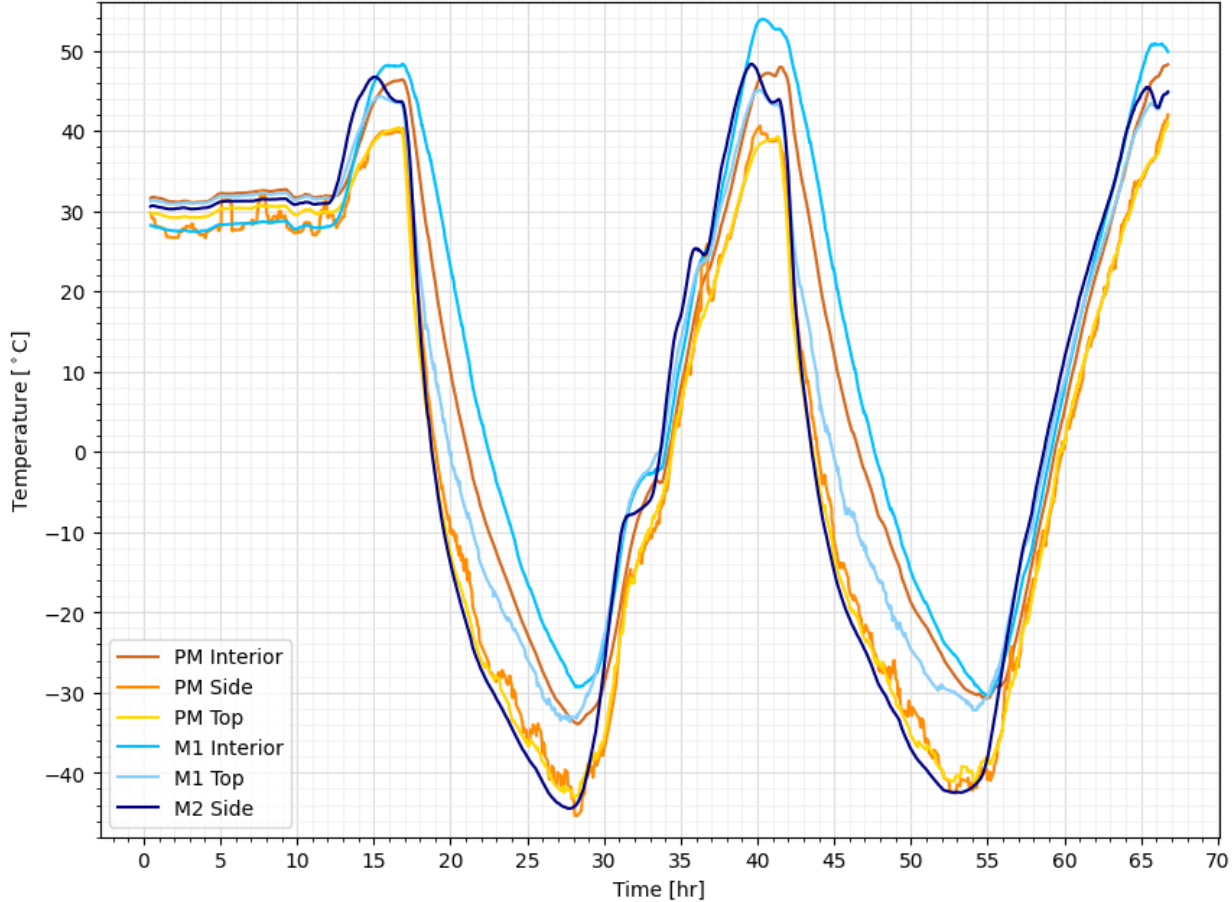


**Figure 5.12: Temperature data from six CUBE thermocouples smoothed with a rolling average.**

Starting at the first hot dwell, M2 Side exhibited some overshoot that quickly settled out. This was likely caused by a combination of the panel's low thermal mass, and its radiative heat transfer to the colder shroud wall. M1 Interior and PM Interior show the highest temperatures during the dwell. This is because they are shielded from the cold shroud walls by the exterior structure. PM Side and PM Top are both mounted to low thermal mass components, resulting in lower temperatures at equilibrium. However, they are also the thermocouples furthest from the heater plate, so they do not exhibit much overshoot.

During the first cycle to the lower temperature bound, M2 Side quickly dropped down to become the coldest of the six thermocouples. There was a significant spread in the thermocouple temperatures during this cycle. The exterior thermocouples lead the drop in temperature while the interior thermocouples lagged behind, radiatively insulated from the cold shroud walls. The cold dwell demonstrated a similar spread in temperatures, with the interior remaining close to ten degrees warmer than the exterior. This spread was eliminated during the climb back to the upper temperature bound on the second cycle. M2 Side quickly plateaued every time the heater plate temperature dropped during the climb.

The second cycle was very similar in performance to the first cycle. The climb after the second cycle resulted in a tighter grouping of the thermocouples and slightly more linear behavior than the first climb. CUBE performed as expected, passively regulating the temperature of its internal components while being subjected to wide temperature cycles.

CUBE was inspected after testing to assess its performance. The structure was visually inspected, and no changes were found in any of the components. Following this, a thorough disassembly was conducted, and each fastener was checked with a torque wrench to determine if any loss of preload had occurred over the course of the test. The fasteners were installed dry during assembly using a torque wrench. The M2.5 fasteners were all torqued to 0.4 N m, and the M3 fasteners were torqued to 1.0 N m. These torque values, while relatively low, are within recommended ranges for the small fastener sizes used [28]. Upon disassembly, it was found that 16 fasteners had lost a small amount of preload. The affected fasteners and their change in torque are listed in Table 5.1.

**Table 5.1: Post-environmental test CUBE torque check results.**

Fastener Location	# of Fasteners Changed	Pre-Test Torque [N m]	Post-Test Torque [N m]
<b>M1</b>			
M1 Stack Secondary Hardware	1	0.4	0.35
<b>M2</b>			
M2 Stack Secondary Hardware	1	0.4	0.35
<b>PM</b>			
Payload Plates -X Face	8	0.4	0.3
Payload Plates -Y Face	4	0.4	0.3

The fasteners that lost preload were all installed through the side panels of CUBE into secondary hardware that spans the respective modules. In this position, the fasteners are very susceptible to changes in stress in the thin panels from thermal gradients. The loss in preload was relatively small, with affected fasteners taking no more than a quarter turn to be retorqued to their pre-test specification.

The loss of fastener torque integrity means that the success criterion of the test was only partially fulfilled. As a result of these findings, the assembly procedure was modified. The torque value for the M2.5 fasteners was increased from 0.4 N m to 0.65 N m, and the torque value for the M3 fasteners was increased from 1.0 N m to 1.25 N m. A liquid thread locker would also be used in vibration testing to improve fastener capture.

### 5.3 Random Vibration Testing

Random vibration testing was conducted to assess the structure's performance in the environment of launch. Random vibration testing is a critical method for qualifying any spacecraft for flight. Launch vehicles create a harsh vibration environment that contains a wide range of frequencies and amplitudes. The test profile used was based on the measured environments of launch vehicles. The prototype was tested to a qualification level to enable lower load factor acceptance testing of subsequent flight versions. Much like environmental testing, the success criterion of the random vibration testing is survival of the specified test profile without experiencing structural failure.

The configuration used for testing was selected to provide worst-case loads within its structure. CUBE was assembled with all of its subsystem mass simulators as described in Section 5.1. Four payload plates were installed in the PM to bring it to its maximum mass. MOI estimates were made using Siemens NX to determine the configuration and mounting location of the payload plates that resulted in the largest MOI. Maximizing the MOI ensured that mass was distributed in the structure to create large moment arms when subjected to vibration. As a result of the MOI study, Config C. was selected for testing, and the payload plates were split between each end of the PM.

CUBE was assembled with Loctite 222 thread locker applied to each fastener. The fasteners were then torqued to the updated specifications resulting from thermal vacuum testing. Torque was applied evenly, and a star pattern was used for tightening the fasteners of each component to minimize the amount of preexisting stress. The completed test configuration for random vibration testing is shown in Fig. 5.13.

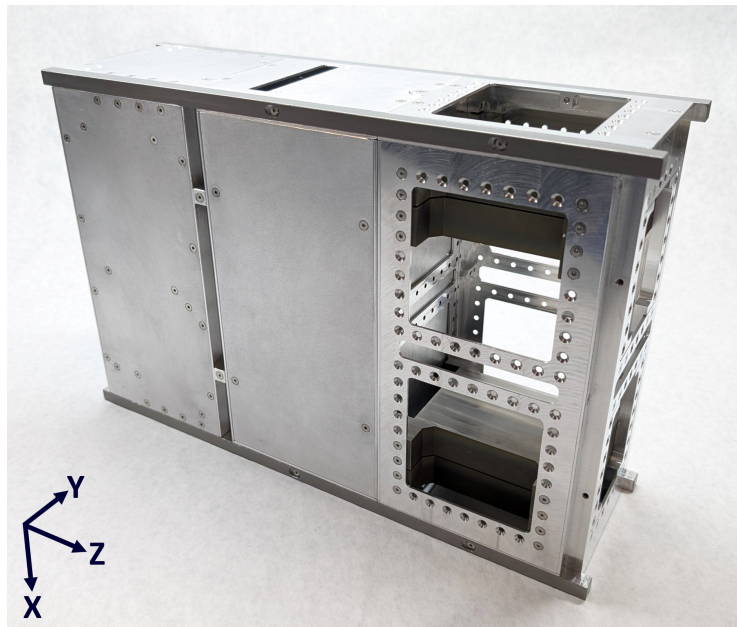
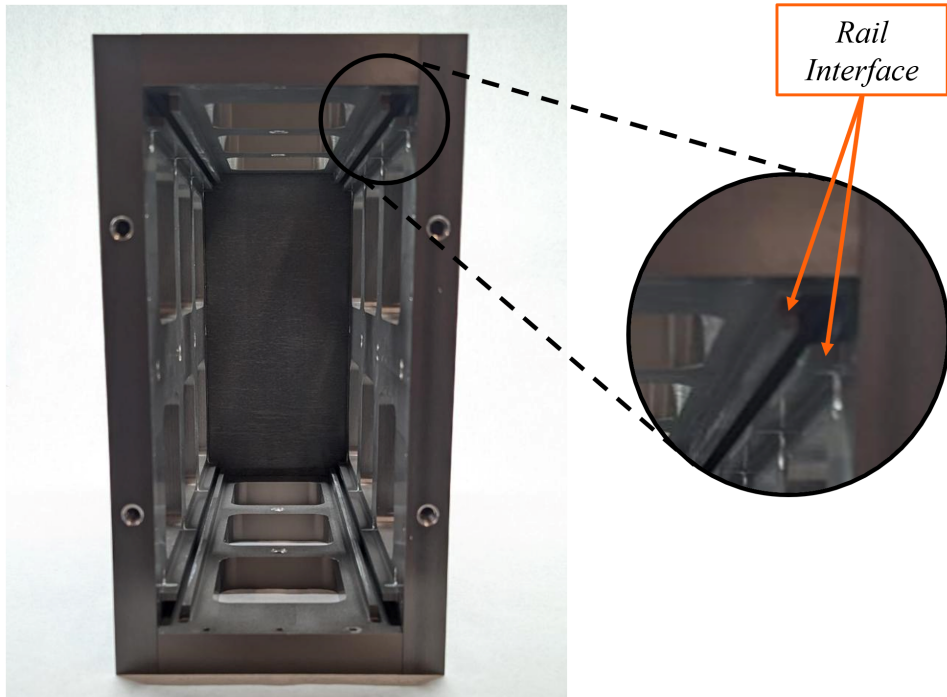


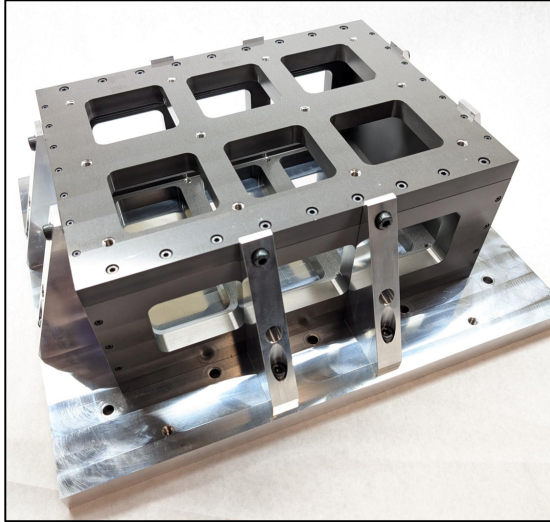
Figure 5.13: CUBE assembled in the test configuration for random vibration testing.

Properly constraining the test article for vibration testing required careful consideration. Since the random vibration test was designed to simulate a representative launch environment, it was important to constrain the structure as it would be constrained during launch. The accuracy of the applied constraints directly affects the accuracy of the test. A test fixture was designed to constrain the structure during the random vibration test. The test fixture interfaces with CUBE the same way that a CubeSat deployer would. Each rail slides between two corresponding tabs in the test fixture. Both ends are then constrained with solid metal plates. Fig. 5.14 shows the interior of the test fixture and highlights the rail interface in one of the corners.

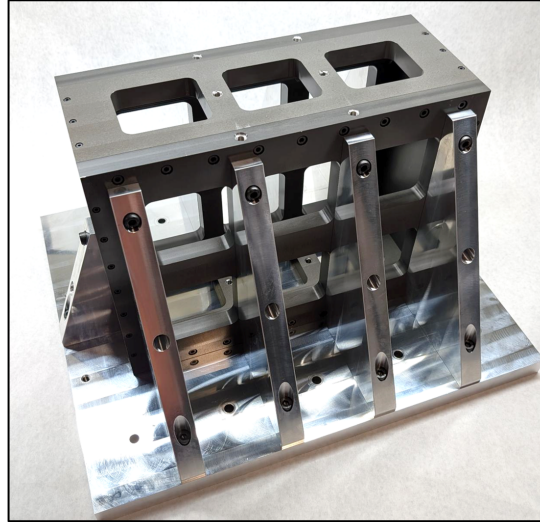


**Figure 5.14:** Test fixture interior.

The test fixture was designed to mount to an adapter plate in a horizontal and vertical orientation. This allows CUBE to be tested in all three axes on a single axis electrodynamic shaker table by rotating the adapter plate as needed. Fig. 5.15 shows the test fixture mounted to the adapter plate in the horizontal orientation, for testing in the Z and X axes, and the vertical orientation, for testing in the Y axis.



*Z and X Axis Orientation*



*Y Axis Orientation*

**Figure 5.15: Test fixture in two test axis orientations.**

The main function of the test fixture is to provide structural constraints without influencing the test results. To do this, the test fixture must be rigid throughout the entire frequency range of the random vibration test. Any resonances in the fixture could artificially change the loading on the structure. The test fixture achieved the necessary rigidity with a combination of thick, hard anodized aluminum panels and stiff gussets that are used to attach the test fixture to the adapter plate. FEA vibration simulations were performed to ensure that the first normal mode of the test fixture and adapter plate occurs above the frequency range of the random vibration test. The fasteners of the test fixture were all torqued to specification and torque striped to visually indicate any loss of preload during testing.

The test profile for the random vibration testing was selected from the NASA GEVS Vibroacoustic Qualification requirements. Fig. 5.16 shows the test profiles specified in NASA GEVS. There are four different profiles defined for different weight class test articles. The plot at the bottom of the figure shows the qualification level for each category. The table at the top of the figure provides equations for dB reductions to protoflight and acceptance levels. CUBE has a mass of 9.49 kg in its test configuration. When integrated with the test fixture, the test mass increases to 47.79 kg. Because of this, the 45 kg category test profile was used. This profile covers frequencies from 20 Hz to 2000 Hz. It sweeps up from 0.013 ASD to 0.08 ASD at a rate of 6 dB/Oct. It then sweeps back down at the same rate. This results in a cumulative root mean square acceleration (RMS) of 10.0g.

Frequency (Hz)	ASD Level ( $\text{g}^2/\text{Hz}$ )	
	Qualification	Acceptance
20	0.026	0.013
20-50	+6 dB/oct	+6 dB/oct
50-800	0.16	0.08
800-2000	-6 dB/oct	-6 dB/oct
2000	0.026	0.013
Overall	14.1 $\text{G}_{\text{rms}}$	10.0 $\text{G}_{\text{rms}}$

The acceleration spectral density level may be reduced for components weighing more than 22.7-kg (50 lb) according to:

	<u>Weight in kg</u>	<u>Weight in lb</u>
dB reduction	= $10 \log(W/22.7)$	$10 \log(W/50)$
ASD(50-800 Hz)	= $0.16 \cdot (22.7/W)$	$0.16 \cdot (50/W)$ for protoflight
ASD(50-800 Hz)	= $0.08 \cdot (22.7/W)$	$0.08 \cdot (50/W)$ for acceptance

Where W = component weight.

The slopes shall be maintained at + and - 6dB/oct for components weighing up to 59-kg (130-lb). Above that weight, the slopes shall be adjusted to maintain an ASD level of 0.01  $\text{g}^2/\text{Hz}$  at 20 and 2000 Hz.

For components weighing over 182-kg (400-lb), the test specification will be maintained at the level for 182-kg (400 pounds).

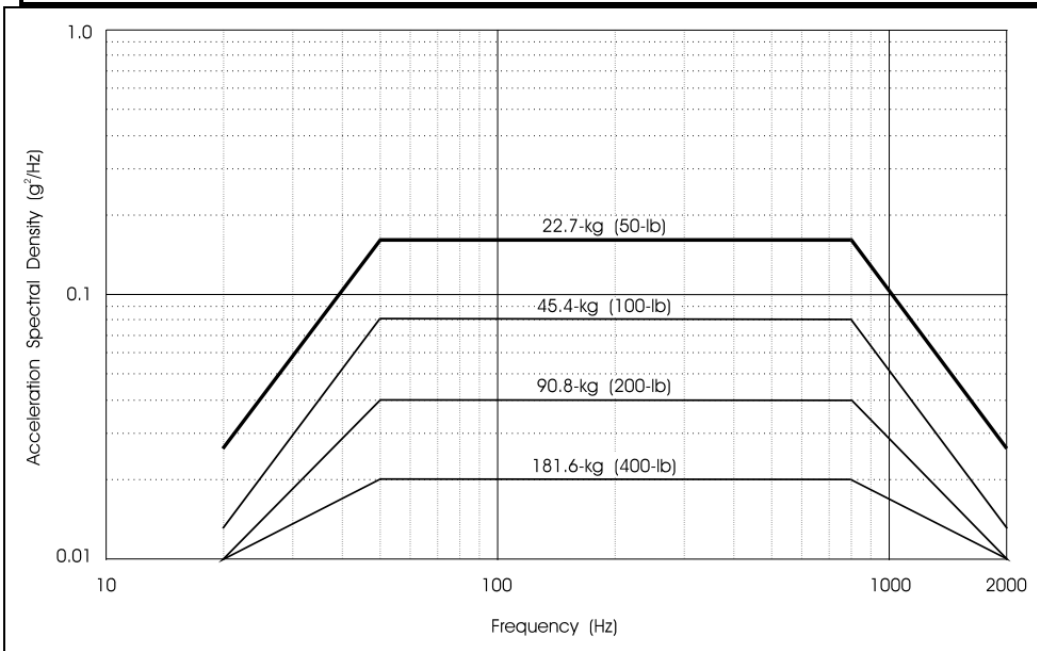


Figure 5.16: Random vibration test profiles [27].

The vibration test was conducted at Morehead State University on their Unholtz-Dickie Corp. ST/S452-36-36 electrodynamic shaker and integrated slip table. Test fixture preparation and mounting was performed by UIUC personnel, while test profile preparation and execution was performed by Morehead State University employees. The shaker was configured to automatically run the specified test profile, using feedback from a control accelerometer mounted to the slip table. A second accelerometer was mounted to the structure in line with the test axis during each test to measure the response of CUBE. The response accelerometer was calibrated with an ANSI Z540 certification.

The first random vibration test was performed in the Z axis. Fig. 5.17 shows the setup for this test.



**Figure 5.17: Test setup of CUBE for Z axis random vibration testing.**

Initial attempts to run the 10.0 GRMS test profile were unsuccessful. A combination of test equipment failure and control software configuration resulted in the response acceleration climbing rapidly beyond what the control accelerometer was reporting. The response accelerometer reached a peak of approximately 120 GRMS before the test was manually aborted. No physical damage was evident upon inspection of the structure after the test anomaly, so it was deemed acceptable to proceed with a repeat of the Z axis test.

After troubleshooting, the target acceleration for the control accelerometer was reduced to bring the response down toward the test profile. A successful Z axis test was completed with the new settings. The output plot of the accelerometer time histories is shown in Fig. 5.18. GRMS is reported for the control and response accelerometers on the vertical axis, with time on the horizontal axis. The response climbed above the test profile and settled at 21.5 GRMS. This level was maintained for two minutes before the end of the test.

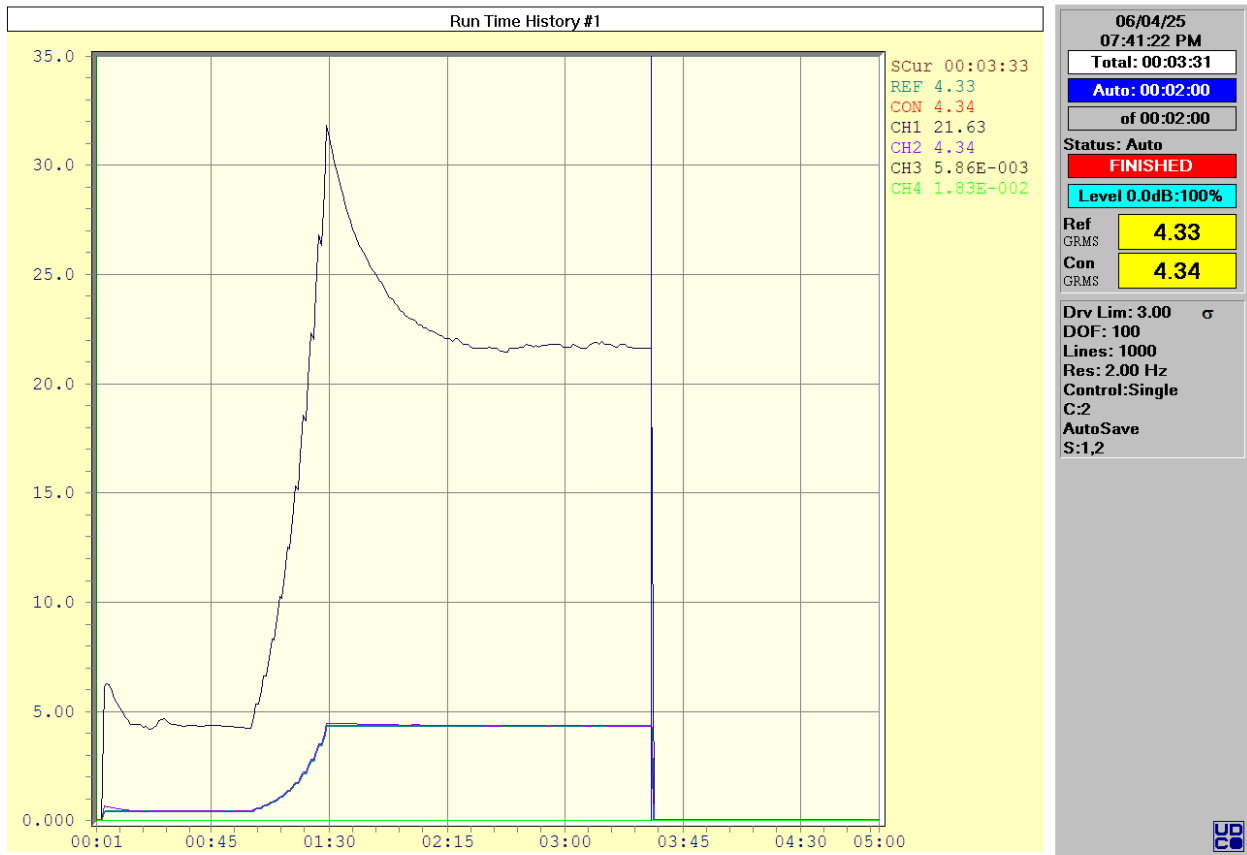


**Figure 5.18:** Z axis random vibration test profile.

Following the Z axis test, the X and Y axis tests were performed. Test setups and output plots are shown for these two tests in Fig. 5.19-5.22. Similar behavior was observed in these two tests. The response accelerometer reached a peak and then settled to a level that was maintained for two minutes. In all three tests, the test profile was exceeded. The amount by which it was exceeded varied between tests, likely due to a failing control accelerometer or other faulty test equipment. However, the calibrated measurements of response acceleration appear to be accurate. This shows that CUBE was subjected to vibration environments that meet and exceed qualification levels. Performance beyond the qualification envelope represents valuable strength margin. The structure design could potentially be optimized further at the expense of some of the margin in strength.

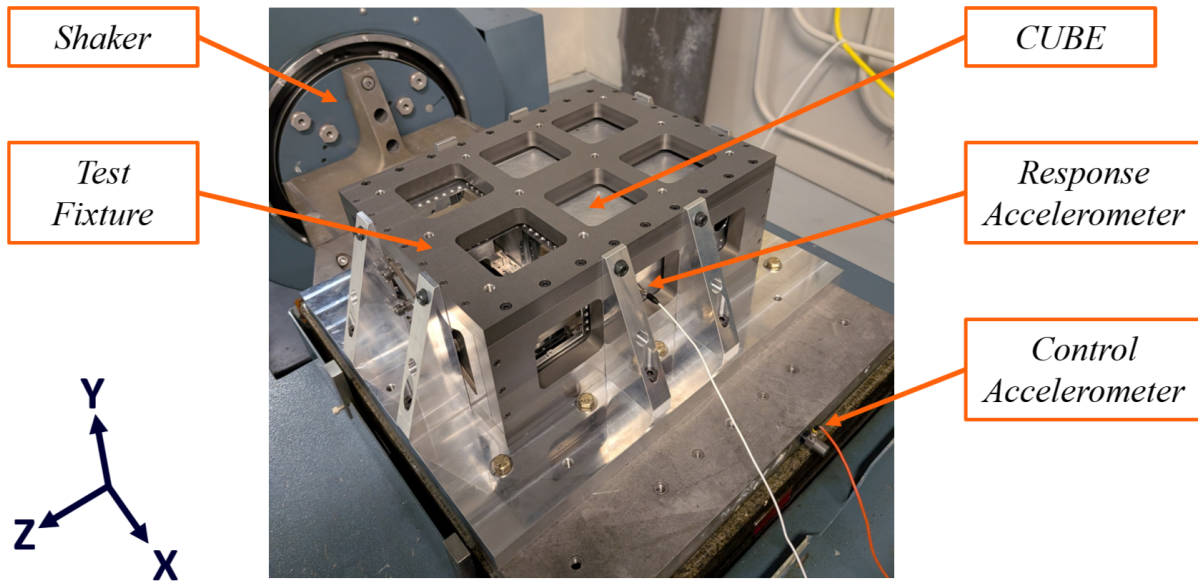


Figure 5.19: Test setup of CUBE for X axis random vibration testing.

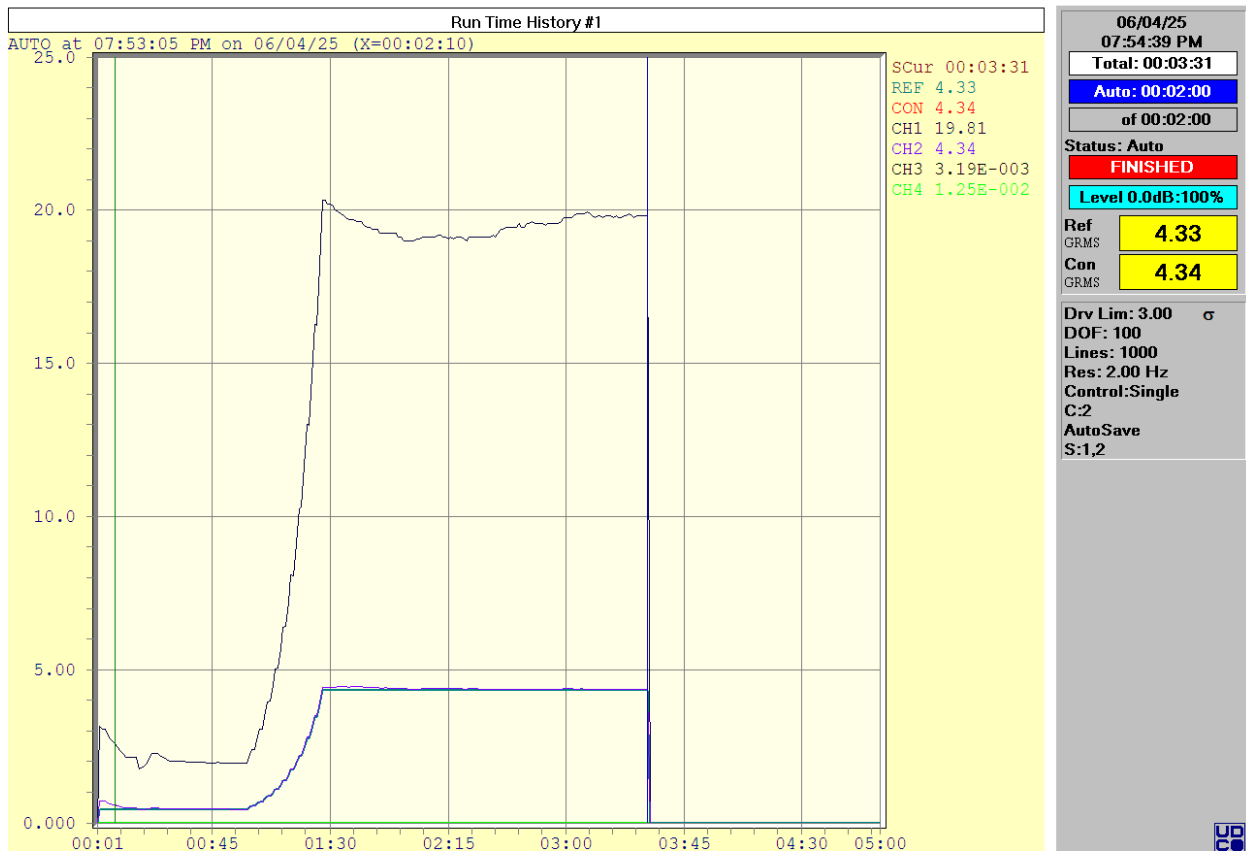


Figure 5.20: X axis random vibration test profile.

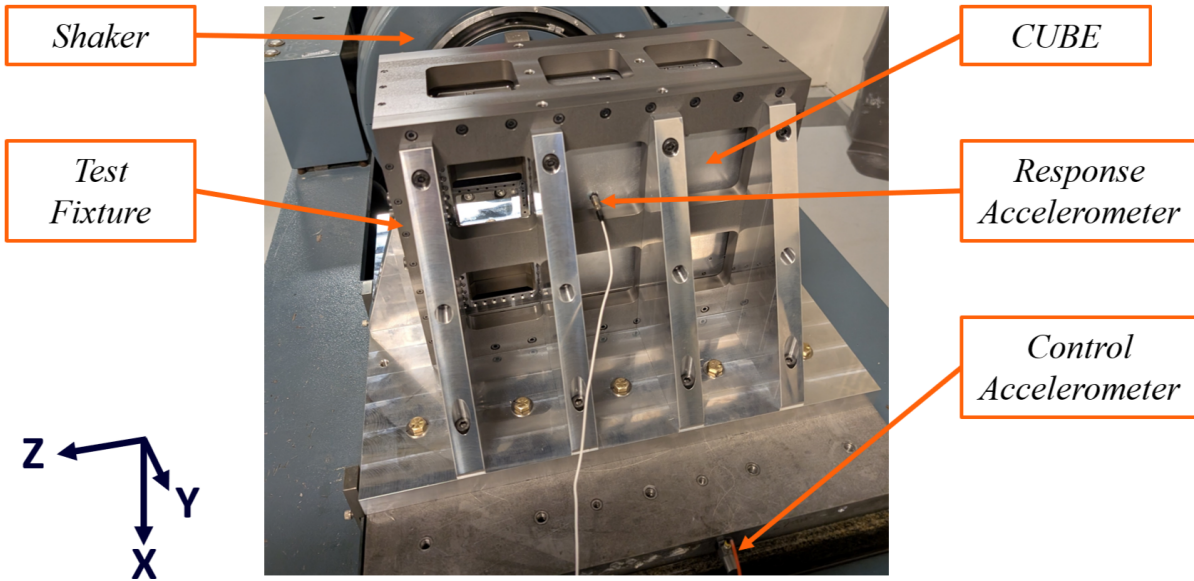


Figure 5.21: Test setup of CUBE for Y axis random vibration testing.

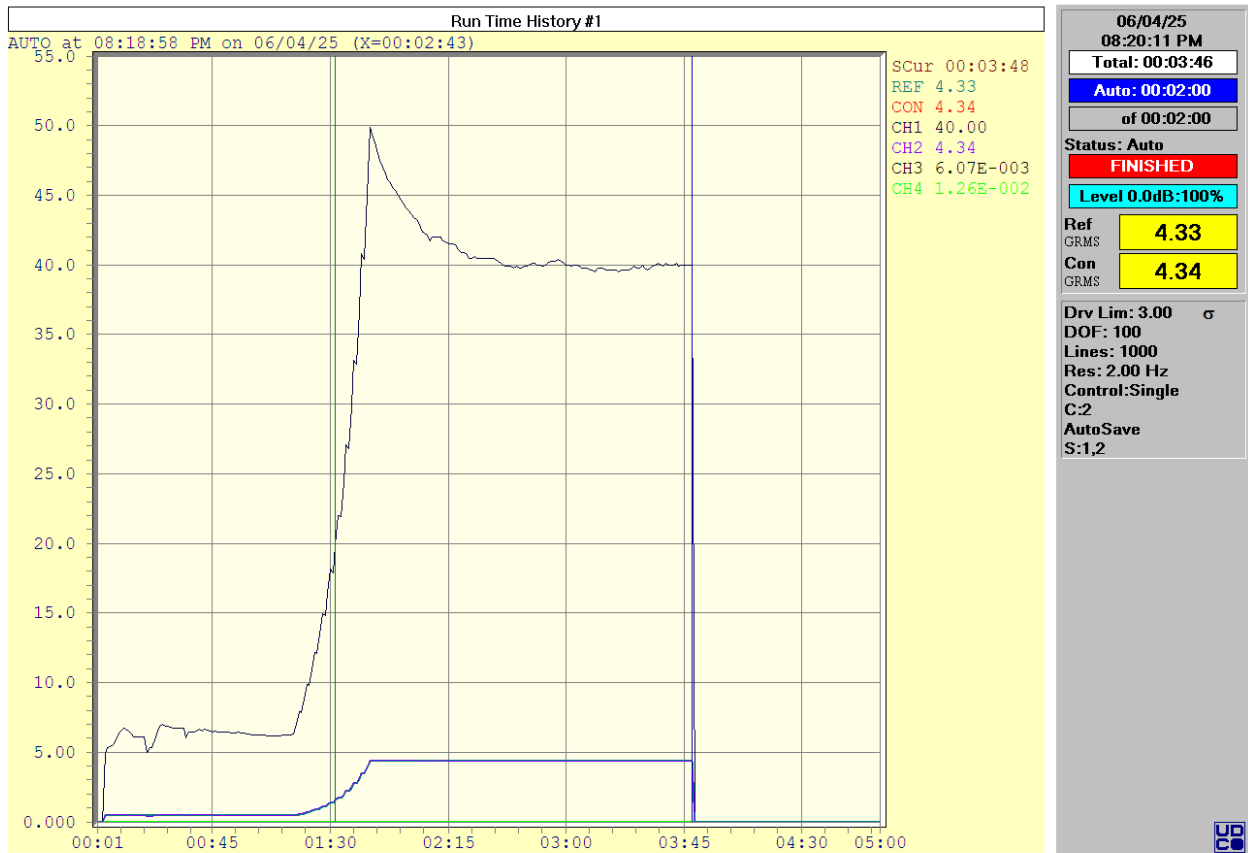


Figure 5.22: Y axis random vibration test profile.

CUBE was thoroughly inspected after the random vibration testing to determine if it had met the success criterion of the test. A visual inspection revealed no change in the test fixture. The structure was removed from the fixture, and no signs of structural failure were observed. Light wear in the surface of the hard coat anodization was observed in some regions of the rails and test fixture interface. This indicates that there may have been some relative motion between the rails and the test fixture during testing. CUBE was then disassembled, and the torque of each fastener was checked. Each component was also inspected for fatigue cracking. No cracking was observed. The results of the torque check are listed in Table 5.2.

**Table 5.2: Post-vibration test CUBE torque check results.**

Fastener Location	# of Fasteners Changed	Pre-Test Torque [N m]	Post-Test Torque [N m]
<b>M1</b>			
N/A		N/A	N/A
<b>M2</b>			
M2-PM Fasteners	2	0.65	0.4
<b>PM</b>			
Payload Plates -Y Face	2	0.9	0.6

Only four fasteners experienced loss of preload during testing. The two fasteners that attach the PM to M2 were slightly loose. There was also some light marring on the surface of the PM and M2 panels at this interface caused by raised fastener heads coming into contact with the panel of the other module. This suggests that there was some relative motion between the PM and M2. Since preload was only partially lost in the effected fasteners, the relative motion was likely very small. No structural damage was apparent in the vicinity of the fasteners on either module. The anomaly did not result in loss of structural integrity, since the PM was still firmly attached to the rails of M1 with four unaffected fasteners.

Two fasteners that mount the payload plates to the PM were also found to be slightly loose. Here too, the preload was only partially lost. The two fasteners were split between two different payload plates. While this is a concern for future builds, structural integrity was maintained since each payload plate is attached to the PM with 16 fasteners. The payload plates were still securely constrained even with the partial loss of joint strength caused by one loose fastener.

In conclusion, the CUBE design successfully withstood severe vibration environments well beyond those that it would experience on a real launch vehicle. It did so in a worst-case configuration with high MOI. Two minor issues were noted in the post-test inspection of fastener torques. However, these issues can be addressed procedurally in future builds.

# Chapter 6

## Conclusion

### 6.1 Summary

The system presented in this thesis was predicated on the challenges identified in the traditional CubeSat AIT process and the growing need for rapid response capabilities. The system objective was defined as follows: *CUBE is a CubeSat standards compatible structure system that provides configurable payload hosting capability promoting rapid access to space.* The fulfillment of this objective was then verified in the subsequent chapters. The functional requirements of the system were developed, and a set of representative DRMs were introduced. The design concept was solidified through the detailed development of structural modules, identification of subsystem components, and design of representative interfaces.

Configurable payload hosting capability is a cornerstone of the design. The DRMs demonstrated the flexibility of the application of the structural concept to real missions. Following the basic validation of the design, the FEA quasistatic and vibration simulations verified that CUBE would survive the launch environment with significant margins.

A prototype was manufactured to qualify the design. A test fit assembly verified structure configurability. The structure, complete with payload and subsystem component mass simulators, was subjected to space-like conditions in a TVAC chamber. This showed that the structure can withstand harsh, ever-changing thermal conditions without loss of structural integrity. A random vibration test was conducted in three axes using a worst-case payload configuration. This test exceeded the qualification level required by launch vehicle providers demonstrating a large strength margin. In conclusion, the objective of providing configurable payload hosting capability that promotes rapid access to space has been validated by the work presented in this thesis.

## 6.2 Future Work

The work documented in this thesis presents the initial successful development and testing of CUBE. Areas for future work include increasing the design maturity of the subsystems, further optimization of the structure, and expanding the applications of the modular architecture. With the completion of structure verification, effort can now be directed toward continuing the integration of subsystem hardware and maturation of the payload interface.

A benchtop, hardware-in-the-loop emulator, or FlatSat, could be constructed to validate the integration of the candidate components. Such an emulator would also enable early development of flight software. Increasing the subsystem design maturity in this fashion provides the benefit of easy access to each component for troubleshooting, as well as the opportunity to emulate certain components until flight units are acquired. Ideally, a flight test would serve to validate the payload flexibility and rapid response capabilities offered by the system. It would also raise the technology readiness level to an advanced state where benefits of utilizing a single design for multiple missions could be realized.

The design of CUBE has now been shown to be sufficient to withstand the environments of launch and operation in space. However, there are improvements that could potentially be made to the structure. The quasistatic load FEA revealed that stress in the structure will likely remain below 58 % of the yield strength in a real launch environment. The modal analysis showed first normal modes in each configuration being well above the 50 Hz cutoff for launch vehicle coupling. Random vibration testing that significantly exceeded the test profile did not result in structural failure. All of these outcomes indicate that the design could be further optimized (i.e., mass reduced).

The modular design inherently requires more structural mass than an open frame CubeSat structure does. Extra mass goes into the side panels of M1, M2, and the PM that do not make up an external face in the three configurations. While different panels are positioned internally in the structure depending on the selected configuration, they all still contribute to the overall strength and stiffness.

One method for optimizing the structure would be to stiffen the geometry using an isogrid. CUBE's structural panels are already thin, with most measuring only 1.5 mm. Reducing this thickness would result in a loss of rigidity. It is possible that the addition of a raised geometric pattern on the interior of the panels would allow for a reduction in panel thickness while maintaining the integrity of the design.

Alternative materials could also be explored for use in CUBE. Using composite material to construct module panels could result in significant mass savings. It could also enable the consolidation of multiple panels into a single component in a way that is not practical with subtractive manufacturing techniques. Future work along these lines could increase the structural efficiency of the design.

The modular architecture employed in CUBE’s design is deliberately scalable. The initial development was performed within the form factor of a 6U CubeSat. However, the system of modules, module connectors, and payload interfaces could just as easily be applied to other CubeSat sizes. A 3U version would offer the same streamlining of AIT operations in a smaller form factor, which would be accessible to missions on a tighter budget. Scaling up to a 12U or larger form factor creates many possibilities. Bus modules with different, but compatible, sets of subsystem components could be developed for interchangeable use as needed by each mission. The payload module could be much larger to accommodate a class of payloads that falls outside the scope of the 6U version. Alternatively, multiple smaller payload modules could be integrated into a single satellite to create a rideshare mission where payload developers are not hindered by delays in the development of the other payloads. The system objective prioritizes capabilities that are beneficial to small satellite missions of any size.

Regardless of scale, the modular architecture of CUBE streamlines the process of mission development and promotes rapid access to space. The adaptability and robustness demonstrated by the CUBE platform underscores its potential to serve as a foundational element for next-generation small satellite missions. By lowering barriers to configurability and rapid deployment, CUBE empowers mission designers to pursue innovative objectives with greater confidence and agility. As the landscape of space exploration continues to evolve, platforms like CUBE will play a pivotal role in democratizing access to space and accelerating the pace of discovery.

# References

- [1] M. Swartwout, *CubeSat Database*. [Online]. Available: <https://sites.google.com/a/slue.edu/swartwout/cubesat-database>.
- [2] *CubeSat Design Specification*. [Online]. Available: [https://static1.squarespace.com/static/5418c831e4b0fa4ecac1bacd/t/62193b7fc9e72e0053f00910/1645820809779/CDS+REV14\\_1+2022-02-09.pdf](https://static1.squarespace.com/static/5418c831e4b0fa4ecac1bacd/t/62193b7fc9e72e0053f00910/1645820809779/CDS+REV14_1+2022-02-09.pdf).
- [3] C. Venturini, B. Braun, D. Hinkley, and G. Berg, “Improving Mission Success of CubeSats,” in *32nd Annual AIAA/USU Conference on Small Satellites*, Aug. 2018. [Online]. Available: <https://digitalcommons.usu.edu/smallsat/2018/all2018/273/>.
- [4] *CubeSat 101: Basic Concepts and Processes for First-Time CubeSat Developers*, Oct. 2017. [Online]. Available: [https://www.nasa.gov/wp-content/uploads/2017/03/nasa\\_cslis\\_cubesat\\_101\\_508.pdf](https://www.nasa.gov/wp-content/uploads/2017/03/nasa_cslis_cubesat_101_508.pdf).
- [5] A. K. Cebrowski and J. W. Raymond, “Operationally Responsive Space: A New Defense Business Model,” *The US Army War College Quarterly: Parameters*, vol. 35, no. 2, May 2005. DOI: [10.55540/0031-1723.2250](https://doi.org/10.55540/0031-1723.2250).
- [6] P. Garrant, *Look-Ahead by Commander of Space Systems Command*, Jan. 2025. [Online]. Available: <https://www.ssc.spaceforce.mil/DesktopModules/ArticleCS/Print.aspx?PortalId=3&ModuleId=560&Article=4047156>.
- [7] E. Falkenhayn, “Multimission Modular Spacecraft (MMS),” in *Space Programs and Technologies Conference*, June 1988. DOI: [10.2514/6.1988-3513](https://doi.org/10.2514/6.1988-3513).
- [8] J. Esper, “Modular, Adaptive, Reconfigurable Systems: Technology for Sustainable, Reliable, Effective, and Affordable Space Exploration,” *AIP Conference Proceedings*, vol. 746, pp. 1033–1043, 2005. DOI: [10.1063/1.1867227](https://doi.org/10.1063/1.1867227).

- [9] T. M. Davis, “Operationally Responsive Space – The Way Forward,” in *29th Annual AIAA/USU Conference on Small Satellites*, Aug. 2015. [Online]. Available: <https://digitalcommons.usu.edu/cgi/viewcontent.cgi?article=3213&context=smallsat>.
- [10] “ORS-1 (Operationally Responsive Space-1),” in *eoPortal*, July 2012. [Online]. Available: <https://www.eoportal.org/satellite-missions/ors-1#mission-status>.
- [11] *GPS.gov: Space Segment*. [Online]. Available: <https://www.gps.gov/systems/gps/space/>.
- [12] I. Anderson, “Preliminary Design of the LAICE-F Mission to Study Atmospheric Gravity Waves,” M.S. thesis, University of Illinois at Urbana-Champaign, Jul. 2023. [Online]. Available: <https://hdl.handle.net/2142/121536>.
- [13] E. Alpine, “Preliminary Design of the Darkness Mission for Fermi National Accelerator Laboratory,” M.S. thesis, University of Illinois at Urbana-Champaign, Dec. 2021. [Online]. Available: <https://hdl.handle.net/2142/113895>.
- [14] F. E. Muller-Karger, “Remote Sensing of Marine Pollution: A Challenge for the 1990s,” *Marine Pollution Bulletin*, vol. 25, no. 1-4, pp. 54–60, Jan. 1992. DOI: [10.1016/0025-326X\(92\)90186-A](https://doi.org/10.1016/0025-326X(92)90186-A).
- [15] *HyperScape100*, Jan. 2025. [Online]. Available: <https://simera-sense.com/products/hyperscape100/>.
- [16] *HyperScape100 satsearch*. [Online]. Available: <https://satsearch.co/products/simera-sense-hyperscape100>.
- [17] *CubeSat Structures - AAC Clyde Space*. [Online]. Available: <https://www.aac-clyde.space/what-we-do/space-products-components/cubesat-structures>.
- [18] F. J. Voldbirk, “NanoStructure 6U Mk2,” 2024. [Online]. Available: <https://gomspace.com/UserFiles/Subsystems/datasheet/gs-ds-nanostructure-6u-Mk2-EXT.pdf>.
- [19] *6U XL Cubesat Structure*. [Online]. Available: <https://www.endurosat.com/products/6u-xl-cubesat-structure/>.
- [20] *MBM2 High-Performance Flight Computer for CubeSats and Nanosatellites*. [Online]. Available: <http://www.pumpkinspace.com/store/p208/mbm2.html>.
- [21] M. Harrigan, E. Widloski, and M. Lembeck, “Development of an Innovative Payload Interface Board for CubeSats,” *Small Satellite Conference*, Aug. 2023. [Online]. Available: <https://digitalcommons.usu.edu/smallsat/2023/all2023/250>.
- [22] S. V. Weston, “Small Spacecraft Technology State-of-the-Art Report 2024 Edition,” 2025. [Online]. Available: <https://www.nasa.gov/wp-content/uploads/2025/02/soa-2024.pdf>.

- [23] J. Wu, “A Basic Guide to I2C,” 2022. [Online]. Available: [https://www.ti.com/lit/an/sbaa565/sbaa565.pdf?ts=1752592735873&ref\\_url=https%253A%252F%252Fwww.google.com%252F](https://www.ti.com/lit/an/sbaa565/sbaa565.pdf?ts=1752592735873&ref_url=https%253A%252F%252Fwww.google.com%252F).
- [24] J. Kim, J.-C. Yoon, and B.-S. Kang, “Finite element analysis and modeling of structure with bolted joints,” *Applied Mathematical Modelling*, vol. 31, no. 5, pp. 895–911, May 2007. doi: [10.1016/j.apm.2006.03.020](https://doi.org/10.1016/j.apm.2006.03.020).
- [25] SpaceX, “Rideshare Payload User’s Guide,” 2024. [Online]. Available: [https://storage.googleapis.com/rideshare-static/Rideshare\\_Payload\\_Users\\_Guide.pdf](https://storage.googleapis.com/rideshare-static/Rideshare_Payload_Users_Guide.pdf).
- [26] G. Sebestyen, S. Fujikawa, N. Galassi, and A. Chuchra, *Low Earth Orbit Satellite Design*. Springer International Publishing, 2018, ISBN: 978-3-319-68314-0 978-3-319-68315-7. doi: [10.1007/978-3-319-68315-7](https://doi.org/10.1007/978-3-319-68315-7).
- [27] NASA, *General Environmental Verification Standard (GEVS) for GSFC Flight Programs and Projects*, Apr. 2021. [Online]. Available: <https://standards.nasa.gov/standard/GSFC/GSFC-STD-7000>.
- [28] H. T. Rivera-Rosario and J. S. Powell, “Installation Torque Tables for Noncritical Applications,” Tech. Rep. GRC-E-DAA-TN37585, Apr. 2017. [Online]. Available: <https://ntrs.nasa.gov/citations/20170003491>.